Novel electronic phases with eg orbitals in triangular lattices

Clément Février

Communauté
UNIVERSITÉ Grenoble Alpes

THÈSE

Pour obtenir le grade de

DOCTEUR DE LA COMMUNAUTE UNIVERSITE GRENOBLE ALPES

Spécialité : **Physique théorique**

Arrêté ministériel : 7 août 2006

Présentée par

Clément Février

Thèse dirigée par **Simone Fratini** et
codirigée par **Arnaud Ralko**

préparée au sein de l'**Institut Néel**
dans **l'École Doctorale de physique**

Nouvelles phases électroniques avec orbitales e_g dans les réseaux triangulaires

Thèse soutenue publiquement le **04 juillet 2016**,
devant le jury composé de :

Madame Silke BIERMANN
Professeur à l'École Polytechnique, Rapporteuse
Monsieur François VERNAY
Maître de conférences au Laboratoire PROMES CNRS, Rapporteur
Monsieur Marcello CIVELLI
Maître de conférences au Laboratoire de Physique des Solides, Membre
Madame Claudine LACROIX
Directeur de recherche à l'Institut Néel, Présidente du jury
Monsieur Simone FRATINI
Directeur de recherche à l'Institut Néel, Codirecteur
Monsieur Arnaud RALKO
Maître de conférences à l'Institut Néel, Codirecteur

Abstract

Layered compounds present a variety of electronic phases, whose origin can be often traced back to the presence of strong Coulomb interactions. This is particularly the case in layered transition metal compounds, which present narrow electronic bands constructed from d-orbitals, a key ingredient to understand their electronic properties. We will focus in this dissertation on systems where the crystal-field splits orbitals into two degenerate subsets, t_{2g} and e_g, and where conduction electrons are on e_g-orbitals. It is the case for $2H$-$AgNiO_2$, known to exhibit charge orders, a periodic arrangement of electrons on the lattice and also true in layered transition-metal dichalcogenides, which exhibit various charge ordering patterns whose physical origin is not fully understood.

In order to investigate charge ordering phenomena in this important class of materials, we derive a generic multiorbital extended Hubbard model and we refine our interest to e_g-orbital with strong local Coulomb interactions. Within an atomistic tight binding approach and using both electrostatic considerations and the unrestricted Hartree-Fock method, we build the phase diagrams as a function of the strength of the Coulomb interactions, both local and non-local, as well as the band structure of the e_g-orbitals manifold. We unravel a rich phase diagram with more than ten phases where some transitions can be controlled by the band structure parameters themselves. In particular, we find that pinball liquid phases can be stabilized in these systems. These are metallic threefold charge orders where localized charges (pins) are surrounded by itinerant charges (balls) on a honeycomb lattice, as experimentally observed in $AgNiO_2$ and to which we provide a solid theoretical explanation. Phases with large unit-cells are also stabilized, such as incommensurate charge and orbital orders and a $\sqrt{12} \times \sqrt{12}$ charge order, reminiscent of the charge order observed in the dichalcogenide materials. These electronic states are generic for the half-filled triangular lattice could therefore be found in other compounds of interest.

To capture the properties of phases with strong band structure anisotropy in the Mott state, that the unrestricted Hartree-Fock method fails to capture, we derive a Heisenberg-like Hamiltonian from perturbation theory. Then, we build the phase diagram of this new effective Hamiltonian using three complementary methods: a classical

approach, exact diagonalization with a symmetry analysis and Lanczos algorithm to attain a larger cluster size. In addition to the known phases of the Heisenberg model in presence of an external field, namely the Y and V configuration, the 1/3 plateau and the ferro-orbital phase, the anisotropy of the band structure of e_g-orbitals leads to other orderings with finite τ^y or τ^x and τ^z components, different stripe orders and orbital density waves. We build a rich phase diagram from this new Hamiltonian.

Table of contents

List of figures

List of tables

Chapter 1

Geometrical charge frustration on triangular lattices

The physical properties of electrons in solids can often be understood by assuming weakly or noninteracting particles. In such cases, electrons are delocalized meaning that the time that they spend on a specific site is very short (itinerant electrons). The insulating or metallic character of such compounds can be explained according to the electronic band structure, which results from the wavelike properties of individual electrons in the periodic potential of the underlying ions.

There are however many classes of materials which exhibit insulating states that cannot be described by the band structure alone. In such materials, electrons interact with each other and the independent particle approximation does not hold anymore: interaction effects cause the electrons to be localized, i.e. spending a larger time on individual atomic sites. In this case, a "real-space" particle picture becomes more appropriate than the "momentum-space" picture at the origin of the electronic bands.

Strongly interacting electron systems are often characterized by complex phase diagrams, reflecting an intricate interplay between magnetic, charge and orbital degrees of freedom. Phenomena such as the Mott metal–insulator transition [1, 2], charge orders close to high temperature superconductivity [3–7] and colossal magnetoresistance [8] are among the many interesting phenomena found. These compounds have narrow electronic bands resulting in a reduced kinetic energy, which is more easily overcome by the Coulomb interactions. When this happens, electrons will tend to be localized and the solid becomes an insulator. Many materials with partially filled d- or f-orbitals at Fermi level are characterized by strong interactions. Known examples are the cuprates, the manganites, the nickelates, the ruthenates, the iron pnictides and the chalcogenides.

Theoretically, the most interesting situation, also the most difficult to handle, is when both itinerant and localized behaviors compete. Transition-metal oxides with conduction electrons residing in d-orbitals are good examples of such competition. Indeed, the shape of these orbitals is more localized than s- or p-orbitals, which makes them subject to strong Coulomb interactions, but they have a long tail in the radial part with respect to the core electrons making them delocalized even though the direct overlap is weak.

In this class of materials, where the interplay between the different interactions is coupled to the conduction electrons, the metallic state expected in the absence of interactions has to compete with several ordered phases, in addition to the Mott phenomenon. Different degree of freedom can order: the spins, the electrons and the orbitals. These orders are called magnetic, charge and orbital orders, respectively. We can distinguish two families of orders: commensurate, when the unit cell formed by the pattern is periodically repeated over the lattice, and incommensurate otherwise. For example, commensurate charge and magnetic orders are observed in $2H$-$AgNiO_2$ [9–11] and both commensurate and incommensurate charge orders are observed in dichalcogenides [12–23]. We will present these two examples in more details in this chapter.

Historically, most studies of these compounds have concentrated either on low energy single band models, with the interaction effects properly included, or on more realistic ab-initio descriptions which however do not fully take into account interaction effects. Multiband effects in model Hamiltonians have been much less studied as, in many materials, they are not needed to understand the main physical phenomena; for example cuprates are most often reduced to a single effective band. One of the most salient examples where this is not true is the iron pnictides, a class of compounds discovered in 2008 [24], which are iron-based superconductors with a highest critical temperature of 55K [25]. In order to explain the superconductivity in these materials, theoretical studies of pnictides involve multiband models. One can mention, for example, the 5 bands model in Ref. [26]. Other systems of interest require a multiband approach to capture their properties. For example, a multiband Hubbard model has been studied to understand the unusual transport properties in perovskite ruthenates, of generic formula $A_{n+1}Ru_nO_{3n+1}$, with A either Ca or Sr, which has four electrons on the t_{2g}-orbitals [27]. Finally, orbital-selective Mott phase in iron chalcogenides requires multiorbital models [28].

Another example where the role of multiple bands is necessary to understand the electronic properties is the Kondo effect. The resistivity of metals is expected to decrease

with temperature, possibly drop to 0 if there is a transition to a superconducting state. In heavy fermion compounds, however, an increasing resistivity is measured at low temperature [29, 30]. Localized f-electrons are coupled to conduction electrons which creates enhanced scattering at low temperatures, leading to a logarithmic increase of the resistivity.

As we shall see in the next paragraphs, in the triangular lattice, the competition between different ordered states is increased by geometrical frustration. Frustration is an effect that appears when the classical ground state of the system is degenerate. It will typically stabilize unconventional phases, e.g. the pinball liquid [31–35], as we will describe in details below (Section 1.2).

In this chapter, we will give a brief introduction on triangular layered compounds and focus on certain classes that pose challenging problems to theory, due to the obsserved electronic orderings. Then, we will present the geometrical frustration and the pinball liquid. Finally, we will present the specificities introduced by the d-orbitals.

1.1 Triangular layered compounds

The triangular lattice appears often in nature, as it is the most compact arrangement of disks on a plane (mathematically defined by the kissing number); the same way face-centered cubic is in three dimension. Know examples are in crystals, helium adsorbed on graphite [36], Wigner crystal of electrons or of classical charged objects [37, 38], vertically shaken granular monolayers [39], etc.,

In condensed matter, one can find triangular lattice in layered compounds. They are solids made of layers where the sites, atoms or molecules, within a layer have the covalent bonds and layers are bonded with either smaller covalent bond or van der Waals' interactions [40] with small transfer integrals.

In this thesis, we focus on materials with layered triangular lattices and sizable electronic interactions because they present interesting charge-ordered phases whose origin is not fully understood. These include transition-metal oxides such as the layered cobaltates Na_xCoO_2, which exhibit complex electronic patterns which can be tuned by electron doping [41–44], and the triangular nickelates $2H$-$AgNiO_2$ [9–11] and Ag_2NiO_2 [45], which show a threefold ordered metallic phase with anomalous metallic properties. Another interesting class is that of transition-metal dichalcogenides. In $1T$-TaS_2, for example, the ordered state displays a marked Mott character induced by charge modulations with a large periodicity of $\sqrt{13} \times \sqrt{13}$ [15, 20], and various other periodicities are found in other compounds (see Section 1.1.2). What all these

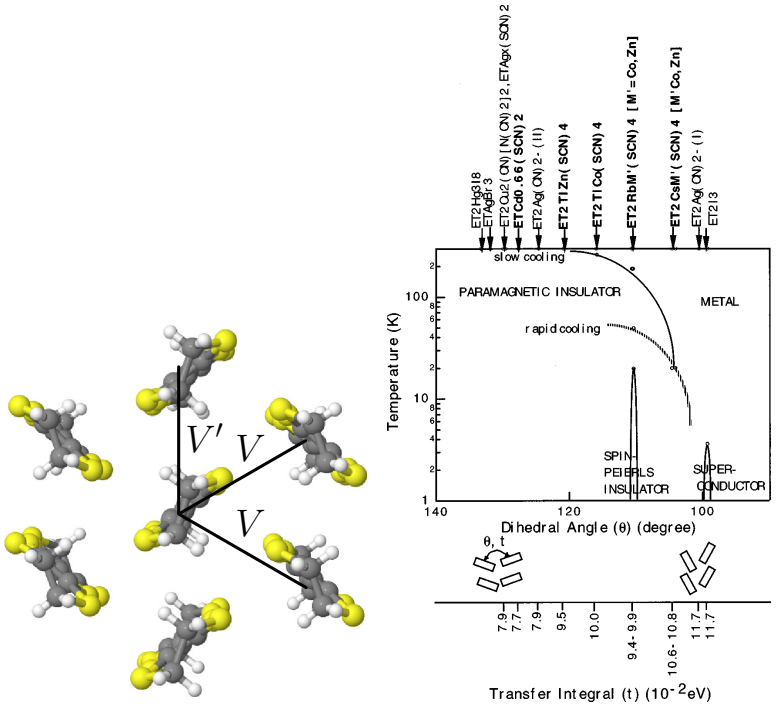

Fig. 1.1 (left) Arrangement of BEDT-TTF molecules in the conducting layers of θ-type ET crystals, with the corresponding nearest-neighbor Coulomb interactions, extracted from [33], and (right) its phase diagram as a function of a transfer integral (t) and a dihedral angle, extracted from [46].

materials have in common is that electrons live in bands constructed from d-atomic orbitals in an octahedral environment (see Section 1.3).

In the following, we present compounds with two-dimensional character and focus on those with triangular lattice and peculiar charge orders.

1.1.1 Quasi two-dimensional organic conductors

The class of quasi two-dimensional triangular lattice organic conductors ET_2X (ET=BEDT-TTF, bisethylenedithio-tetrafulvalene), where the X represents a monovalent closed-shell unit, are charge transfer compounds composed of alternating layers of conducting (donor) molecules ET and insulating (acceptor) units X. They exhibit a large variety of molecular arrangements corresponding to different polytypes classified by Greek characters (see Refs. [47–49] for an exhaustive list).

The materials of the θ-ET_2X class have a triangular lattice structure, shown in Fig. 1.1, with an average of $n = 3/2$ electrons per molecule, fixed by complete charge transfer between ET and X units. Since this corresponds to a three-quarter filled electronic band, these materials should be normal metals in the absence of interactions.

They exhibit a narrow conduction band due to the relatively weak inter-molecular overlaps $t \sim 0.1eV$, implying strong electron-electron correlations. Looking at the phase diagram in Figure 1.1, extracted from [46], we can divide them into three groups: (i) compounds that undergo a metal insulator transition with a structural transition and charge order ($\theta > 110^{\circ}$), (ii) compounds without phase transition ($\theta < 110^{\circ}$), and (iii) θ-ET_2I_3 which is the only superconductor of the series. It is understood that Coulomb interactions between electrons are the principal origin of the ordered phases observed in these compounds.

1.1.2 Layered transition-metal dichalcogenide

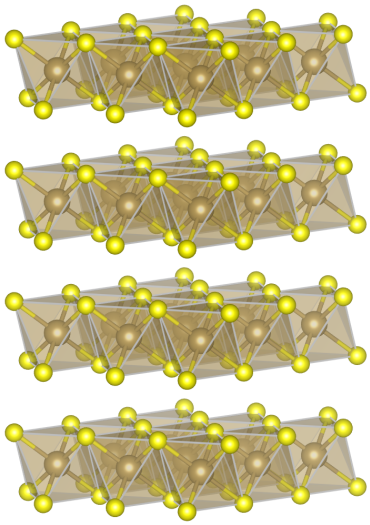

Fig. 1.2 Structure of layered $1T$-TaS_2. The center of octahedra (larger spheres) form a triangular lattice.

Layered transition-metal dichalcogenides, with generic formula MX_2 where M is a transition metal and X a chalcogen, are a class of two-dimensional compounds that exhibit various charge-ordered phases. One can cite for example $NbSe_2$, TaS_2, $TaSe_2$, $NbTe_2$, $TiSe_2$, $TiTe_2$, $TaTe_2$, $NbTe_2$, where the three chalcogen elements, S, Se and Te, have a s^2p^4 electronic configuration. When bonding with metal transition atoms, the two chalcogen atoms will take two electrons each from the transition metal depleting the latter of four electrons. We distinguish two major structures in these compounds: the $2H$ polytype which consists of a unit cell of two layers in a trigonal prismatic environment and the $1T$ polytype structure formed of a unit cell of only one layer in an octahedral environment [50]. The structure of layered 1T-TaS_2 is drawn in Figure 1.2, where the layers are formed of edge-shared octahedra (sulfur atoms at the corners).

The octahedra are connected such as their centers, here the transition-metal (tantalum atom), form a triangular lattice.

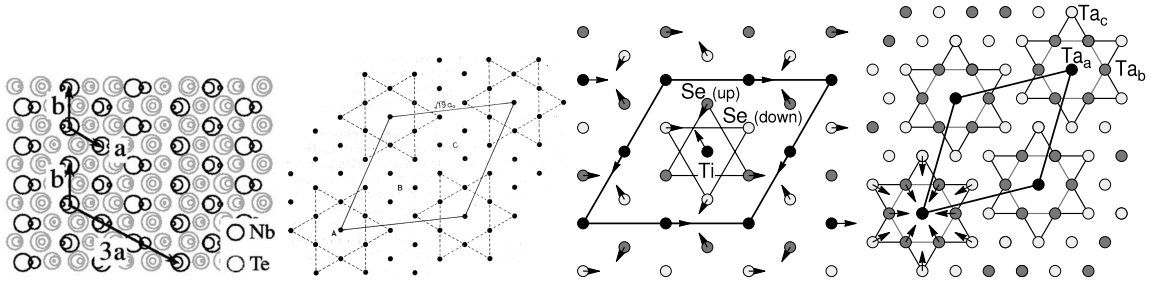

(a) (3×1) (b) $\left(\sqrt{19} \times \sqrt{19}\right)$ (c) (2×2) (d) $\left(\sqrt{13} \times \sqrt{13}\right)$

Fig. 1.3 Snapshots in real-space of charge density waves in layered transition-metal dichalcogenides. (a) (3×1), (b) $\left(\sqrt{19} \times \sqrt{19}\right)$ (c) (2×2), and (d) $\left(\sqrt{13} \times \sqrt{13}\right)$, superlattices of a single layer of (a) and (b) $NbTe_2$, (c) $1T$-$TiSe_2$, and (d) $1T$-TaS_2. In (a), the vectors represent the original and new unit cell. The arrows in (c) and (d) indicate in-plane displacements of the atoms from their original positions. For $NbTe_2$ and $1T$-TaS_2, only the Nb, Ta atoms, respectively, are shown; there are three inequivalent a, b and c Ta atomic sites in the distortion patterns. Snapshots are reproduced from other works: (a) is from [17], (b) is from [16], and (c) and (d) are from [22].

Such structures often present charge-ordered phases at low temperature. For example, $1T$-TaS_2 undergoes various transitions while being cooled down, from a metallic incommensurate charge-ordered phase above 350K to a commensurate charge-ordered phase below 180K [23]: a $\left(\sqrt{13} \times \sqrt{13}\right)$ charge density wave (see right panel in Figure 1.3), is also present in $TaSe_2$ [21, 51]. This large unit cell charge-ordered phase has a peculiar star of David modulation [16, 18]. Transition from this charge-ordered phase to a superconducting state can be driven by doping, substituting the sulfur atoms S by selenium Se $1T$-$TaS_{2-x}Se_x$ [21]. Other charge orders are depicted in Figure 1.3. One can cite the (3×1) for $1T$ type $TaTe_2$ and $NbTe_2$ [12, 17] or large unit cell $\left(\sqrt{19} \times \sqrt{19}\right)$ charge density wave in $TaTe_2$ and $NbTe_2$ [16].

Another layered transition metal dichalcogenide is $1T$-$TiSe_2$. The titanium atoms are also in an octahedral environment created by the surrounding selenium [52]. Below 200K a transition between a semimetal to a semimetal charge density wave occurs [53] associated with a $(2 \times 2 \times 2)$ superlattice [13, 14, 19].

Theoretically, these modulations of the charge can be in principle described by considering the interaction between electrons and the lattice through the electron-phonon coupling [22] because it is expected to be strong. However, the insulating behavior of gapped charge-ordered phases is not captured and a pseudo-gap is found

instead with DFT calculations [51]. This motivates the study of electron-electron interactions in layered transition-metal dichalcogenide, where their role has been chown to be important [20].

1.1.3 $2H$-$AgNiO_2$

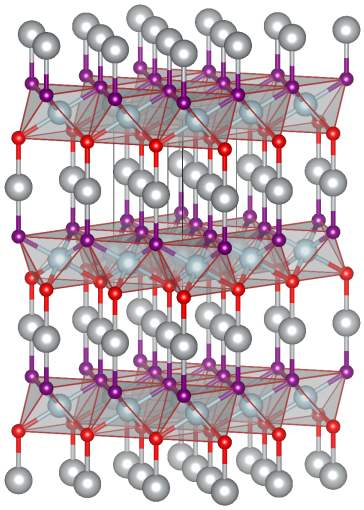

Fig. 1.4 Structure of $2H$-$AgNiO_2$. The oxygens at the top (purple) or the bottom (red) of a NiO_2 layer are represented in two different colors to distinguish them. The center of octahedra (larger spheres) form a triangular lattice.

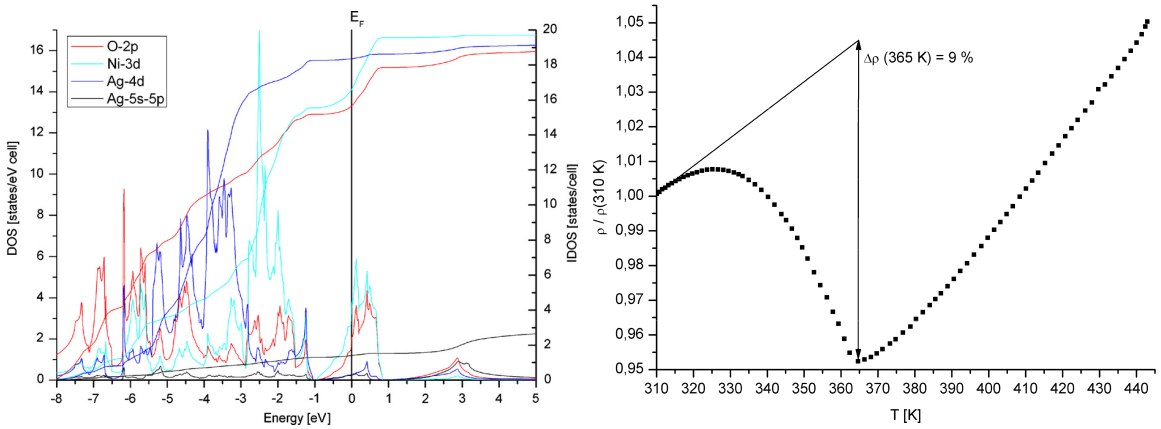

Fig. 1.5 (left) Partial density of states (DOS) and integrated density of states (IDOS) of the Ag-5s and -5p, Ni-3d and O-2p states in $2H$-$AgNiO_2$ and (right) evolution of resistivity as a function of temperature normalized by the resistivity at 310K, from Sörgel [54, 55].

$2H$-$AgNiO_2$ is a delafossite, of generic formula ABO_2, with A a cation stacked between edge-shared octahedral layers of BO_2, which presents a peculiar threefold charge order up to above room temperature ($T_{CO} = 365K$), and magnetic ordering setting in at a much lower temperature ($T_N = 19.7K$) [10, 9, 11, 56]. Layers of NiO_2 are separated by Ag layers perpendicular to the z axis [57] as depicted in Figure 1.4. Nickel atoms form a triangular lattice. The d-electrons of nickel are strongly hybridized with the p-electrons of the oxygen as shown in Figure 1.5.

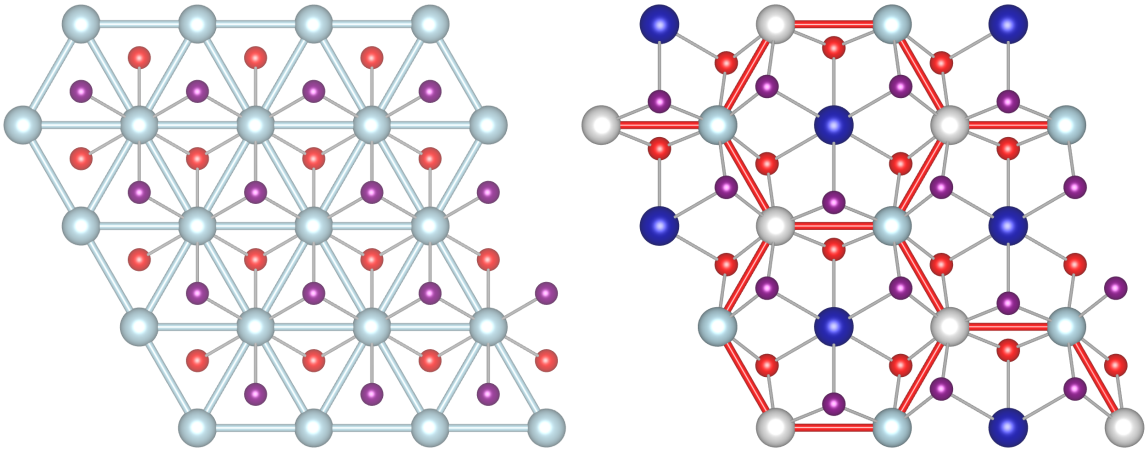

Fig. 1.6 Top view of a layer of NiO_2 in $2H$-$AgNiO_2$ before and after structural transition at 365K. The larger spheres represent nickel atoms while top (purple) and bottom (red) smaller spheres represent oxygen atoms. We increased the lattice distortions on Ni-O bonds to highlight structural change.

A structural transition with a metallic charge order happens below 365K [9]. There, a charge modulation appears with a three-site unit cell, where Ni^{3+} ($3d^7$) changes its valence state and ideally becomes Ni^{2+} on charge-rich and $Ni^{3.5+}$ on charge-poor sites (these are the saturating values assuming no quantum fluctuations), with a partial lift of orbital degeneracy (see Section 1.3), and oxygen atoms are moved away from charge-rich sites, as depicted in Figure 1.6. The Ni sites with two electrons undergo a magnetic stripe order at a lower temperature $T_N = 19.5K$ [9, 10, 58].

A mean-field study has been performed already to address triangular lattices with e_g-orbitals by taking into account the local Coulomb interaction and the electron-lattice interaction by Uchigaito and collaborators [59]. They found a metallic state with a threefold charge order in a realistic, though narrow, range of parameters with a small amplitude of the modulation. In this phase, all sites, charge-rich and charge-poor, are conducting.

Another work attempted to describe the charge order of this compound through electron-electron interactions for e_g-orbitals with Hund's coupling and reveals the pinball liquid phase [35] which is a good candidate for $2H$-$AgNiO_2$ because it has a threefold charge order with insulating charge-rich sites and metallic charge-poor sites forming an honeycomb lattice. However, the precise role of the orbital degeneracy in these systems remains unexplained to date. Study the influence of the specific band structures with multiple orbitals is the main goal of this thesis with $2H$-$AgNiO_2$ as a base for the following theoretical studies.

1.1.4 Adsorbates

An adsorbate is a material that absorbs atoms on its surface. These adsorbed atoms, called adatoms, can come from either another compound with which it shares the interface or from a gas.

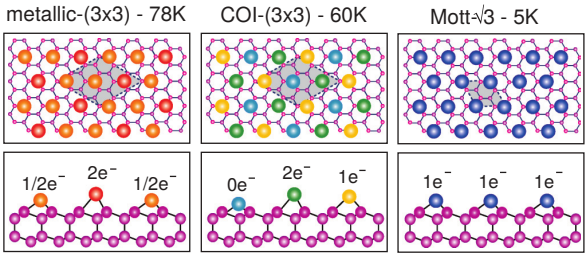

Fig. 1.7 Structure of Sn/Ge(111) from left to right by decreasing temperature: metallic 1U2D(3×3) structure, insulating charge order (3×3) with 2-1-0 electronic pattern and the Mott insulator $\left(\sqrt{3} \times \sqrt{3}\right) R30^{\circ}$. Large (small) spheres correspond to Sn (Ge) atoms and the unit cells are highlighted. These figures are extracted from [60]

In Sn/Ge(111), for example, Sn atoms are deposited on the Ge layer. These Sn adatoms form a triangular lattice as depicted in Figure 1.7 [60]. In the 1U2D(3×3) phase at room temperature, where one Sn atom out of three is farther from the Ge layer (up atom), there is a metallic charge order where the up atom receives one electron from the two down Sn atoms making the up Sn doubly occupied and the two down atoms share the remaining electron. Below 30K, all Sn atoms become equivalent and the system goes to a Mott phase called $\left(\sqrt{3} \times \sqrt{3}\right) R30^{\circ}$, with an intermediate insulating charge order in the 1U2D(3×3) structure with a 2-1-0 pattern.

Another example of such structure with charge order is Pb/Si(111) where STM reveals (3×3) charge order [61].

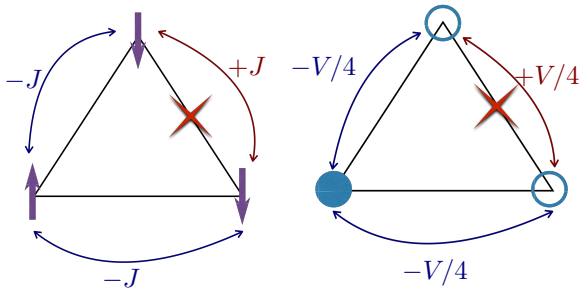

Fig. 1.8 Two examples of frustration on the triangular lattice: (left) magnetic and (right) charge frustration. The gain (blue) and the cost (red) in energy are given for each bond with respect to Equations 1.1 and 1.2.

1.2 Geometrical frustration

1.2.1 Magnetic frustration

Geometrical frustration appears when the local constraint cannot be extended univocally to the whole system, leading to a ground state that is macroscopically degenerate and involving a finite entropy at zero-temperature. For example, in a lattice of spins 1/2 with antiferromagnetic interactions between nearest neighbors, the system alternates spin up and down along each bond direction. For bipartite lattices, such as square or honeycomb, the ground state is a classical Néel state which corresponds to two ferromagnetic sublattices with an antiferromagnetic coupling between each other. In contrast, there is frustration when the system cannot satisfied all links at the same time classically. This happens, for example, when the system is a closed loop with an odd number of bonds. Magnetic frustration is an important example where the antiferromagnetic coupling of spins does not allow an arrangement on the pattern of the lattice, the simple examples are a triangle (one loop of three bonds), the triangular lattice and the Kagome lattice, which cannot satisfy all links at the same time [62–64].

The simplest illustration of the phenomenon can be given on an individual triangle where the spins are coupled anti-ferromagnetically

$$H_{\mathrm{AF}} = J \sum_{\langle i,j \rangle} \vec{S}_i . \vec{S}_j . \tag{1.1}$$

If a spin up is on the first site, the nearest neighbor spins should be pointing down in order to minimize the energy. The first two bonds are satisfied and therefore the energy is lowered by $-J$. However, there is a cost in energy for the third bond of $+J$, as depicted in Figure 1.8. Extending these considerations to the triangular lattice, two

of the three electrons in each triangle must share the same spin orientation The system has to find a compromise.

With the inclusion of quantum fluctuation, frustration will favor quantum phases, usually without long-range order. This is what happens in systems such as the Heisenberg chain with nearest (coupling J_1) and next nearest neighbors (coupling $J_2 = J_1/2$), called the Majumdar-Ghosh model [65, 66], and the $J_1 - J_2$ model on the square lattice [67] where ground states does not have magnetic order as the correlation decreases exponentially opening a gap between the ground state (singlet) and the first magnetic excitation. They have unusual properties for the susceptibility and specific heat. At zero-temperature, a class of frustrated antiferromagnetic model exhibit a peculiar behavior called "spin liquid," a disordered quantum state with no discernible pattern and no long-range spin-spin correlations but which restores spacial symmetries.

Due to the frustration, many states are close in energy to the ground state. From the mean-field approach that we will use in the third chapter, because it is difficult for the method to give the global minima, unrestricted Hartree-Fock often converges to one of these states that will appears to be reasonable solution because they minimize the electrostatic energy. Ensure to have the global minima will be an issue to tackle.

1.2.2 Charge frustration

In analogy with frustrated spin systems, inter-site Coulomb interactions between nearest neighbors induce a frustration of charge, which can be understood as follows. If one considers a system of spinless electrons at an average density of one electron per two sites, inter-site Coulomb interactions can be written

$$H_{\text{n.n.}} = V \sum_{\langle i,j \rangle} (n_i - 1/2)\,(n_j - 1/2)\,. \tag{1.2}$$

This form of Coulomb interaction clearly reveals that alternating between charge rich and charge poor site lowers the energy, as sketched in Figure 1.8. Indeed two electrons nearest neighbors, $n_i = 1$ and $n_j = 1$, or two holes, $n_i = 0$ and $n_j = 0$, will cost an energy $V/4$ whereas alternating electron and hole, $n_i = 1$ and $n_j = 0$, lowers the energy by $-V/4$. So the off-site Coulomb interaction V acts on electrons like the antiferromagnetic coupling for spins.

In total analogy with magnetic frustration, charge frustration constitutes a favorable playground for the emergence of novel phases where the classical degeneracy of the ground state involves a competition between these states. The system explores the different degenerate states and remains dynamic when plugging quantum fluctuations,

which leads to exotic phases such as spin liquid with magnetic frustration and a peculiar state for the charge frustration, the pinball liquid.

1.2.3 Pinball liquid

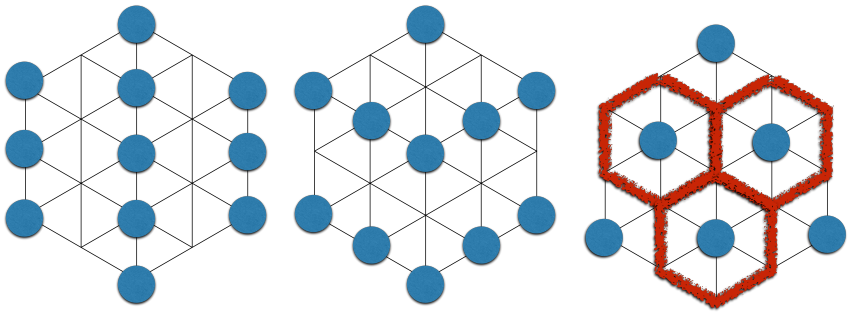

Fig. 1.9 Sketches of phases that can occur for the half-filled spinless single-band extended Hubbard model on the triangular lattice: (left) vertical stripes, (middle) disordered stripes and (right) pinball liquid.

Let us consider a simple system, a spinless single-band triangular lattice at half filling, i.e. with one electron every two sites. Electrons interact with the short-range Coulomb interaction in Equation 1.2. The classical ground state of this system is any charge order with a stripe pattern such as the energy per site is $V/2$ (two examples are sketched in Figure 1.9). The ground state is infinitely degenerate. Adding the quantum fluctuations lifts the classical degeneracy, leading to novel phases. A peculiar electronic state without classical equivalent induced by frustration is the pinball liquid (PL) phase, that we describe in the following paragraphs.

The pinball liquid is a metallic charge ordered state where localized (pins) and itinerant electrons (balls) coexist, as sketched on the right panel of Figure 1.9. The insulating threefold charge order formed by the pins (charge-rich sites) is surrounded by balls (charge-poor sites) free to move on the metallic honeycomb lattice.

The existence of the pinball liquid as a robust phase of the extended Hubbard model on the triangular lattice is now a consolidated fact It has been demonstrated by several complementary techniques and approximations, such as mean field theory [68], Dynamical Mean Field Theory (DMFT) [38], variational Monte Carlo [32], Exact diagonalization [33, 69], Variational Monte Carlo [70]. A typical phase diagram for the case of both isotropic Coulomb interactions and hopping integrals is plotted using data from Ref. [33] in Figure1.10[1]. The pinball liquid is stabilized by strong local Coulomb

[1]This work has been performed at a filling of three-quarter where the role of electrons and holes are switched.

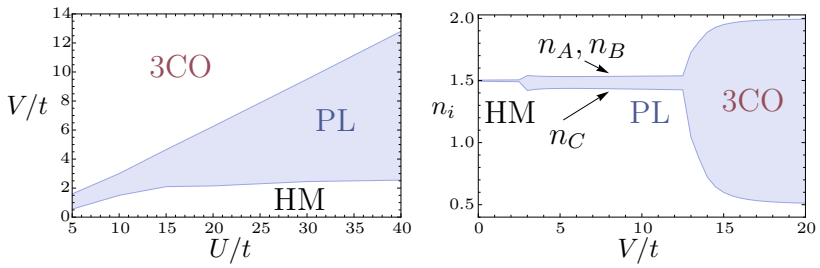

Fig. 1.10 (left) Phase diagram in the (U, V) plane for the three-quarter-filled extended Hubbard model. Three phases are found, homogeneous metal (HM), pinball liquid (PL) and threefold charge order (3CO). (b) Evolution of the local densities on the sublattices of the pins (n_C) and balls (n_A and n_B) at $U = 40t$ as a function of V/t. We extracted data from Ref. [33] to draw the case of isotropic Coulomb interaction and hopping integrals.

interaction as we will discuss below, and the evolution of the local electronic density on the sublattice of the pins (n_C) and the balls (n_A and n_B) for comparison with our results in the next chapter.

Let us focus on the original work from Hotta and Furukawa [31]. They considered θ-type organic compounds with a large local Coulomb interaction $U \gg V_{ij}, t$, and anisotropy on the short range Coulomb interaction V_{ij}, with V' in the vertical direction whereas V corresponds to the two other directions, as represented in Figure 1.1, and isotropic hopping integrals. The results that they found with exact diagonalization as a function of the anisotropy are reported in Figure 1.11. The pinball liquid is stabilized around the isotropic case while anisotropy stabilizes stripe orders. The vertical stripes in the area III have a unique classical solution of energy $E_C = V/2$, whereas the disordered stripes in area I are classically degenerate, as there exists a macroscopic number of classical configurations that correspond to the electrostatic energy $E_C = V'/2$. The threefold charge order of the pinball liquid, whose energy is $E_C = (2V + V')/6$, becomes degenerate with the stripe orders at the point $V = V'$. To explain the lifting of degeneracy by quantum fluctuations, the kinetic term is treated perturbatively $V_{ij} \gg t$. The perturbation theory lowers the energy by $E_1 \propto t$ at the first order for the pinball liquid and $E_2, E_2' \propto t^2$ for the disordered and vertical stripes at the second order, reflecting the dominant role of the kinetic effects to stabilize the pinball liquid. The energy of the ground state behaves almost linearly as a function of the Coulomb anisotropy, following the electrostatic energy (the energy of the unperturbed Hamiltonian) and is in good agreement with the perturbation theory.

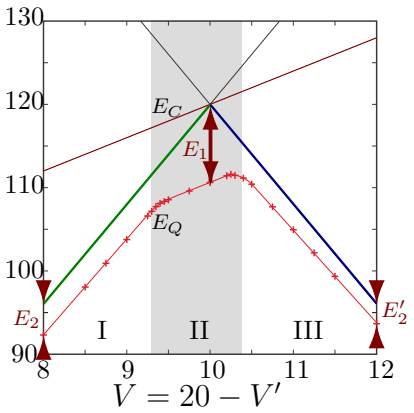

Fig. 1.11 Phase diagram from exact diagonalization for the quarter-filled extended Hubbard model applied to θ-type organic compounds as a function of the Coulomb anisotropy, extracted from [31]. V' is the short range Coulomb interaction in the vertical direction whereas V corresponds to the Coulomb interaction in the two other directions. E_C is the classical electrostatic energy at the fixed value of $V + V' = 20$ as a function of V. The vertical (green) and disordered (blue) striped states are classically realized at $V < V'$ and $V > V'$, with $E_C = V/2$ and $E_C = V'/2$, respectively, while in case of isotropic interactions, at $V = V'$, all states become classically degenerate, including the three sublattice states with $E_C = (2V + V')/6$ becomes degenerate with these stripes. E_Q, the energy of the ground state behaves almost linear with respect to E_C, with the first ($E_1 \propto t$) and second ($E_2, E_2' \propto t^2$) order energy corrections as offset.

This phase was first devised in the context of quarter-filled organic conductors θ-(BEDT-TTF)$_2X$ a decade ago [31] as an original Coulomb-induced charge-ordered metallic phase in the framework of the extended Hubbard model.

Although all these theoretical studies support the existence of such an electronic phase, it has not been observed experimentally in the θ-(BEDT-TTF)$_2X$ materials for which it was originally predicted. This can be attributed to the presence of other competing effects not considered in the idealized theoretical descriptions, most notably deviations from a perfectly isotropic triangular lattice, the interaction with the lattice degrees of freedom [71] and the presence of long-range tails of the Coulomb repulsion beyond nearest neighbors [72, 73], which all favor insulating stripe-ordered states.

We saw in this example how the classical degeneracy of the ground state can be lifted by quantum fluctuations. We mention here that finding a unique ground state is also possible if one considers long-range Coulomb interactions as it has been shown for quarter-filled systems where a global stripe order is stabilized [73].

We can anticipate that a pinball liquid and its dual, the inverse pinball liquid, will be obtained in this dissertation in a more general context, stabilized by multiband effects.

1.3 d-electrons in an octahedral environment

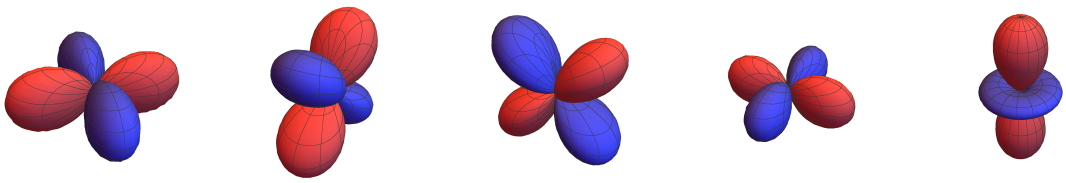

Fig. 1.12 Shapes of the five d-orbitals. The color represents the phase or sign of the wave function. From left to right: xy, yz, xz, x^2-y^2 and $3z^2-r^2$.

As mentioned previously, our focus is on the class of two-dimensional compounds with transition metal ions in an octahedral environment. d-orbitals are split into two sets because of the symmetry O_h of this environment which has two irreductible representations for these orbitals t_{2g} (xz, yz, xy) and e_g $(2z^2-x^2-y^2, x^2-y^2)$[2]. The shape of d-obitals is represented in Figure 1.12.

These two sets are not degenerate because of the crystal-field Δ, i.e. the Coulomb interaction of the other atoms of the crystal. In octahedral environment, t_{2g}-orbitals

[2]In an equivalent way, the orbital $2z^2-x^2-y^2$ is sometimes written $3z^2-r^2$

are lower in energy than e_g-orbitals because the latter face the ligands hence raise their energy due to Coulomb repulsion, whereas e_g-orbitals are lower than the t_{2g}-orbitals in cubic and tetrahedral environments. If the crystal-field is large enough, as we shall assume in the following, the two sets of orbitals can be considered as independent. It is the case for atoms which belong to the first row of transition metals. One can cite two important examples: Nickel and Cobalt.

Each of these sets can be again split into two subsets by the Jahn-Teller effect: a deformation of the octahedra [74], splits the t_{2g}-orbitals into a_{1g} (xy) and e'_g (yz, zx) and the e_g-orbitals into $(2z^2 - x^2 - y^2)$ and $(x^2 - y^2)$ [75]. This deformation can have two modes, each of them corresponding to a different orbital ordering. However, we shall neglect this effect in this work as our focus is on purely electronic interactions and as it seems not relevant experimentally for $2H$-$AgNiO_2$ [10]

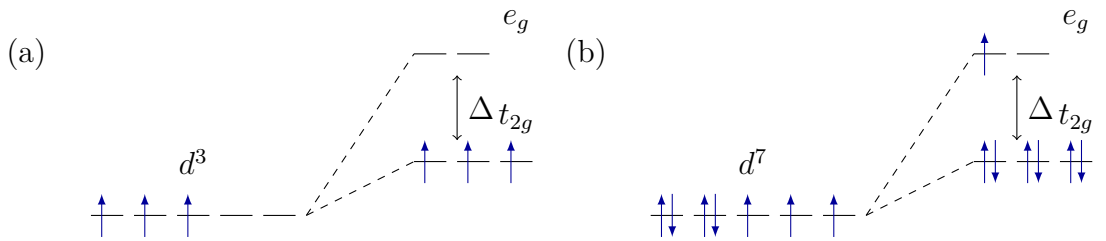

Fig. 1.13 Effect of crystal-field on spin configuration of d-orbitals. (a) The crystal-field does not change the spin configuration for three electrons. (b) For four electrons, the system initially in the high-spin configuration, is in the low-spin configuration for a high crystal-field.

Finally, the crystal field has also an effect on Hund's rule, which is the parallel alignment of spins on an orbital shell, meaning that when a shell is populated, such has d-orbitals, electron will first fill individually different orbitals with the same spin orientation in order to maximize the local magnetization before adding the second electron on the same orbital. However, Hund's rule can be violated for certain fillings due to the crystal field. Let us explain this effect with an example. For three electrons on the d-shell, all of them have the same spin (Hund's rule). When considering the splitting of d-orbitals, the three electrons are on the t_{2g}-orbitals with the same spin and Hund's rule is still valid [See Fig. 1.13 (a)]. Now, if we consider seven electrons, the total spin is 3/2, referred to as a high-spin configuration. However, after the crystal-field splitting, six electrons fill the t_{2g}-orbitals and one electron is on e_g-orbitals. The total spin is now 1/2, which is called a low-spin configuration [See Fig. 1.13 (b)].

Later, we will consider only systems with a filled t_{2g}-shell and a remaining electron on e_g-orbitals. In $2H$-$AgNiO_2$ ($t_{2g}^6 e^1{}_g$ configuration, formal valence Ni^{3+}), for example,

the two sets of orbitals are split by a large crystal-field gap of ~ 2 eV [76, 77, 54] with one electron on the e_g-orbital so that the completely filled t_{2g} triplet can be neglected to a first approximation.

Chapter 2

Multiorbital Hubbard model

2.1 Introduction

Charge-ordered phases realized in a variety of materials can be ascribed to the prominent role of electron-electron interactions. Several theoretical studies have aimed at reproducing the different charge-ordered patterns observed in actual compounds as well as the physical phenomena associated with it (such as quantum criticality, the emergence of superconductivity mediated by charge fluctuations, or the bad metal behavior of the *normal* phases, to cite a few) within the framework of the extended Hubbard model or its generalizations (see Section 2.2), including longer ranged electronic interactions and various types of electron-lattice interactions. In purely electronic model descriptions, i.e. where one does not consider the interaction of electrons with the lattice degrees of freedom, the observation of electronic ordering implies that the magnitude of electron-electron interactions is comparable with the widths of the relevant electronic bands constructed from the molecular orbitals.

Since our main focus is the exploration of novel charge-ordered phases, such as the pinball liquid introduced in the preceding chapter, and the description of experimental compounds such as $AgNiO_2$, we will first derive a general multiorbital extended Hubbard model for d-electrons, where the band structure can be tuned as a function of the microscopic transfer parameters, to resort to a spinless electron description. We shall then introduce a spinless multiorbital extended Hubbard model, as we will justify in Section 2.3, for d-electrons in an octahedral environment. Finally, we will review some previous studies for the single band model for the isotropic spinful Hubbard model then its extension with short-range Coulomb interactions.

2.2 Derivation of an effective electronic model

We derive the multiband extended Hubbard model [78] from a generic electronic Hamiltonian H. We provide the derivation in full details, which allows us to identify the key terms introduced by multiple orbitals, and that will be important in the following. The energy of the system is the sum of the kinetic and potential energies, here related to one- and two-body interactions

$$\begin{aligned} H &= \underbrace{\sum_{\sigma} \int d^3\vec{r}\psi^{\dagger}\left(\vec{r},\sigma\right)\left(-\frac{1}{2}\vec{\nabla}^2 + v_R\left(\vec{r}\right)\right)\psi\left(\vec{r},\sigma\right)}_{K,\text{ Kinetic}} \\ &+ \underbrace{\sum_{\sigma} \int d^3\vec{r}\psi^{\dagger}\left(\vec{r},\sigma\right) V_1\left(\vec{r}\right)\psi\left(\vec{r},\sigma\right)}_{H_1,\text{ One-body}} \\ &+ \underbrace{\sum_{\sigma_1,\sigma_2} \int d^3\vec{r}_1 d^3\vec{r}_2 \psi^{\dagger}\left(\vec{r}_1,\sigma_1\right)\psi^{\dagger}\left(\vec{r}_2,\sigma_2\right) V_2\left(\vec{r}_1-\vec{r}_2\right)\psi\left(\vec{r}_2,\sigma_2\right)\psi\left(\vec{r}_1,\sigma_1\right)}_{H_2,\text{ Two-body}}. \end{aligned} \tag{2.1}$$

where $\sigma = \uparrow, \downarrow$ denotes the spin, $\vec{r}$ is the space degree of freedom and $\psi\left(\vec{r},\sigma\right)$ is the wavefunction.

In order to introduce second quantization in the Hamiltonian, we use atomic orbitals to expand field operators [79], as they form a set of orthogonal functions making the derivation easier. They have the following form

$$\psi\left(\vec{r},\sigma\right) = \sum_{i,m} c_{im\sigma}\phi_{im}\left(\vec{r}\right), \tag{2.2}$$

with $\phi_{im}\left(\vec{r}\right)$ the spacial extension of the orbital m center on site i and $c_{im\sigma}$ is the annihilation fermionic operator of an electron on site i at the m-th orbital with a spin σ. Hence this operator, and its adjoint $c^{\dagger}_{im\sigma}$ the creator fermionic operator, has the following algebra

$$\begin{aligned} \{c_{im\sigma}, c_{jm'\sigma'}\} &= 0, \\ \{c^{\dagger}_{im\sigma}, c^{\dagger}_{jm'\sigma'}\} &= 0, \\ \{c_{im\sigma}, c^{\dagger}_{jm'\sigma'}\} &= \delta_{i,j}\delta_{m,m'}\delta_{\sigma,\sigma'}, \end{aligned}$$

$\delta_{i,j}$ is the Kronecker delta, equal to 1 if variables are equal and 0 otherwise. These fermion anticommutation relations contain Pauli exclusion principle and fermionic statistics.

2.2.1 Kinetic energy

Let us just substitute the atomic orbitals, Equation 2.2, for the kinetic part in Equation 2.1

$$K = -\sum_{i,j}\sum_{m,m'}\sum_{\sigma} t_{ij}^{mm'} c_{im\sigma}^{\dagger} c_{jm'\sigma}, \tag{2.3}$$

which constitute the tight-binding approximation, where i and j denote sites, and

$$t_{ij}^{mm'} = \int d^3\vec{r}\phi_{im}^{*}\left(\vec{r}\right)\left(\frac{1}{2}\vec{\nabla}^2 + v_R\left(\vec{r}\right)\right)\phi_{jm'}\left(\vec{r}\right) \tag{2.4}$$

are the hopping integrals. $v_R\left(\vec{r}\right)$ describes non-interacting electrons in an external potential. K describes electrons moving with transfer integrals $t_{ij}^{\tau\tau'}$ which depend on both the orbital type and on the orientation of the bond (i,j) on the lattice.

If one considers, for example, the approximation of Gaussian orbitals, hopping integrals can be computed analytically in Equation 2.4 and they become proportional to the overlap between orbitals. In pratice, we will consider only the sum over nearest neighbors in Equation 2.3 because of the exponential decrease with the distance of the overlaps.

2.2.2 One-body interaction

The one-body interaction H_1 in the Hamiltonian Equation 2.1 is an approximation that includes the interaction of electrons with the cations, here the nuclei are considered static, and the crystal potential.

Substituting the atomic orbitals, Equation 2.2, in H_1 and taking into account that these orbitals are orthogonal, one obtains

$$H_1 = \sum_{i,m}\sum_{\sigma}\mu_m n_{im\sigma} \tag{2.5}$$

with $c_{im\sigma}^{\dagger}c_{im\sigma} = n_{im\sigma}$ the number operator and

$$\mu_m = \left(\int d^3\vec{r}\phi_{im}^{*}\left(\vec{r}\right)V_1\left(\vec{r}\right)\phi_{im}\left(\vec{r}\right)\right) \tag{2.6}$$

the chemical potential.

Notice that in a non-orthogonal basis of orbitals, off-diagonal terms renormalize the hopping integrals.

We consider that the chemical potential does not depend on the orbital and because we will work at fixed number of particles, H_1 can be explicitly omitted in the following.

2.2.3 Two-body interactions

On-site electron-electron interaction

Charged particles are subject to Coulomb interactions. Because we will describe the properties of conduction electrons, we shall consider that the Coulomb interaction is screened by core electrons as well as the crystal environment

$$V_2\left(\vec{r}_1-\vec{r}_2\right) \propto \frac{1}{\epsilon}\frac{e^2}{|\vec{r}_1-\vec{r}_2|},$$

with e the elementary charge and ϵ the dielectric permittivity that takes into account the screening.

It is customary to consider only the on-site Coulomb interaction when we substitute the atomic orbitals into H_2 from Equation 2.1, non-local interactions will be introduced below. The Coulomb interaction at site i is

$$H_{2,\text{local}} = \frac{1}{2}\sum_i \sum_{m_1,m_2,m_1',m_2'} \sum_{\sigma_1,\sigma_2} c^\dagger_{im_1\sigma_1} c^\dagger_{im_2\sigma_2} c_{im_2'\sigma_2} c_{im_1'\sigma_1} I\left(m_1,m_2,m_2',m_1'\right), \tag{2.7}$$

with

$$I\left(m_1,m_2,m_2',m_1'\right) = \int d^3\vec{r}_1 d^3\vec{r}_2 \phi^*_{im_1}\left(\vec{r}_1\right)\phi^*_{im_2}\left(\vec{r}_2\right) V_2\left(\vec{r}_1-\vec{r}_2\right)\phi_{im_2'}\left(\vec{r}_2\right)\phi_{im_1'}\left(\vec{r}_1\right).$$

Hereafter, we will focus specifically on d-orbitals. One can show that in this case, atomic orbital overlaps have only three nonzero terms due to their axial symmetry [80]. The first nonzero term is $I\left(m,m',m',m\right) = U_{mm'}$, when

$$\begin{cases} m_1 &= m_1' \\ m_2 &= m_2'. \end{cases}$$

The second nonzero term is the Hund's coupling $I\left(m,m',m,m'\right) = J_{mm'}$ for

$$\begin{cases} m_1 &= m_2' \\ m_2 &= m_1' \\ m_1 &\neq m_2. \end{cases}$$

Finally, $I(m, m, m', m') = J'_{mm'}$ with

$$\begin{cases} m_1 &= m_2 \\ m'_1 &= m'_2 \\ m_1 &\neq m'_1. \end{cases}$$

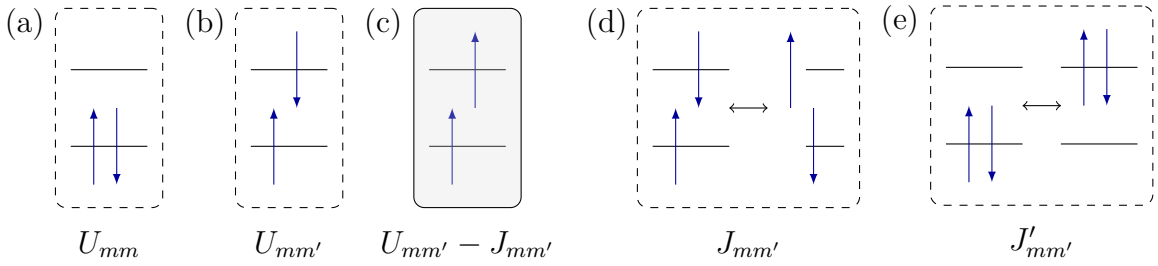

Fig. 2.1 List of all local Coulomb interactions with two orbitals m (lower) and m' (upper) and two electrons. Boxes (a) to (c): Potential energy associated to the state. Boxes (d) and (e): Energy associated to the exchange between the left hand and the right hand of the arrows. Labels from (a) to (e) correspond to the terms from left to right in the right side of Equation 2.8; (a) intraorbital interaction, (b) interorbital interaction with opposite spins, (c) interorbital interaction with same spins, (d) double spin-flip exchange, (e) pair exchange.

Let us now use these conditions in Equation 2.7.

$$\begin{aligned} H_{2,\text{local}} = \frac{1}{2}\sum_i \sum_{m_1,m_2,m'_1,m'_2} \sum_{\sigma_1,\sigma_2} c^\dagger_{im_1\sigma_1} c^\dagger_{im_2\sigma_2} c_{im'_2\sigma_2} c_{im'_1\sigma_1} \Big(U_{m_1m_2}\delta_{m_1,m'_1}\delta_{m_2,m'_2} \\ + J_{m_1m_2}\delta_{m_1,m'_2}\delta_{m_2,m'_1}(1-\delta_{m_1,m_2}) + J'_{m_1m'_1}\delta_{m_1,m_2}\delta_{m'_1,m'_2}\Big(1-\delta_{m_1,m'_1}\Big)\Big) \\ = \underbrace{\sum_{i,m} U_{mm} n_{im\uparrow} n_{im\downarrow}}_{\text{(a)}} + \underbrace{\sum_{i,m<m',\sigma} U_{mm'} n_{im\sigma} n_{im'\bar{\sigma}}}_{\text{(b)}} + \underbrace{\sum_{i,m<m',\sigma} (U_{mm'} - J_{mm'})\, n_{im\sigma} n_{im'\sigma}}_{\text{(c)}} \\ + \underbrace{\sum_{i,m\neq m'} J_{mm'} c^\dagger_{im\uparrow} c^\dagger_{im'\downarrow} c_{im\downarrow} c_{im'\uparrow}}_{\text{(d)}} + \underbrace{\sum_{i,m\neq m'} J'_{mm'} c^\dagger_{im\uparrow} c^\dagger_{im\downarrow} c_{im'\downarrow} c_{im'\uparrow}}_{\text{(e)}}, \end{aligned} \tag{2.8}$$

where $\bar{\sigma}$ denotes the opposite spin of σ. These different terms of Equation 2.8 are illustrated in Figure 2.1. There are three potential terms: it costs an energy (a) U_{mm} to have two electrons on the same orbital m, (b) $U_{mm'}$ to have two electrons on different orbitals m and m' with opposite spins and (c) $U_{mm'} - J_{mm'}$ to have two electrons on different orbitals m and m' with the same spin. There are also two exchange terms: it

takes an energy (d) $J_{mm'}$ to exchange electrons from two orbitals m and m' (notice that they necessarily have opposite spin because the virtual state is forbidden by Pauli principle) and (e) $J'_{mm'}$ to exchange two electrons from orbital m to m'.

Off-site electron-electron interaction

Our next step is to take into account off-site Coulomb interactions in the term H_2. Essentially, we should perform the same procedure as above but without assuming only local interactions

$$H_{2,\text{non-local}} = \frac{1}{2}\sum_{i\neq j}\sum_{m_1,m_2,m'_1,m'_2}\sum_{\sigma_1,\sigma_2} c^\dagger_{im_1\sigma_1}c^\dagger_{jm_2\sigma_2}c_{jm'_2\sigma_2}c_{im'_1\sigma_1} I\left(m_1,m_2,m'_2,m'_1\right), \quad (2.9)$$

and compute the resulting integrals of the form

$$I\left(m_1,m_2,m'_2,m'_1\right) = \int d^3\vec{r}_1 d^3\vec{r}_2 \phi^*_{im_1}\left(\vec{r}_1\right)\phi^*_{jm_2}\left(\vec{r}_2\right)V_2\left(\vec{r}_1-\vec{r}_2\right)\phi_{jm'_2}\left(\vec{r}_2\right)\phi_{im'_1}\left(\vec{r}_1\right).$$

In metals, these integrals are rapidly suppressed with the distance so we will neglect everything beyond the nearest-neighbors. By considering the Coulomb interaction to be isotropic, we obtain

$$H_{2,\text{non-local}} = V\sum_{\langle i,j\rangle}\sum_{m_1,m_2}\sum_{\sigma_1,\sigma_2} n_{im_1\sigma_1}n_{jm_2\sigma_2}, \quad (2.10)$$

where V is the Coulomb repulsion between electrons on neighboring sites. As will be shown, $H_{2,\text{non-local}}$ constitutes the main driving force for charge ordering.

When gathering Equation 2.3, Equation 2.5, Equation 2.8 and Equation 2.9, we obtain the general multiorbital extended Hubbard model

$$H = K + H_1 + H_{2,\text{local}} + H_{2,\text{non-local}}.$$

2.3 Spinless multiorbital extended Hubbard model for d-orbitals

In the preceding section, we have derived a generic multiorbital extended Hubbard model by introducing the second quantization to a general electronic Hamiltonian. This Hamiltonian contains many terms and we will now refine our interest on d-orbitals

Table 2.1 On-site Coulomb interaction inter and intraorbital $U_{mm'}$. The t_{2g} and e_g sets of parameters are highlighted.

m' \ m	xy	yz	zx	x^2-y^2	$3z^2-r^2$
xy	U_1	U_2	U_2	$4U_2-3U_3$	U_3
yz	U_2	U_1	U_2	U_2	$3U_2-2U_3$
zx	U_2	U_2	U_1	U_2	$3U_2-2U_3$
x^2-y^2	$4U_2-3U_3$	U_2	U_2	U_1	U_3
$3z^2-r^2$	U_3	$3U_2-2U_3$	$3U_2-2U_3$	U_3	U_1

t_{2g} e_g

in octahedral environment and make reasonable approximations to reduce the number of free parameters.

The terms $U_{mm'}$ from Equation 2.8 can only acquire three different values for d-orbitals: U_1, U_2 and U_3. They are summarized in Table 2.1. The term $J_{mm'}$, from the same equation, can be deduced from U_{mm} and $U_{mm'}$

$$U_1 - U_2 = 2J \tag{2.11}$$

for t_{2g}-orbitals and

$$U_1 - U_3 = 3J \tag{2.12}$$

for e_g-orbitals.

Let us refine our focus on $2H$-$AgNiO_2$ that we introduced in the previous chapter to try to capture the electronic state. As we mentioned before, nickel atoms have seven d-electrons in an octahedral environment with a strong crystal-field Δ hence the t_{2g}-level is filled with six electrons and only one electron remains on the e_g-orbitals. This separation of energy scales implies that we can restrict to a two-orbital model with one electron per site in average. Let us make an assumption

$$U_{mm} \gg U_{mm'},$$

with $m \neq m'$. In this case, the configurations (a) and (e) in Figure 2.1 are forbidden. In addition, we can see that configuration (c) is lower in energy than configuration (b) because of Hund's coupling. This will be the only configuration that we will retain because if we add a second electron to a site, it will be on the other orbital with the same spin. By this simplification, we obtain an effective spinless model. This approach has been shown to capture the correct ordering patterns realized in

single-band models [31, 33] in the limit of strong local Coulomb repulsion, where the magnetic energy scales are typically much smaller than the ones controlling charge ordering. It has also been successfully used to study charge ordering in the context of multiband models for correlated oxides [81] in the ferromagnetic state.

To summarize, we will consider a spinless model with one electron per site in average on the triangular lattice with e_g-orbitals which are pseudo-spins because they have two states so can be labelled $\tau = \uparrow, \downarrow$. These assumptions imply that we remove the sum over the spin and the index on operators, and the index m becomes τ in Equation 2.3 and Equation 2.9. Equation 2.8 becomes

$$H_{2,\text{local}} \simeq \tilde{U} \sum \sum_{\tau<\tau'} n_{i\tau} n_{i\tau'}, \tag{2.13}$$

following standard notations [82]with $\tilde{U} = U_3$. When this term is dominant, it stabilizes Mott states.

In conclusion, we shall study in the rest of this work the following spinless multiorbital extended Hubbard Model

$$H = -\sum_{\langle ij\rangle,\tau\tau'} t_{ij}^{\tau\tau'} d_{i\tau}^{\dagger} d_{j\tau'} + \text{h.c.} + \tilde{U} \sum_{i=1}^{N_s} \sum_{\tau<\tau'} n_{i\tau} n_{i\tau'} + V \sum_{\langle ij\rangle,\tau\tau'} n_{i\tau} n_{j\tau'}, \tag{2.14}$$

where h.c. stands for hermitian conjugate, N_s is the number of sites, which corresponds also to the number of electrons, in the considered case of half-filling. In the first term, we write the annihilation and creation operator d and $d^{\dagger}$ instead of c and $c^{\dagger}$ because we consider explicitly d-electrons.

Before proceeding further, some remarks are in order. First, considering the effective on-site Hubbard repulsion term in Equation 2.14, which describes the interaction between electrons on different orbitals as we derived in preceding paragraphs, has direct relevance to the study of ferromagnetically ordered states [81], in which case only one spin species is present and two electrons necessarily occupy two different orbitals. In a more general context, the present spinless model can be viewed as an approximation to tackle the strongly interacting limit, i.e. strong Hubbard repulsion *and* strong Hund coupling, of the full two-band spinful model introduced above in Section 2.2.3 and in Ref. [35].

Second, we mention here that although related multiband models with e_g-orbitals for charge and orbital ordering on the triangular lattice have been studied in recent years, how multiorbital kinetic terms affect frustrated charge ordering, in particular the pinball liquid introduced in Section 1.2.3, remains an open question. Vernay, *et*

al. [76], for example, studied the evolution of orbital ordering as a function of t'/t (See Section 3.2) in a spinful model via both mean-field and exact diagonalization, but they did not consider the charge ordering induced by the intersite repulsion V. Uchigaito, *et al.* [59] performed a mean-field analysis of the effects of both the Hund and Jahn-Teller couplings on the electron ordering as a function of t'/t; however, because the repulsion V was not included in the model, no pinball-liquid phase was found at realistic values of the Hubbard repulsion U, which is at odds with the experimental observations in $2H$-$AgNiO_2$ presented in Section 1.1.3. The question has also been addressed from an *ab initio* point of view [83], including both local and nonlocal interaction effects, but without providing systematic studies as a function of the microscopic Hamiltonian parameters. Finally, multiband effects on charge ordering on the triangular lattice have been studied via both unrestricted Hartree-Fock and dynamical mean-field theory in Ref. [35], but only the fully isotropic limit $t' = t$ was explored. From the point of view of the present work, this is a special case where the model becomes equivalent the isotropic spinful extended Hubbard model at half filling with the substitution $\tilde{U}$ by U. We shall come back to this analogy at length in Section 3.2 and Section 3.4.3.

We end this chapter by reviewing some known theoretical results on the standard isotropic spinful Hubbard model on the triangular lattice, and then for the extended Hubbard model.

2.4 State of the art

2.4.1 Single-band Hubbard model at half filling on the triangular lattice

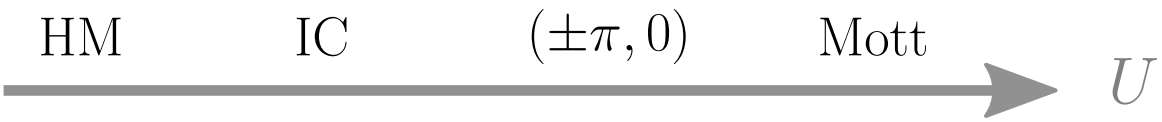

Fig. 2.2 Schematic phase diagram of the Hubbard model at half filling for the triangular lattice. Upon increasing the strength of the on-site Coulomb interactions, the homogeneous metal (HM) goes through an incommensurate phase (IC) then zigzag (modulation of $(\pm\pi, 0)$) and finally to a Mott state.

In this section, we briefly review some results of spinful Hubbard model applied to the isotropic triangular lattice at half filling. The goal is not to be exhaustive but

rather to give an idea of the phases that one can expect in this model, which is one the most studied models of condensed matter.

We start this brief review by two articles [84] and [85], both by Krishnamurthy, Jayaprakash and collaborators. They performed Hartree-Fock calculations and found four phases: a homogeneous metal for $U \in [0, 3.98]$, then an incommensurate phase up to $U = 4.45$, followed by a zig-zag phase (wave vectors $\vec{Q} = (\pm\pi, 0)$) with a critical $U = 6.2$, finally, the so-called 120° phase (wave vector $\vec{Q} = (4\pi/3)$) for higher values of U. This is a broken symmetry phase where spins are ordered with an angle of 120° in the plane.

The slave-boson technique has also been used to study the Hubbard model [86–88]. The system goes from the homogeneous metal to the antiferromagnetic order through the zig-zag phase (Linear Spin Density Wave in these articles) in the range $U \in [6.9, 7.8]$. So no incommensurate phase is found within the slave-boson treatment. Exact diagonalization has also been performed in [88] in addition to the slave boson approach within a finite-size cluster of 12 sites. Only one transition occurs, from the homogeneous metal to the 120° phase at $U_c = 12.07$ using the Drude weight as an order parameter.

A similar behavior as the one predicted by exact diagonalization is found with Dynamical mean-field theory but with a different critical parameter $U_c = 18.2$ [89].

A Variational Monte Carlo study is again consistent with exact diagonalization for a 12-sites cluster and dynamical mean-field theory, i.e. a direct transition from the homogeneous metal to the 120° phase is obtained at a critical parameter $U_c \simeq 8$ [90].

Finally, the Variational Cluster Approach of Ref [91] finds a nonmagnetic insulator between the homogeneous metal and the 120° phase.

To summarize, the accepted view resulting from the existing studies is that the Hubbard model goes from homogeneous metal to an insulating Mott state. Some methods found intermediate phases magnetically ordered, either metallic or insulating, but without finite magnetization. These transitions are summarized in Figure 2.2. Among the methods that we presented, the mean-field approach gives the richest phase diagram as it is usually the case. While it clearly neglects electronic correlations, the mean-field approximation is interesting in that it does not suffer from finite size effects, as very large systems can be accessed with reasonable numerical effort. We shall come back to this point in the next chapter.

2.4.2 Single-band Extended Hubbard model at half filling on the triangular lattice

We now increase the complexity by adding nonlocal Coulomb interactions.

We start this quick review with the extended two-particle self-consistent approach [92]. In this work which presents results at different band filling, we are interested by the half-filled case, $n = 1$. There are only two results, for a value of the local Coulomb interaction of $U = 5$ and $U = 10$ as a function of short range Coulomb interaction V. In the first case, Davoudi *et al.* find a small area of incommensurate charge-density wave between the homogeneous metal (paramagnetic) and a charge-ordered phase with finite charge correlation on K-points. In the second case, they found an incommensurate spin-density wave with a transition to a threefold charge order when increasing the short range Coulomb interaction V.

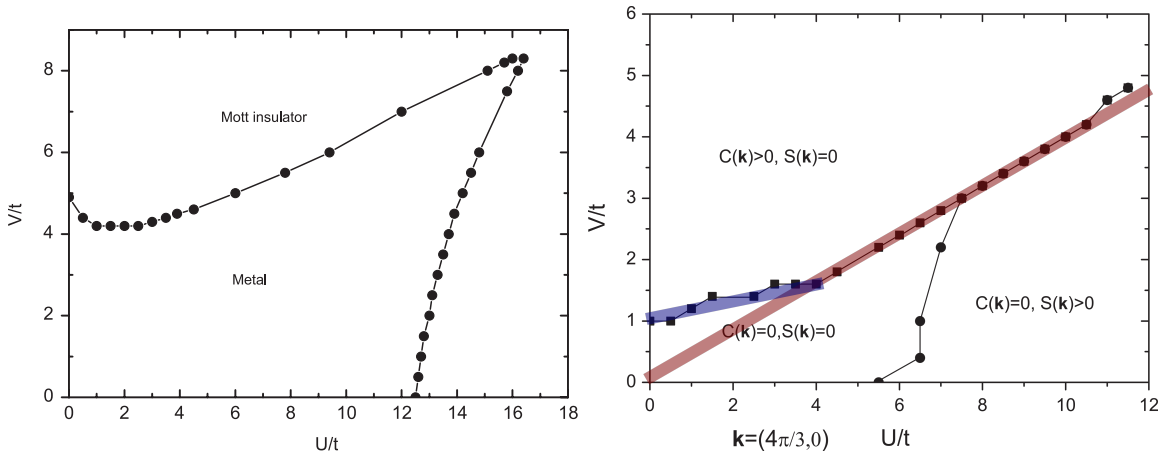

Fig. 2.3 Block renormalization group (BRG) (left) and Hartree-Fock (right) phase diagrams in the $(U/t, V/t)$-plane extracted from [93]. On the right panel, we added the two straight lines according to our analytical estimates (see text).

A phase diagram for the metal insulator transition has been obtained with block renormalization group (BRG) [93]. This phase diagram is reproduced on the left panel in Figure 2.3. When the short-range Coulomb interaction V increases, the transition to a Mott state with a threefold order is pushed to higher values of the local interaction U. In the same work, one can find a restricted Hartree-Fock study. The corresponding phase diagram is reproduced on the right of Figure 2.3. We will see in the next chapter that our results are quantitatively in good agreement with this picture; we recover the same transition to a Mott state with the magnetic structure factor $S(K) > 0$ and to a charge-ordered phase with a charge structure factor $C(K) > 0$. One can notice that for both methods the transition to the threefold Mott state happens at higher value of

local interactions U/t when the short-range Coulomb interaction increases. In addition, we extracted the following transition lines to the charge order from the Hartree-Fock phase diagram that we reported in Figure 2.3

$$V_c\,(U) = \begin{cases} V_c \simeq U/6+1 & , \quad 0 \leqslant U \lesssim 4 \\ V_c \simeq U/3 & , \quad U \gtrsim 4. \end{cases}$$

We will see later, in Section 3.3, that the first line is an evidence of a transition to the pinball liquid phase that we introduced in the previous chapter.

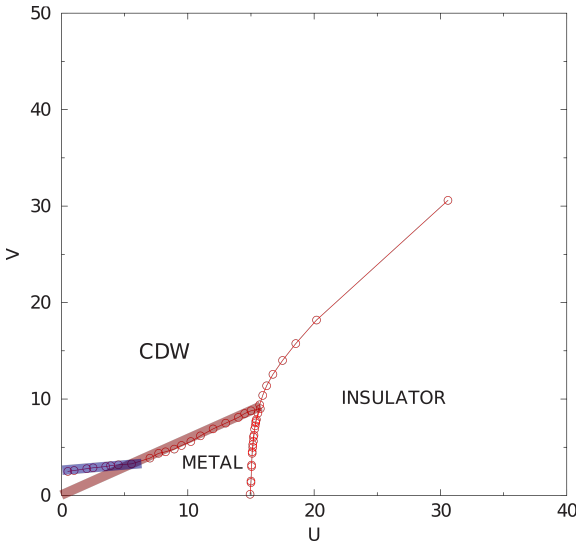

Fig. 2.4 Slave spins Mean-Field phase diagram in the $(U/t, V/t)$-plane extracted from [94]. We added the two straight lines.

One can also cite the slave-spins Mean-Field theory approach [94]. The corresponding phase diagram, reproduced in Figure 2.4, looks consistent with the block renormalization group approach. The stabilization of the metallic state when increasing the short-range Coulomb interaction V is again present with the two different behaviors for the transition to the charge-ordered phase, but with different slopes.

The final work that we review here is done in the context of adsorbates but might be the most interesting for us in the sense that it is the closest model, method and results to our work. Indeed, the authors studied an isotropic spinful extended Hubbard model at half filling on the triangular lattice within mean-field theory [95]. Besides focusing on spinful electrons instead of effective pseudo-spins as we do here, the considered band structure is specific to the adsorbate systems under study, and it includes longer range hopping beyond nearest neighbors (see different noninteracting band structures in Section C.2). Yet, the behavior is expected to be alike, especially at strong interaction

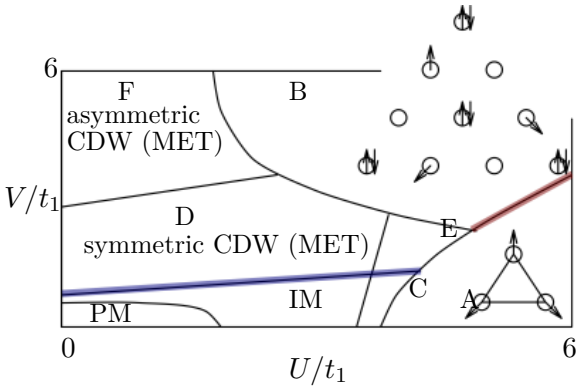

Fig. 2.5 Hartree-Fock phase diagram for the corresponding hopping integrals in the $(U/t, V/t)$-plane. Both figures are reproduced from [95]. We swapped the axes to match the convention for U and V that we will use in this dissertation and we added the two colored straight lines.

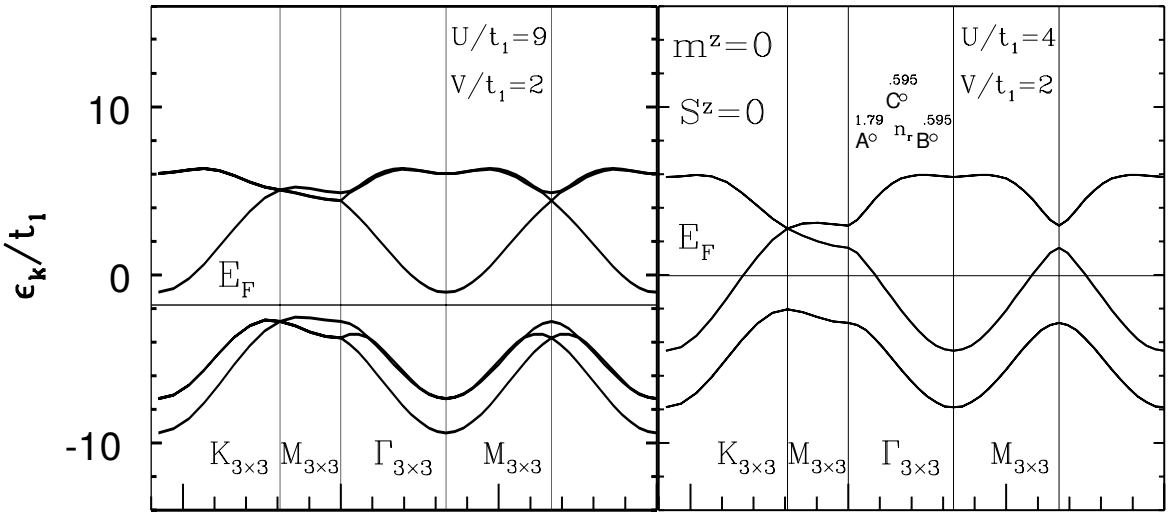

Fig. 2.6 Band structures for the 120° phase (left) and the pinball liquid phase (right) labelled A and D in Figure 2.5 with the hopping integrals in the caption. They are reproduced from [95]. We replotted these band structure on the $\Gamma MK\Gamma$ path and we swapped the sign to match our explicit sign convention in the Hamiltonian for comparison with our results.

where the role of kinetic effects is reduced. Santoro, *et al.* revealed a rich phase diagram, which is reproduced in Figure 2.5 extracted from [95].

First, let us describe the line at $V = 0$. For weak interactions, the system is a homogeneous paramagnetic metal. At large value of the local interaction U, the 120° broken symmetry phase is stabilized (see the corresponding band structure on the left of Figure 2.6). For intermediate values, two other orders appear: incommensurate (IM) and threefold (C) spin order metallic phases.

Now, let us describe the phase diagram for finite V. At strong interactions, they found a threefold charge order with local densities on the three sublattices of respectively 2, 1 and 0 electrons (2-1-0 configuration), with a straight line for the transition from the Mott state (red line), but with an extra 120° spin order on the singly occupied sites. At low on-site interaction but strong nearest neighbor interaction, they found a threefold metallic charge order [F asymmetric CDW (MET)]. We will see below that this phase is an artefact of the method. Indeed, they constrain the system to have at most a nine-site unit-cell. With this constraint, the minimum of the energy is found for a threefold charge order. The band structure is just a folding of the Brillouin zone of the noninteracting case into the reduced Brillouin zone corresponding to the new Bravais lattice. Within this folding, the band structure can not have a gap at the Fermi energy and the system remains metallic even at infinite nearest-neighbor interaction V. To overcome this problem, the constraint on the unit-cell must be removed, i.e. one needs to use an unrestricted version of the Hartree-Fock method. Finally, for intermediate values of nearest-neighbor interaction, and for low on-site interaction, the authors found a metallic phase with threefold charge order, that we identify with the pinball liquid state introduced in Section 1.2.3, where the transition from the paramagnetic metal is a straight line. The local densities of this phase, which are reported in the inset of the band structure plotted on the right panel of Figure 2.6, have the expected pattern for the pinball liquid phase as there is one charge-rich site and two equivalent charge-poor sites. We have highlighted in blue and red the transitions lines to a pinball liquid phase and an insulating threefold charge order 2-1-0.

2.4.3 Multiorbital Hubbard model

As was mentioned earlier, the multiorbital Hubbard model for e_g-orbitals has been studied with one electron per site with Hund's coupling but without considering off-site Coulomb interactions.

We described in Section 1.1.3 the work at mean-field level in the context of 2H-$AgNiO_2$ from Uchigaito and collaborators [59] where they added the lattice interaction

through the phonons but did not consider the nearest neighbor interactions. Let us recall the results of interest to us: around $U/t = 4$ and $J_h/t \simeq 0.25$, even without considering the coupling to phonon, a metallic charge order appears with a small amplitude of the modulation. In addition, this work shows the richness of the multiband model as five phases have been found either metallic or insulating, with different charge patterns, such as homogeneous, threefold and sixfold, magnetic and orbital orders. It is interesting to notice that the only orbital order found for the choice of parameters ($t' = -t$) is ferro-orbital along the y direction in a ferromagnetic state without charge-order.

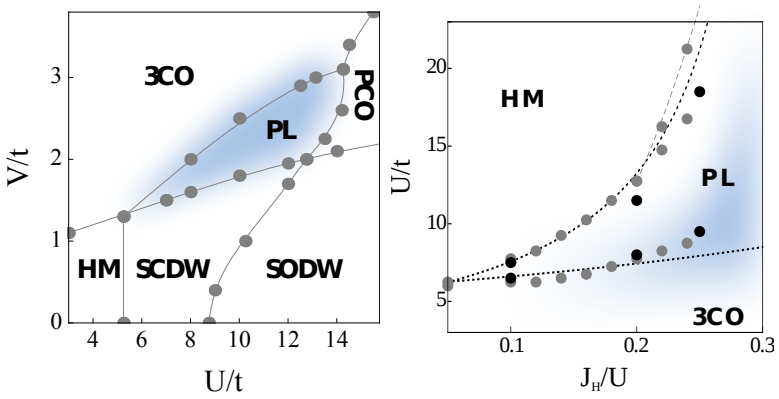

Fig. 2.7 Phase diagrams of the multiorbital extended Hubbard model for e_g-electrons on the triangular lattice obtained from DMFT (black points) and UHF (gray points) in (left) the $(U/t, V/t)$ plane for $J_H/U = 0.2$ and (right) the $(J_H/U, U/t)$ plane $V/t = 2$. These values are highlighted with the thick black dashed line. Both figures are extracted from [35].

The effect of the nearest neighbor interaction with Hund's coupling and e_g-orbitals at a filling of one electron per site (quarter-filled system) has been reported during this thesis in Ref. [35] by Ralko, Merino and Fratini, where they studied the model for isotropic hopping integrals ($t' = t$) using unrestricted Hartree-Fock and dynamical mean-field theory. The effect of the nearest neighbor interactions reveals an even richer phase diagrams (see Figure 2.7) with different charge, magnetic and orbital orders. Among these phases, the pinball liquid is stabilized.

None of these two studies analyzed the influence of the free parameters t and t' related to the electronic structure of the e_g-orbitals. The study of the kinetic effects will be one of the themes of the next chapter. We will study large systems, in contrast to small clusters where discretization does not allow to capture the details of the band structure, and we will use the unrestricted Hartree-Fock method, reliable at weak to moderate values of the interactions where kinetic effects matter.

2.5 Conclusion

In this chapter, we derived a multiorbital Hubbard model from the general Hamiltonian with Coulomb interaction and took the specific case of d-orbitals for large on-site intraorbital Coulomb interaction U. It leads us to a spinless electronic model which describes the interplay between frustrated electron-electron interactions and multiorbital effects on the half-filled triangular lattice.

We have then provided a brief summary of previous work on (i) the single-band Hubbard model, that is of relevance for small values of the nearest neighbor interactions, (ii) the single-band Extended Hubbard model, in cases where non-local interactions are relevant, and (iii) the multiorbital Hubbard model, in the specific case of e_g-orbitals relevant to $AgNiO_2$. Notice that the spinful single-band studies that we presented correspond exactly to our model in the isotropic case $t = t'$.

The next chapter presents a complete study of the model that we derived. The results that will be presented are part of the work published in [34].

Chapter 3

Coulomb-driven charge-ordered phases

3.1 Introduction

The role of the multiorbital effects on the emergence of frustrated electronic orders on the triangular lattice at half filling is investigated through the extended spinless fermion Hubbard model that we derived in the previous chapter. By using complementary approaches, unrestricted Hartree-Fock and exact diagonalizations, we unravel a very rich phase diagram controlled by the strength of both local and off-site Coulomb interactions and by the interorbital hopping anisotropy ratio t'/t. Three robust unconventional electronic phases, the pinball liquid, the inverse pinball liquid, and a large-unit-cell $\sqrt{12} \times \sqrt{12}$ droplet phase, are found to be generic in the triangular geometry, being controlled by the band structure parameters. The latter are also stabilized in the isotropic limit of our microscopic model, which recovers the standard SU(2) spinful extended single-band Hubbard model.

In the first chapter, we introduced various classes of materials with layered triangular lattices and sizable electronic interactions which do present interesting charge-ordered phases whose origin is not fully understood. These include transition-metal oxides such as the triangular nickelates $AgNiO_2$ [9, 11] and Ag_2NiO_2 [45], which show a threefold ordered metallic phase with anomalous metallic properties. Another interesting class is that of transition-metal dichalcogenides. In $1T$-TaS_2, for example, the ordered state displays a marked Mott character induced by charge modulations with a large periodicity of $\sqrt{13} \times \sqrt{13}$ [15, 20], and various other periodicities are found in other compounds (as seen above in Section 1.1.2). What all these materials have in common is that electrons live in bands constructed from d atomic orbitals. Bridging the

ideas of frustrated charge order from their initial domain of application (single-band, layered organic conductors) to such d-electron compounds requires us to account for the presence of multiple bands and to move to electron densities not restricted to one-quarter filling.

Multiband effects come in two different kinds. The first is related to interactions that are present within the d-electron manifold already at the atomic level, most notably the on-site Hund interactions acting on the magnetic degrees of freedom [82] (see previous chapter). These are known to favor the emergence of high-spin states and have been shown to strongly enhance the effects of electronic correlations [96, 97, 2]. Their ability to stabilize a pinball liquid phase with unconventional metallic properties at a filling of one electron per site has been explored very recently [35]. The second type of multiband effect, which can also lead to novel and original properties, is of kinetic origin and has to do with the microscopic form and symmetry of the interatomic electron transfers. One can cite for example the hidden kagome symmetry and flat bands which have been pointed out in the layered cobaltates [98], and which could be related with the experimentally observed Kagome order in these compounds [99, 44].

The purpose of this chapter is to study how such multiorbital kinetic effects influence the frustrated charge order on the triangular lattice. To this aim we employ an atomistic tight-binding description [100] and set up the two-orbital extended Hubbard model introduced in the previous chapter where the band structure can be tuned systematically as a function of the microscopic transfer parameters. Since our main focus is the exploration of novel charge ordered phases, it is a good starting point to resort to a spinless electron description. This approach has been shown to capture the correct ordering patterns realized in single-band models [31, 33] in the limit of strong local Coulomb repulsion, where the magnetic energy scales are typically much smaller than the ones controlling charge ordering. It has also been successfully used to study charge ordering in the context of multiband models for correlated oxides [81] in the ferromagnetic state.

Our results, obtained here at half filling via electrostatic considerations, unrestricted Hartree-Fock (UHF) mean-field theory and exact diagonalization (ED) on small clusters, show the emergence of a rich panel of charge and orbitally ordered phases. Most notably, we find three robust unconventional charge-ordered phases, whose occurrence can be tuned by varying the multiorbital band structure parameters. Two of these phases have peculiar properties since a fraction of the electrons forms a charge order with a threefold symmetry breaking, while the other fraction is free to move on the remaining sites of the lattice, forming a honeycomb structure. These phases are called respectively

the pinball liquid, originally found in quarter-filled lattices and obtained here at half filling, and the inverse pinball liquid, which can be viewed as the dual to the pinball liquid. The third unexpected phase found in this work is the large-unit-cell $\sqrt{12} \times \sqrt{12}$ droplet phase, also found in the isotropic limit where our model reduces to the spinful extended Hubbard model on the triangular lattice, where it was overlooked in previous studies. Such phases could be of relevance to a variety of triangular d-band electron systems such as the cobaltates, nickelates and dichalcogenides.

In this chapter, we will study the model for e_g-orbitals that we derived in the previous chapter using complementary approaches. First, we focus on the noninteracting part of the Hamiltonian to study e_g-orbitals. It will be followed by tight-binding and electrostatic arguments to build a preliminary phase diagram based on the noninteracting limit and the strongly interacting limit. To go beyond classical considerations, we will present the unrestricted Hartree-Fock method before giving a detailed description of the results. Finally, the phase diagrams obtained by the unrestricted Hartree-Fock method will be compare with exact diagonalization studies on small clusters.

3.2 Noninteracting system: Tight Binding studies

In this section, we solve the Hamiltonian Equation 2.14 in absence of interactions. We mentioned before the d-orbitals split into two sets, the t_{2g} and the e_g. From now on, our main interest will be the two e_g orbitals. For a brief discussion of t_{2g}-orbitals, see Appendix B.

The transfer integrals along the lattice vectors $\vec{u}_1 = (1, 0)$, $\vec{u}_2 = \left(1/2, \sqrt{3}/2\right)$, and $\vec{u}_3 = \vec{u}_2 - \vec{u}_1$ can be expressed in terms of two independent parameters t and t' as [100, 76, 59]:

$$t_{\vec{u}_1} = \begin{pmatrix} t & 0 \\ 0 & t' \end{pmatrix}, \; t_{\vec{u}_2} = \begin{pmatrix} t_2 & t_3 \\ t_3 & t_4 \end{pmatrix}, \; t_{\vec{u}_3} = \begin{pmatrix} t_2 & \text{-}t_3 \\ \text{-}t_3 & t_4 \end{pmatrix}$$

with $t_2 = (t + 3t')/4$, $t_3 = \sqrt{3}(t - t')/4$ and $t_4 = (3t + t')/4$. We take t'/t in the interval $[-1, 1]$ as values outside this interval are found by interchanging orbitals $\uparrow$ and $\downarrow$, and set t as the energy unit. Note that for $t' = t$ the kinetic term reduces to two independent instances of the triangular isotropic lattice, and the model becomes analogous to the single-band spinful extended Hubbard model.

Figure 3.1 reports the evolution of the noninteracting density of states (DOS) as a function of t'/t. As soon as $t' \neq t$, the electronic dispersion separates into two

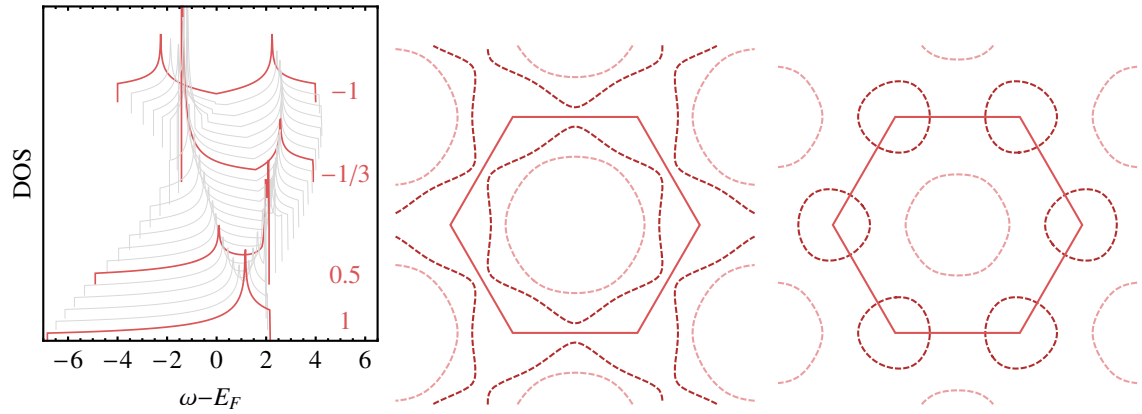

Fig. 3.1 (left) Evolution of the density of states of the noninteracting system with respect to the t'/t ratio, reproduced from [34]. Four specific values are highlighted in bold red, $t'/t = -1, -1/3, 1/2, 1$. Fermi surface, dashed line, at (middle) $t' = 0.5$ and (right) $t' = 0$ with the Brillouin zone, solid line. The two shades of red distinguishes the two bands.

nondegenerate bands. Correspondingly, the logarithmic singularity in the density of states of the triangular lattice splits into two peaks, and Dirac cones appear in the band structure at the K points. The density of states never vanishes at the Dirac points, due to the simultaneous presence of other bands at the same energy; these can be identified in the right plot of Figure 3.1 by the kinks located between the two Van Hove singularities. A Lifshitz transition occurs for $t' \simeq 0.43t$ where the lowest of the two peaks in the density of states crosses the Fermi energy, and one of the two bands changes character from electronlike, with Fermi surface that circles Γ point (see for example the Fermi surface at $t' = 0.5t$ in middle panel of Figure 3.1), to holelike, where the K points are circled in addition to the Γ point (see for example the Fermi surface at $t' = 0$ in right panel of Figure 3.1).

At $t'/t = -1/3$, where t_4 cancels, a flat band is found which gives a strong Van Hove singularity. However, no phase specific to this ratio has been found because this effect is immediately screened by the interactions.

The band structure becomes particle-hole symmetric for $t' = -t$, in which case the Dirac point falls at the band center. In this case, the system is a semimetal with two parabolic bands touching at the Γ point and Dirac cones at the K points.

Further details about the band structure and the Fermi surfaces are given with the description of the spectral function in Section C.2 and the corresponding band structures are plotted with the unrestricted Hartree-Fock results in Section 3.4.2.

Table 3.1 Local mean densities for sites A, B and C of the three sublattices on orbitals $\sigma_i, \sigma_i' = \uparrow, \downarrow$ for the different phases considered for reference: homogeneous metal (HM), Mott state, pinball liquid (PL), inverse PL (IPL), orbital-ordered pinball charge order (PCO_I and PCO_{II}), the pinball charge order (PCO_{III}) and the $\sqrt{12} \times \sqrt{12}$ droplet phase averaged on a three sublattice (see Appendix A). There is no correlation between the filling of the orbitals in one site (i) from one phase to another and (ii) from one sublattice to another, as it does not change the electrostatic energy.

	HM	Mott	PL	IPL	PCO_I/PCO_{II}	$PCO_{III}/\sqrt{12} \times \sqrt{12}$
$A\sigma_A$	1/2	1	1	3/4	1	1
$A\sigma_A'$	1/2	0	1	3/4	1	1
$B\sigma_B$	1/2	1	1/4	3/4	1	1/2
$B\sigma_B'$	1/2	0	1/4	3/4	0	1/2
$C\sigma_C$	1/2	1	1/4	0	0	0
$C\sigma_C'$	1/2	0	1/4	0	0	0

3.3 Electrostatic considerations

In this section, we want to capture the main feature of the phase diagrams with simple physical ideas. To this aim, we evaluate the energy of the system starting from the mean-field value of the Coulomb interactions, and include kinetic energy corrections to the lowest order in the band parameters. Several phases, that will actually be found in our unrestrcited Hartree-Fock calculations, are considered here: (i) the homogeneous metal, composed by a kinetic energy calculated in the tight binding approximation and Coulomb interactions calculated at mean-field level, (ii) the Mott insulator calculated for saturated density patterns corresponding to the classical limit, (iii) the pinball charge order, and the $\sqrt{12} \times \sqrt{12}$ droplet phase which are insulators with only Coulomb interactions, and finally (iv) the inverse pinball liquid, which exhibits both a metallic behavior on the honeycomb lattice for a third of the electrons, with the associated kinetic energy, and the rest forming an insulating charge order.

The considerations presented here will serve as guidance for unrestricted Hartree-Fock and most notably to predict transition lines to charge-ordered phases.

3.3.1 Local electronic densities on a three sublattice

Table 3.1 summarizes the values of local electronic densities in the electrostatic limit for the reference phases considered on a three sublattice (see Appendix A), where we conventionally label the sublattice densities in descending order, $n_A > n_B > n_C$.

- The homogeneous metal (HM) has same filling on every state.
- The Mott state has one electron per site exactly on one orbital only. In this limit, any orbital order has the same energy.
- The pinball liquid (PL) has two electrons on the pins and the balls are filled as a homogeneous metal with the remaining electrons.
- The inverse pinball liquid (IPL) is the dual to the latter as the role of charge-rich and -poor sites are swapped. The pins are filled with two holes (zero electron) while the ball sublattice equally shares the remaining hole (three electrons).
- The orbital-ordered pinball charge order (PCO), corresponding to $\mathrm{PCO_I}$ and $\mathrm{PCO_{II}}$ in the unrestricted Hartree-Fock results (see Section 3.4.2 below), has a threefold 2-1-0 charge pattern.
- The pinball charge order, $\mathrm{PCO_{III}}$, and the $\sqrt{12}\times\sqrt{12}$ droplet phase are considered because they are found in unrestricted Hartree-Fock. The former is similar to the orbital-ordered pinball charge order excepted the absence of orbital order on site B and the latter has a larger unit cell of twelve sites. To allow a direct comparison with the other phases, we averaged densities on the three main sublattices. Remarkably, the average densities on the three sublattice of $\sqrt{12}\times\sqrt{12}$ droplet phase are equal to $\mathrm{PCO_{III}}$, the phase found in previous studies. Nevertheless, these two phases are not equivalent in our effective model because the $\mathrm{PCO_{III}}$ is metallic (see mean-field results in Section 3.4.2).

Finally, we note that at this level of approximation, orbitals $\sigma_i, \sigma_i' = \uparrow, \downarrow$ on a row in Table 3.1 are not correlated from on column to another. For example $B\sigma_i$ can be on $\uparrow$ for the Mott state and $\downarrow$ for the PCO. Moreover, these are not correlated from one sublattice to another in the electrostatic limit.

3.3.2 Energies

In order to build the phase diagram, we shall compute the energy of the different phases as a function of the different parameters $(V, \tilde{U}, t', t)$. Then we compare the energy of each phase to compute the transition lines.

The energies of the different phases are the sum of their kinetic energy computed from the tight binding model, in other words the sum of the N_e[1] first eigenstates of the

[1] N_e is the number of electrons

kinetic term, and the electrostatic energy, also referred as mean-field classical energy, which is equal to the cross term in the Hartree approximation except for the sign (see Section 3.4.1)

$$E^s = \frac{\tilde{U}}{3} \sum_{i=A,B,C} n_{i\uparrow} n_{i\downarrow} + V \sum_{i \neq j \in \{A,B,C\}} \left(n_{i\uparrow} + n_{i\downarrow}\right)\left(n_{j\uparrow} + n_{j\downarrow}\right). \tag{3.1}$$

In Equation 3.1, we substitute the $n_{i\sigma}$ terms by their value in Table 3.1 for each phases.

As mentioned above, the homogeneous metal has a constant kinetic energy K_{HM} which is easily computed in the tight binding approach. Its energy using Equation 3.1 and Table 3.1 is

$$E_{\mathrm{HM}} = K_{\mathrm{HM}} + \frac{1}{4}\tilde{U} + 3V,$$

with $K_{\mathrm{HM}} = -1.581t$ for $t' = 0.5t$.

The effective model to describe the pinball liquid is an insulating threefold charge order with two electrons per pin, so two electrons per three sublattices (see Appendix A), and a tight binding model on the honeycomb lattice at quarter filling, i.e. the remaining electron on the two sites with two orbitals of the three sublattices. Equivalently for the inverse pinball liquid, no electrons on pins and three electrons on the two other sites making a three-quarter-filled honeycomb lattice.

One can check if other fillings of charge-rich and charge-poor sites are electrostaticaly lower in energy by introducing a charge disproportionation δ on balls of the honeycomb lattice ($n_A = n_B$) and pins of charge order (n_C)

$$n_A = n_B = 1 + \delta, \tag{3.2}$$

$$n_C = 1 - 2\delta \tag{3.3}$$

which recovers both pinball liquid and inverse pinball liquid. The mean-field electrostatic energy $E^s_{\mathrm{IPL}} = E^s_{\mathrm{PL}} = \frac{\tilde{u}}{5}\left(1 + 2\delta^2\right) + 3V\left(1 - \delta^2\right)$, the same in both case, has two minima: $\delta = 1/2$ (inverse pinball liquid) and $\delta = -1/2$ (pinball liquid).
The two phases have both the same Coulomb repulsion, and kinetic energy $K_{\mathrm{honeycomb}}$ within this approach

$$E_{\mathrm{PL}} = E_{\mathrm{IPL}} = K_{\mathrm{honeycomb}} + \frac{3}{8}\tilde{U} + \frac{9}{4}V,$$

with $K_{\mathrm{honeycomb}} = -1.140t$ for $t' = 0.5t$.

The Mott state, which can have various orbital orders such as incommensurate orders or the 120° phase, is assumed to be an insulator; its energy is

$$E_{\text{Mott}} = 3V.$$

The orbital-ordered pinball charge-ordered phases, PCO_{I} and PCO_{II}, referred as PCO later, are insulating as well because of the orbital order, as can be seen from the gap proportional to $\tilde{U}$ in the band structures in Figure 3.9 and Figure 3.10. Their energy is therefore purely electrostatic and equals

$$E_{\text{PCO}} = \frac{1}{3}\tilde{U} + 2V.$$

The band structure of the $\sqrt{12} \times \sqrt{12}$ droplet phase, also displayed in Figure 3.12, shows the insulating gap proportional to the short range Coulomb interaction V. Its energy is

$$E_{\sqrt{12}\times\sqrt{12}} = \frac{5}{12}\tilde{U} + 2V.$$

Finally, we do not consider the PCO_{III} because of its absence in the phase diagram both with unrestricted Hartree-Fock and exact diagonalization approach.

3.3.3 Qualitative phase diagram

Within the present treatment, a first order phase transition happens when two phases have the same energy. Let us start with the metal insulator transition (MIT) from homogeneous metal to Mott state

$$E_{\text{HM}} = E_{\text{Mott}} \Rightarrow \tilde{U}_c = -4K_{\text{HM}}.$$

The transition between the Mott state and the pinball charge order follows the line

$$V_c = \frac{1}{3}\tilde{U}.$$

The transition line between the homogeneous metal and the inverse pinball liquid is predicted as follows

$$V_c = \frac{\tilde{U}}{6} + \frac{3}{4}\left(K_{\text{honeycomb}} - K_{\text{HM}}\right).$$

From the pinball charge order to the $\sqrt{12}\times\sqrt{12}$ droplet charge order, we find a straight vertical line at the origin

$$\tilde{U}_c = 0.$$

So the $\sqrt{12}\times\sqrt{12}$ droplet charge order will exist only for $\tilde{U}_c = 0$ and the transition to the inverse pinball liquid will happen for

$$V_c = -4K_{\text{honeycomb}}.$$

Let us finish with the transition from inverse pinball liquid to the pinball charge order

$$V_c = -4K_{\text{honeycomb}} - \frac{1}{6}\tilde{U}.$$

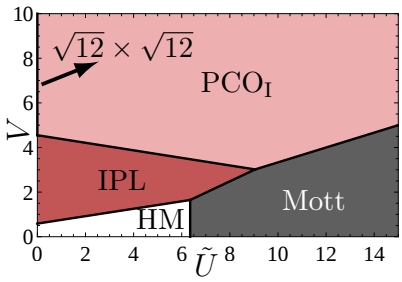

Fig. 3.2 Static phase diagram derived from the effective model.

We now gather these lines to draw the phase diagram in the $\left(\tilde{U}, V\right)$ plane displayed in Figure 3.2. We found with such simple considerations many features such as (i) a metal insulator transition, (ii) while V increases, a transition from inverse pinball liquid to either the $\sqrt{12}\times\sqrt{12}$ droplet phase ($\tilde{U}=0$) or the orbital-ordered pinball charge order ($\tilde{U}>0$) (iii) a vertical transition between the two latter (iv) transitions from the homogeneous metal and Mott state to the charge-ordered phases, the inverse pinball liquid and the PCO$_\text{I}$. Notice that we choose the phases, inverse pinball liquid, $\sqrt{12}\times\sqrt{12}$ droplet phase and PCO$_\text{I}$, rather than other equivalent states in this model according to the unrestricted Hartree-Fock results.

So far, we studied two limits, noninteracting and strong interactions, which can lead to original phases if in competition. To study this interplay for intermediate values of interaction, we need approaches that properly include both the kinetic energy and the Coulomb interactions.

3.4 Unrestricted Hartree-Fock

The Hubbard model for an infinite system can not be solved exactly in general, even though it is possible in some special case such as using the Bethe ansatz in one-dimension [101] or without interaction as we did previously in Section 3.2. Apart from these two cases, one can either diagonalize the Hamiltonian for a finite system, in practice the size of the cluster is small (see Section 3.5), derive an effective model we can solve exactly (see a brief introduction in Section 3.3) or make approximations.

One of these approximations is the mean-field theory, a self-consistent equation of a one-body problem which is a fixed point problem. The Hubbard model for the half-filled triangular lattice has been already studied using mean-field theory. However, these previous works were assuming a given unit cell for the ordered states in order to work in reciprocal space and diagonalize the mean-field Hamiltonian. As this construction is not simple, because it depends on the chosen unit cell and larger unit cells involve more complicated construction, only three- and nine-site unit cell have been considered [93, 95]. These guesses were actually relatively accurate because most phases respect these symmetries. However, in this work, we chose to explore all possibilities and, without making any assumption, to work directly in real space. This allows us to study the different kinetic terms seen in Section 3.2 that can break any symmetry. This is called unrestricted Hartree-Fock.

3.4.1 Method

We will now introduce the method. The main idea is to decouple the mean value of the product of the number operator

$$\langle n_{i\tau} n_{j\tau'} \rangle \simeq \langle n_{i\tau} \rangle \langle n_{j\tau'} \rangle. \tag{3.4}$$

There are two different ways to do this that we present below.

Hartree approximation

One can first neglect the product of the local density fluctuations. Let us rewrite the density operator $n_{i\tau}$ as the sum of its mean value $\bar{n}_{i\tau} = \langle n_{i\tau} \rangle$ and the deviation to the latter, i.e. the fluctuation $\delta_{i\tau} = n_{i\tau} - \bar{n}_{i\tau}$,

$$n_{i\tau} = \bar{n}_{i\tau} + \delta_{i\tau}.$$

Now, product of density operators is

$$n_{i\tau}n_{j\tau'} = \bar{n}_{i\tau}\bar{n}_{j\tau'} + \bar{n}_{i\tau}\delta_{j\tau'} + \delta_{i\tau}\bar{n}_{j\tau'} + \underbrace{\delta_{i\tau}\delta_{j\tau'}}_{\simeq 0},$$

where the last term is neglected. We just have to write explicitly the mean value and the fluctuation in term of operator $n_{i\tau}$ which leads to the following transformation in the Hamiltonian

$$n_{i\tau}n_{j\tau'} \to n_{i\tau}\langle n_{j\tau'}\rangle + \langle n_{i\tau}\rangle n_{j\tau'} - \langle n_{i\tau}\rangle\langle n_{j\tau'}\rangle. \tag{3.5}$$

It is the Hartree term and it directly satisfies the condition in Equation 3.4.

The Coulomb interaction has two types of terms: $\langle n_{i\tau}\rangle\langle n_{j\tau'}\rangle$ and $n_{i\tau}\langle n_{j\tau'}\rangle$. The first term, that we shall denote as "crossed term", is just a shift of the energy which will be omitted in the self-consistent procedure described below because the energy is defined with respect to an arbitrary constant. So, only the second term is relevant to address the problem. A simple view of the new problem with two orbitals τ and τ' is the following: if we have an electron on the orbital τ of the site i, it will see the electrostatic mean-field $\langle n_{i\tau'}\rangle$. So it will cost an energy $\tilde{U}\langle n_{i\tau'}\rangle$, the mean-field produced by the other electrons, to the system to have an electron on this orbital. Otherwise, i.e. if there is no electron on this orbital, the local electrostatic mean-field will not cost any energy to the system. This electrostatic mean-field, which is the classical Coulomb interaction, will overcome the kinetic term, thus, this approximation gives the electrostatic limit for strong interactions. One shall find for instance a Mott state at strong $\tilde{U}$ ($\tilde{U} \gg t', t$ and $\tilde{U} > 3V$) and a charge-ordered state with an energy $E/N_s = \tilde{U}/3 + 2V$ at strong V ($\tilde{V} \gg t', t$ and $V > \tilde{U}/3$), see Section 3.3.3.

Fock approximation

We want to make a better approximation, the Hartree-Fock approximation. We keep the condition on the product of density operators (see Equation 3.4) but we improve the transformation in Equation 3.5 with the unrestricted Hartree-Fock, The idea of this improvement is to add an exchange term to the uncoupled density operators

$$\begin{aligned} n_{i\tau}n_{j\tau'} \to n_{i\tau}\langle n_{j\tau'}\rangle + \langle n_{i\tau}\rangle n_{j\tau'} - \langle n_{i\tau}\rangle\langle n_{j\tau'}\rangle \\ - \left(\langle d^\dagger_{i\tau}d_{j\tau'}\rangle d^\dagger_{j\tau'}d_{i\tau} + d^\dagger_{i\tau}d_{j\tau'}\langle d^\dagger_{j\tau'}d_{i\tau}\rangle - \langle d^\dagger_{i\tau}d_{j\tau'}\rangle\langle d^\dagger_{j\tau'}d_{i\tau}\rangle\right). \end{aligned} \tag{3.6}$$

One can cite the first derivation in 1951 by Roothaan [102] and one of the earliest studies in 1965 for a cubic lattice [103]. The Fock term has two main effects. First, it allows non-classical electrostatic solutions at strong, even infinite, interactions. The best known example is the 120° phase of the Hubbard model because the mean-field parameters in this case for the Hartree term are the polarization along z and the Fock term adds the x and y components of the magnetization required to find this specific phase. The second effect appears with the short-range Coulomb interaction. The Fock terms have the same form than the kinetic operators so that they actually renormalize the kinetic energy of the system; formally $t_{ij}^{\tau\tau'}(V) = t_{ij}^{\tau\tau'} + V\langle d_{j\tau'}^{\dagger} d_{i\tau}\rangle$. Let us now write the multiorbital extended Hubbard model in the mean-field approximation

$$
\begin{aligned}
H^{\mathrm{HF}} &= -\sum_{\langle ij\rangle,\tau\tau'} t_{ij}^{\tau\tau'} d_{i\tau}^{\dagger} d_{j\tau'} + \mathrm{h.c.} \\
&\quad + \tilde{U} \sum_{i=1}^{N_s} \sum_{\tau<\tau'} \left(n_{i\tau}\langle n_{i\tau'}\rangle + \langle n_{i\tau}\rangle n_{i\tau'} - \langle n_{i\tau}\rangle\langle n_{i\tau'}\rangle \right. \\
&\quad \left. - \left(\langle d_{i\tau}^{\dagger} d_{i\tau'}\rangle d_{i\tau'}^{\dagger} d_{i\tau} + d_{i\tau}^{\dagger} d_{i\tau'} \langle d_{i\tau'}^{\dagger} d_{i\tau}\rangle - \langle d_{i\tau}^{\dagger} d_{i\tau'}\rangle\langle d_{i\tau'}^{\dagger} d_{i\tau}\rangle \right) \right) \\
&\quad + V \sum_{\langle ij\rangle,\tau\tau'} \left(n_{i\tau}\langle n_{j\tau'}\rangle + \langle n_{i\tau}\rangle n_{j\tau'} - \langle n_{i\tau}\rangle\langle n_{j\tau'}\rangle \right. \\
&\quad \left. - \left(\langle d_{i\tau}^{\dagger} d_{j\tau'}\rangle d_{j\tau'}^{\dagger} d_{i\tau} + d_{i\tau}^{\dagger} d_{j\tau'} \langle d_{j\tau'}^{\dagger} d_{i\tau}\rangle - \langle d_{i\tau}^{\dagger} d_{j\tau'}\rangle\langle d_{j\tau'}^{\dagger} d_{i\tau}\rangle \right) \right) \qquad (3.7) \\
&= -\sum_{\langle ij\rangle,\tau\tau'} t_{ij}^{\tau\tau'}(V)\, d_{i\tau}^{\dagger} d_{j\tau'} + \mathrm{h.c.} + \tilde{U} \sum_{i=1}^{N_s} \sum_{\tau\tau'} \left(n_{i\tau}\langle n_{i\tau'}\rangle - \langle d_{i\tau}^{\dagger} d_{i\tau'}\rangle d_{i\tau'}^{\dagger} d_{i\tau} \right) \\
&\quad + V \sum_{\langle ij\rangle,\tau\tau'} \left(n_{i\tau}\langle n_{j\tau'}\rangle + \langle n_{i\tau}\rangle n_{j\tau'} \right) + \mathrm{CT} \qquad (3.8)
\end{aligned}
$$

where CT stands for cross terms and all products of mean values, implicitly multiplied by the identity matrix.

One can see that there is no approximation on the kinetic term, which will be a key point to find new physics.

Self-consistent algorithm

Let us briefly introduce the self-consistent algorithm, its flowchart is given Figure 3.3.

The first step is to initialize the mean-field parameters which are $\langle d_{i,\tau}^{\dagger} d_{j,\tau'}\rangle$, $i, j \in [1, N_s]$ and τ, τ' are the orbitals, in our case of e_g-orbitals we label them $\uparrow, \downarrow$ but the formula is easy to generalize for multiorbital spinless systems. In order to optimize the convergence of the method, we consider two types of initial values of the mean-field

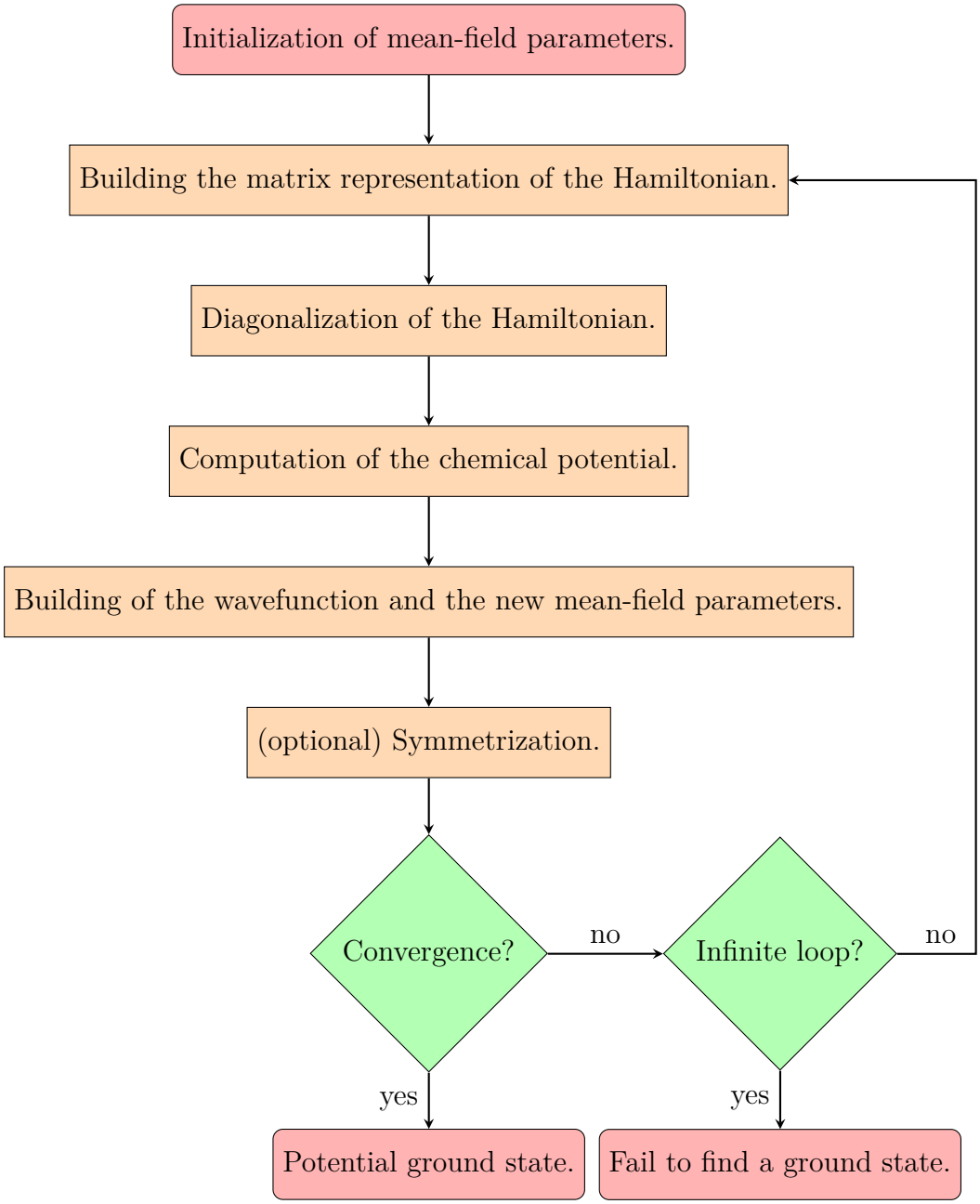

Fig. 3.3 Flowchart of unrestricted Hartree-Fock algorithm.

parameters, either random nonzero complex numbers[2] or ordered state by setting manually their value with an initial guess that one can expect from the considerations of Section 3.3.

The second step is to build the matrix representation of the Hartree-Fock Hamiltonian H^{HF} with these parameters in the basis of one particle states $d^\dagger_{i\tau}|0\rangle$.

The third step is to diagonalize this matrix. For this purpose, we can use efficient libraries as described below. These routines provide all we need, i.e. the eigenvalues ϵ_κ and their associated eigenvectors $\tilde{d}^\dagger_\kappa|0\rangle = \sum_{\kappa'} \alpha_{\kappa\kappa'} d^\dagger_{\kappa'}|0\rangle$. The index κ denotes an eigenstate of the Hartree-Fock Hamiltonian in the range $[1, N_s N_o]$, with N_o the number of orbitals, and κ' denotes the pair of indices i, τ. The wavefunction of a mean-field Hamiltonian is a single Slater determinant

$$|\psi\rangle = \sum_{\kappa=1}^{N_o N_s} f_{FD}\left(\epsilon_\kappa, \mu, T\right) \tilde{d}^\dagger_\kappa|0\rangle. \tag{3.9}$$

$f_{FD}\left(\epsilon_\kappa, \mu, T\right)$ is the Fermi-Dirac distribution, where T is the temperature and μ the chemical potential which must be computed accurately at each iteration.

To compute the chemical potential μ, one should satisfy the following condition

$$\sum_{i=1}^{N_s} \sum_{\tau} \langle n_{i\tau} \rangle = N_e.$$

Notice that computing the chemical potential is required to work with a fixed number of particles. One can also fix directly the chemical potential to compute the compressibility (see discussion Appendix C.1).

At zero temperature, the Fermi-Dirac distribution becomes a Heaviside step function and the chemical potential is equal to the Fermi energy. In this case, building the new mean-field wavefunction is easier as, first, the chemical potential step is skipped and, second, the sum in Equation 3.9 is truncated and becomes the sum on the N_e first eigenstate $\tilde{d}^\dagger_\kappa|0\rangle$.

Using the wavefunction we compute the new mean-field parameters $\langle\psi|d^\dagger_{i,\tau} d_{j,\tau'}|\psi\rangle$.

The last step is to check the convergence of the self-consistent algorithm, that will be discussed below in Section 3.4.1. If it did not converge, we start the algorithm at the second step by building the new mean-field Hamiltonian with the updated mean-field parameters. We repeat the loop until convergence.

[2] real numbers for the density operators which are diagonal.

In the code we developed, we included fast linear algebra libraries that contain eigensolvers. Especially, we used LAPACK (Linear Algebra PACKage)[3] [104] convenient for very large matrices of dimension more than 10^5 that can be coupled with ATLAS [105–110] or OpenBLAS [111, 112]. For smaller systems, e.g. 72×72 cluster which makes a 10368×10368 matrix, faster libraries exist, such as Eigen [113] and, even faster, Armadillo [114] but the container can not handle very large matrices as LAPACK does.

The method is free from local constraints and *ad hoc* symmetrizations of the solution; that is, no particular form of the ground state is assumed. This allows us to obtain the most general ordered states of the model in an unbiased way and has been proved very successful in predicting novel phases in related models [115, 35].

However, the algorithm can be trapped in an infinite loop where the mean-field parameters oscillate between two, or more, excited states. To avoid this effect, one can use symmetrizations, an average of mean-field parameters on a subcluster that can help the convergence by adding constrains. These symmetrizations are explained in Appendix D. Another approach consist on mixing wavefunctions of previous iterations with different weights. For example, the wavefunction at iteration m when mixing the M previous states with exponential decay of characteristic length λ is $|\psi\rangle = \frac{1}{\sum_{x=1}^{M} e^{-m/\lambda}} \sum_{x=1}^{M} |e^{-m/\lambda}\psi_{m-x}\rangle$.

A summary of the algorithm is depicted in Figure 3.3. In cases where we performed symmetrizations; it was typically on 1, 3, 6, 9, 12, 24, 36, 48 sites. In practice, we launched many runs for each set of parameters. Each of these runs are initiated with different mean-field parameters. They can be either random, the results from a close set of parameters (typically used when scanning) or corresponding to an ordered state, guess or state found previously. The order is only initialized in the local electronic densities, the off-diagonal parameters are always random. In any case, a randomness is added to these parameters at the first iteration, see Figure 3.4.

Because unrestricted Hartree-Fock is a fixed point problem, we also used the Broyden's method during iterations, a quasi-Newton method [116]. The idea is to iteratively compute the Jacobian of the system. It can also suffer of oscillation effect and does not necessarily converge but works efficiently in some cases where the previous algorithm does not.

Although our focus here is on zero temperature properties, each run is performed at zero and finite temperature. The temperature will typically melt the orders to favor metallic states, making the transition lines pushed to higher values of the Coulomb

[3]One can cite especially the functions zheev, zheevd (Divide and conquer) and zheevr (Relatively Robust Representations)

interactions. Some exceptions exist where increasing the temperature will stabilize charge orders, e.g. in quarter-filled compounds [117]. In our case, we took temperatures low enough to have a negligible effect on the physics, both qualitatively and quantitavely, typically, up to an inverse temperature of $\beta = 100$. This small temperature is mandatory in case of an open shell, i.e. when the Fermi level, of energy E_f, is degenerate and not all degenerate states are filled, because it will mix properly the ensemble of states of energy $\epsilon_\kappa = E_f$. The runs are also performed for the different symmetrizations. We do this because the unrestricted runs sometimes fail to find a solution and to avoid as much as we can the spurious solutions, i.e. local minima. Among all converged states, we choose the one with the lowest energy.

Convergence criteria

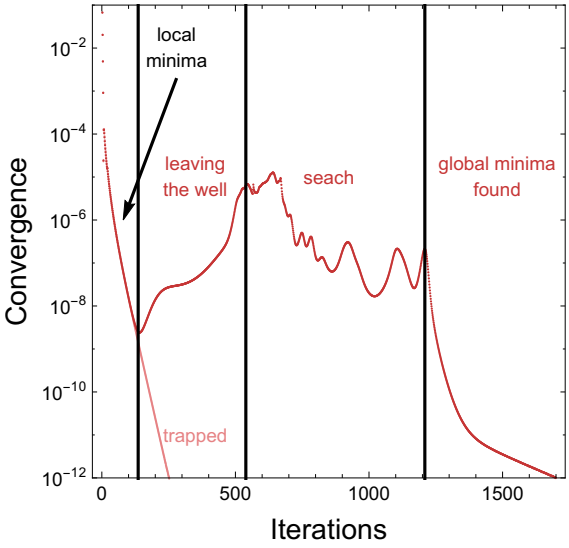

Fig. 3.4 Typical behavior of the convergence criterion ΔE, defined in Equation 3.11, during the self-consistent procedure. In this example, we launch two runs, one with ordered local densities and the other one with the same starting point but with randomness added at the first iteration. The behavior in both cases looks very similar. Due to the (almost) symmetric starting point, the routine converges to a local minimum. Without randomness, the routine is trapped whereas the other run leaves the local minimum, then searches for other ones before finding the global minimum.

The criterion used to characterize the convergence is an important parameter of the algorithm often overlooked. In the literature, this criterion is not necessarily defined [84, 85, 95, 93, 33, 34] and if it is, the cut-off used is rarely given. A criterion often used to check the convergence of the self-consistent field is based on the difference

in the mean-field parameters between two iterations [118]. It has the same form than the variance

$$\frac{1}{N}\sum_i \left|n_i^m - n_i^{m+1}\right| < C, \tag{3.10}$$

with n_i^m a mean-field parameter at the m-th iteration and C the cut-off, which varies from one work to another. Typical values are of the order 10^{-4} [118]. This criterion has three major weaknesses. First, the cut-off is usually restrictive enough and an ordered starting point has a good chance to be considered has a fixed point because the convergence might be exponential at first. As shown in Figure 3.4, any cut-off higher than 10^{-8} will be trapped and this behavior can happen even below 10^{-12}. Setting C to 10^{-14} seems safe and will avoid many of the spurious fixed points[4]. The second issue is that it does not take into account that the computed Hartree-Fock energy E^{HF} at a given iteration can be much lower than the ground state. It is possible because even though the Hartree-Fock energy for a converged state is necessarily greater or equal than the ground state, it is a variational energy, no constraint exists on the Hartree-Fock energy during the iteration process. Technically, it is because the states at iteration $m+1$ are calculated based on the mean-field Hamiltonian defined at iteration m. The last problem is that it does not constrain the Hartree-Fock energy E^{HF} to be equal to the energy of the system $E = \langle \mathrm{HF}|H^{\mathrm{HF}}|\mathrm{HF}\rangle$. The latter is a proper definition of the variational energy, which is correct even for an unconverged state. To ensure the two energies are equal, we choose the following criterion

$$\Delta E = \left|\frac{E^{\mathrm{HF}} - E}{E}\right| < 10^{-14}. \tag{3.11}$$

The Hartree-Fock energy is the sum of the eigenvalues of the mean-field Hamiltonian weighted by the Fermi-Dirac distribution

$$E^{\mathrm{HF}} = \sum_{i=1}^{N_o N_s} f_{FD}\left(\epsilon_i^m, \mu, T\right)\epsilon_i^m.$$

The energy of the system is computed with the mean-field parameters at the $m+1$-th iteration while the Hartree-Fock energy is computed with the mean-field parameters at the m-th iteration.

Notice that we do not set an upper cut-off on the number of iterations. For intermediate values of interaction, the number of iterations required until convergence

[4]Notice that the convergence parameter is limited by the numerical precision; in our system, we reach the numerical noise for double precision in C++ around 10^{-28}.

can be large, typically more than 10^5 iterations even with a good starting point. The evolution of the convergence criterion ΔE, defined in Equation 3.11, using the self-consistent procedure is plotted in Figure 3.4. In this example, we launch two runs, one with ordered local densities and the other one with the same starting point but with randomness added at the first iteration. Due to the (almost) symmetric starting point, the routine converges to a local minimum where the behavior in both cases looks very similar. Without randomness, the routine is trapped whereas the other run leaves the local minimum then searches for other ones before finding the global minimum.

Finally, we have performed a systematic size-scaling analysis for clusters up to 72×72 sites in order to identify transition lines in the thermodynamic limit.

As we briefly discussed previously, mean-field studies assume a unit-cell, generally 3 or 9 for the triangular lattice and then treat the Hamiltonian in reciprocal space. The benefit is that there are no constraints on the size of the reciprocal space, in other words it is easier to reach the thermodynamic limit. However, the solution that is found necessarily respects the symmetries of the assumed unit-cell. The unrestricted Hartree-Fock does not have any assumption on the solution. It means that all symmetries can be broken which implies the solution can have any unit-cell compatible with the cluster. The drawbacks are first that it is very difficult to identify an incommensurate phase: the solution will be different for each cluster, defined by its periodic bondary condition vectors (see Appendix A.1.2), but the vector associated to the incommensurate modulation should convergence when the size of the cluster increases. The second drawback is that the convergence is more difficult and might not be reached. Finally, if two phases are degenerate in the limit of infinite interactions, i.e. if they have the same electrostatic energy and so are distinguished only by kinetic effects, it means the relative energy difference between these two states becomes smaller while Coulomb interactions increase and thus the Hartree-Fock method will reach its numerical limit when the numerical uncertainty is the order of magnitude of the difference between two electrostaticaly degenerate states. In this case, it will be difficult for unrestricted Hartree-Fock method to distinguish a local minima from the mean-field ground state.

3.4.2 Unrestricted Hartree-Fock phase diagrams

In this section, we will present the unrestricted Hartree-Fock results.

As we are looking for the pinball liquid phase, with a particular attention to the metallic threefold charge order observed experimentally below the structural transition in $2H$-$AgNiO_2$ at 365K, we will try to find a realistic ratio t'/t that is representative to

the band structure of this compound. The density of states calculated by DFT-LDA of $2H$-$AgNiO_2$ compound in the normal state, above the structural transition, is reproduced from Sörgel [54] in Figure 1.5. Because this density of states is calculated in the homogeneous metallic phase, we compare it with the density of states in the noninteracting case of our model. We tune the ratio t'/t for the tight binding model to reproduce the main qualitative features of this density of states. Close to the Fermi energy, i.e. in the range [-1,1]eV which is the part that actually contributes to the conduction properties, this density of states has a peak close to the Fermi energy and two close peaks at higher energy. In the range $0.5 \lesssim t'/t \lesssim 0.75$ as shown on the right panel of Figure 3.1, the noninteracting density of states qualitatively reproduces the main features for $2H$-$AgNiO_2$. For $t'/t = 0.5$, the peak lower in energy is the closest to the Fermi energy, which appears to be the case in DFT-LDA calculations. So, this ratio of $t' = 0.5t$ will be our choice to describe the physics of this compound. We shall see below how robust are the properties to changes in this ratio. We want to mention here that although we can tune the system through a phase transition just by changing this ratio, the phases found in the specific case $t'/t = 0.5$ exist in a broad range of this parameter.

The phase diagram obtained in the $\left(\tilde{U}, V\right)$ plane for $t'/t = 0.5$ from unrestricted Hartree-Fock is reported in Figure 3.5. To explore all the possible regimes of the model, we also display the phase diagram in the (t', V) plane at a fixed value of $\tilde{U} = 1$ in Figure 3.6.

Such a moderate $\tilde{U}$, which is an effective parameter related to the microscopic interaction in the e_g-electron via the equality $U = \tilde{U} + 3J_H$ ($\tilde{U} = U_3$ in Equation 2.12 in Section 2.2), actually stands for a local Hubbard repulsion U which is considerably larger than this value. For a choice of the Hund coupling $J_H = 0.25U$, for example, the value $\tilde{U} = 1$ corresponds to $U = 4$, a value appropriate to moderately correlated materials [119]. As we show below, a rich variety of phases is found and can be classified into charge ordered (at large V) and charge homogeneous (at low V).

The right panel of Figure 3.5 conveniently reports the evolution of the local charge densities as a function of V along the vertical line shown in the phase diagram corresponding to $\tilde{U} = 1$. An analogous scan is presented on the right panel in Figure 3.6 for the t' dependence at fixed $V = 1.1$.

The different phases have been identified using order parameters introduced in the Appendix C.1 which is summarized in a truth table (Table 3.2) where nonzero order parameters have check mark a ✓ or a question mark ? in case of undefined order for incommensurate phases.

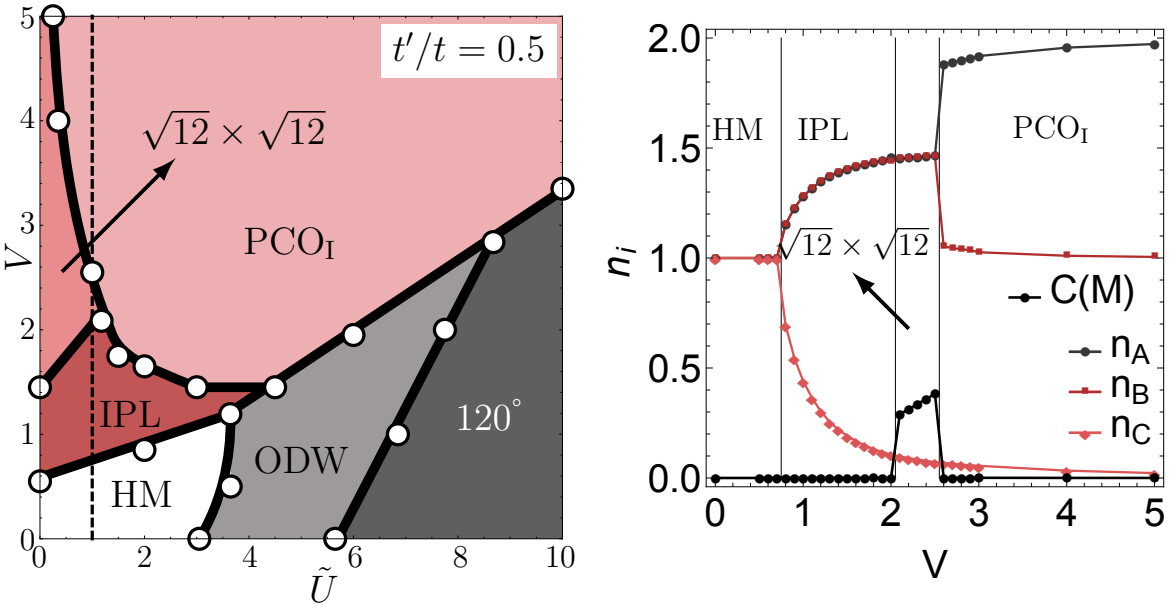

Fig. 3.5 (left) Phase diagram at zero-temperature for the multiorbital extended Hubbard model in the unrestricted Hartree-Fock approximation at fixed $t'/t = 0.5$ in the $\left(\tilde{U}, V\right)$ plane. The white disks with black edges correspond to the transition found in unrestricted Hartree-Fock. Notice that we did not display all dots corresponding to the scans performed to determined the transitions. The black lines are bezier curves using the disks as control points, except the transition lines on the left phase diagram between the charge-homogeneous and charge-ordered phases which are the predicted transition from the effective model (see Section 3.3). (right) Evolution of the three sublattice densities n_A, n_B, n_C and charge correlations $C\,(M)$ along the constant $\tilde{U}$ line shown in the left panel [the scale of $C\,(M)$ has been multiplied by 10]. For the $\sqrt{12} \times \sqrt{12}$ phase, n_A, n_B, n_C are defined as the averages over the four nonequivalent sublattices in the new unit cell. The phases denoted by HM and IPL are metallic, and all the other phases are insulating. IPL is charge ordered, PCO$_\mathrm{I}$ and $\sqrt{12} \times \sqrt{12}$ are charge and orbitally ordered, and ODW and 120° are orbitally ordered. Both phase diagrams are reproduced from [34].

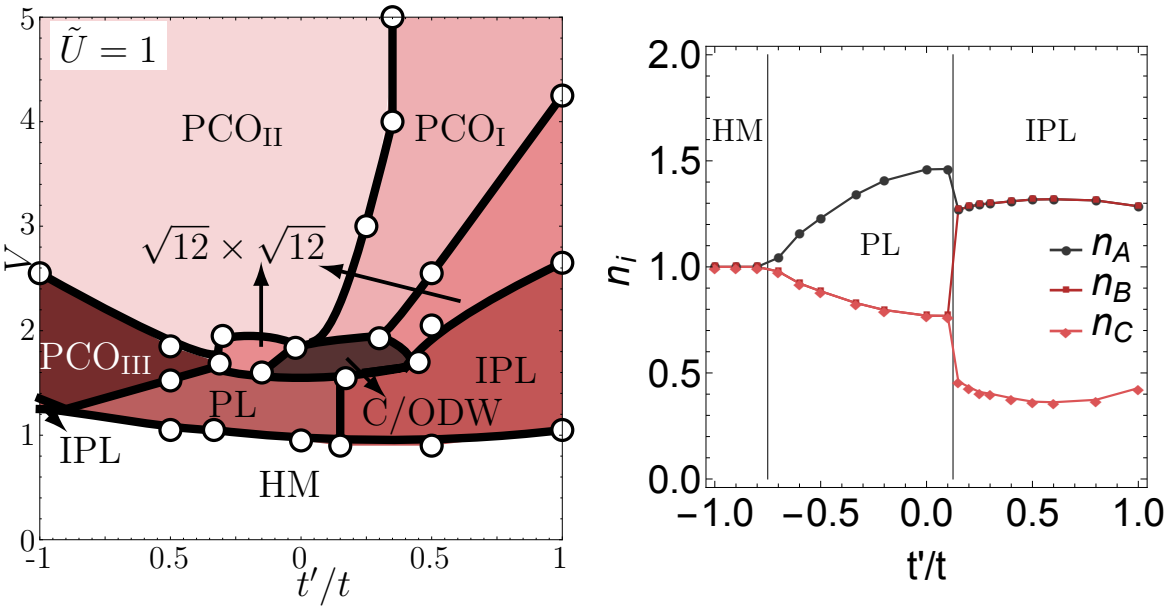

Fig. 3.6 (left) Phase diagam at zero-temperature for the multiorbital extended Hubbard model in the unrestricted Hartree-Fock approximation at fixed $\tilde{U} = 1$ in the (t', V) plane. The white disks with black edges correspond to the transition found in unrestricted Hartree-Fock. Notice that we did not display all dots corresponding to the scans performed to determined the transitions. The black lines are bezier curves using the disks as control points. (right) Evolution of the three sublattice densities n_A, n_B, n_C as a function of t'/t for fixed $\tilde{U} = 1$ and $V = 1.1$. The phases denoted by HM, PL, IPL and PCO$_{\text{III}}$ are metallic, and all the other phases are insulating. PL, IPL and PCO$_{\text{III}}$ are charge ordered, PCO$_{\text{I}}$, PCO$_{\text{II}}$, $\sqrt{12} \times \sqrt{12}$ and C/ODOW are charge and orbitally ordered. Both phase diagrams are reproduced from [34].

Table 3.2 Truth table for the different phases found in unrestricted Hartree-Fock as input and order parameters as output. Check marks ✓means the order parameter is nonzero. A question mark ? is put when the order parameter is not defined.

	$C\,(K)$	$C\,(M)$	$T\,(K)$	$\langle\tau^z\rangle$	$n_A - n_B$	$n_B - n_C$	$\sum_{i=1}^{N_s} \lvert n_{i\uparrow} - n_{i\downarrow}\rvert$
HM	0	0	0	0	0	0	0
ODW	0	?	?	0	0	0	✓
120°	0	0	✓	0	0	0	✓
IPL	✓	0	0	0	0	✓	0
PL	✓	0	0	0	✓	0	0
PCO$_{\text{I}}$	✓	0	0	0	✓	✓	✓
PCO$_{\text{II}}$	✓	0	0	✓	✓	✓	✓
PCO$_{\text{III}}$	✓	0	0	0	✓	✓	0
$\sqrt{12} \times \sqrt{12}$	✓	✓	✓	0	0	✓	✓
C/ODW	?	?	?	0	?	?	✓

For all phases we present real space snapshots where the radius of disks is proportional to the charge density on the site $(n_{i\uparrow} + n_{i\downarrow})$ and the light and dark filling corresponds to the partial orbital densities $(n_{i\uparrow}/n_{i\downarrow})$.

We also display snapshots of the orbital order, if one, using Equations C.1. Their vectorial representations are found to belong to the same plane as any triple product is null. This plane is arbitrary and rotated to coincide with the plane of the lattice to make convenient snapshots.

The total spectral function[5] $A(k,\omega)$ is computed whenever the considered phase exhibits a commensurate charge order. The path $\Gamma MK\Gamma$ displayed beside the snapshots for the original Brillouin zone correspond to a path $\Gamma' K' M' \Gamma' M' \Gamma'$ in the reduced Brillouin zone of the three sublattice structure corresponding to threefold charge orders. The Fermi surface of conducting phases is also displayed. It is interesting to notice that the folding into the reduced Brillouin zone makes the former K-points correspond to the new Γ' points. On the spectral function figures, dashed lines are the noninteracting solutions.

The two straight lines that separate charge-homogeneous to charge-ordered phases in Figure 3.5 qualitatively match the highlighted straight lines in phase diagrams of Hartree-Fock (right panel of Figure 2.3), slave spins mean-field (Figure 2.4) and Hartree-Fock with slightly different hopping integrals (Figure 2.5). The latter is remarkably consistent with our results; indeed, one can make the following correspondence: PM $\rightarrow$ HM, IM and C $\rightarrow$ ODW, A to 120°, D $\rightarrow$ IPL and B $\rightarrow$ $\mathrm{PCO_I}$. It can be explained by similar band structures (left panel in Figure 2.5 to be compared for example with dashed lines in Figure 3.7). The F phase, which corresponds to $\mathrm{PCO_{III}}$ is found instead of the $\sqrt{12} \times \sqrt{12}$ droplet phase because of their constraint (nine sites per unit cell) and the E phase that we did not find can be attributed to the difference between the noninteracting band structures.

3.4.3 Charge-ordered phases

Inverse pinball liquid

The inverse pinball liquid order, metallic threefold charge order displayed in Figure 3.7, develops in the whole region $t'/t > 0.1$ upon increasing the intersite repulsion V from the homogeneous metal phase for sufficiently low values of $\tilde{U}$ (Figs. 3.5).

The charge density separates into charge-rich sites forming a honeycomb lattice (*balls*) and charge-poor sites (*pins*) located on the remaining triangular sublattice. The

[5] We summed the contribution of the orbitals $A(k,\omega) = A_{\uparrow}(k,\omega) + A_{\downarrow}(k,\omega)$.

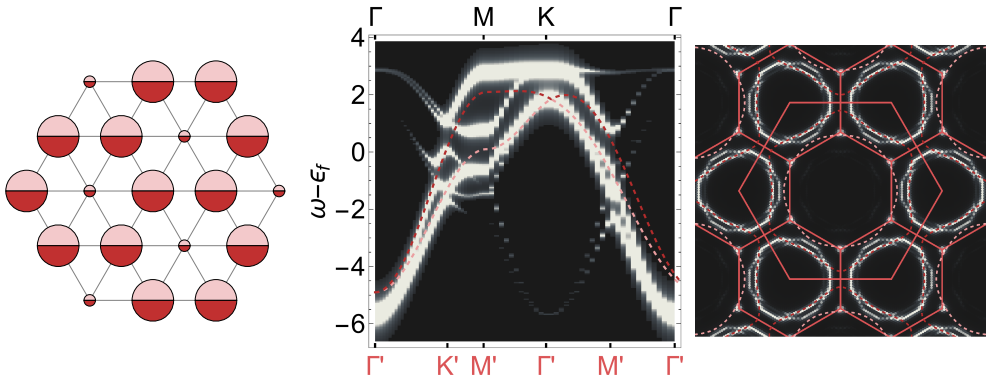

Fig. 3.7 (left) Typical charge- and orbital-density snapshot for inverse pinball liquid ($V = 0.9, \tilde{U} = 1, t' = 0.5$). The radius of the disks is proportional to the charge density on the sites, and the light and dark fillings correspond to the partial orbital densities. (middle) Spectral function and (right) Fermi surface obtained from Equation (C.5) with a Lorentzian broadening $\eta = 0.02$ on 72×72 site lattices. The solid lines in the Fermi surface plots show the original and reduced Brillouin zone, whose symmetry points are labeled in Figure A.2. The dashed lines are the Fermi surfaces and band structures in the noninteracting limit. These figures are reproduced from [34].

charge disproportionation δ in Equation 3.2 and Equation 3.3 progressively increases with V towards the maximum allowed value $\delta = 1/2$ corresponding to a fully depleted charge-poor sublattice ($n_C = 0$ and, correspondingly, $n_A = n_B = 3/2$). There is no orbital polarization in either the charge-rich or charge-poor sublattices.

The inverse pinball liquid is metallic due to the presence of itinerant carriers (balls) on the charge-rich honeycomb network as we have seen with simple considerations in Section 3.3. The right panel in Figure 3.7 illustrates the Fermi surface (FS) obtained in this phase ($V = 0.9$, $\tilde{U} = 1$, $t' = 0.5$), which clearly shows the existence of holelike carriers around the K points of the original Brillouin zone (large hexagon), resulting from the folding of one of the noninteracting bands (shown as dashed lines). Small pockets can also be seen around the corners of the reduced Brillouin zone (small hexagons). These are remnants of the second band of the noninteracting system, which at this value of t' crosses the reduced Brillouin zone very close to its corners (denoted as K' points) and therefore folds into closed pockets of trigonal shape. The origin of the large hole Fermi surface and the small trigonal pockets can also be clearly seen by comparing the spectral function $A(k, \omega)$ illustrated in middle panel of Figure 3.7 with the dispersion of the two noninteracting bands (dashed lines).

We can compare this band structure with the Hartree-Fock results in the model for an adsorbate layer presented in Figure 2.6. In our calculations, one can see splitting of the bands due to the anisotropy of the hopping integrals, we must focus on the general

trend to make the comparison. Along the path $\Gamma' K' M' \Gamma' M' \Gamma'$ [6], a lower band increases along $\Gamma' K'$, remains almost flat on along $K' M'$, decreases along $M' \Gamma'$, increases along $\Gamma' M'$ and finally decreases along the remaining $M' \Gamma'$. The two upper bands have opposite behavior on $\Gamma' K'$ until they cross on K'. The middle band follows the lowest band for the rest of the represented path (almost indiscernible in our case), whereas the upper band has an almost opposite behavior than the two lower ones. The most notable quantitative difference, i.e. the gap between the two lower bands in Figure 2.6, comes from the higher values of the effective Coulomb energies $\tilde{U}$ and V, in an area where the pinball liquid is not stabilized for this ratio of t'/t. Other differences come from the form of the hopping integrales. Nevertheless, the good agreement between the two band structures shows that the electronic phase found in the adsorbate work in Ref. [95] is actually an inverse pinball liquid, although pinball liquid states had not been identified at the time of that work.

Inverse pinball liquid exhibits characteristics of the phase in $2H$-$AgNiO_2$, metallic and threefold charge order, but the real-space snapshot corresponds to the dual of this phase where the charge rich and charge poor sites are swapped which looks like the original pinball liquid. The reason can be because our initial guess of t'/t is based on a fit of the noninteracting band structure. However, we can tune this ratio in order to reach the pinball liquid as observed in the experiment.

Pinball liquid

When $t'/t < 0.1$, the inverse pinball liquid $\frac{3}{2}$-$\frac{3}{2}$-0 charge pattern ($\delta = 1/2$) shown in Figure 3.7 is replaced by the pinball liquid, with a 2-$\frac{1}{2}$-$\frac{1}{2}$ pattern ($\delta = -1/2$) as illustrated in Figure 3.8. This phase is dual to the inverse pinball liquid in the sense that the roles of the charge-rich and charge-poor sublattices are interchanged. We identify this phase with the original pinball liquid of Hotta and coworkers [31] (see Section 1.2.3) because, from the point of view of the electronic densities ($n_A = 2$, $n_B = n_C = 1/2$), it can be viewed as two realizations of the pinball liquid phase found at quarter filling, one per each orbital character (the pinball liquid at quarter filling has $n_A = 1$, $n_B = n_C = 1/4$). Because of orbital-orbital interactions, however, the two realizations are not independent, and the present pinball liquid can occur for only small or moderate values of $\tilde{U} \lesssim 5$. This can be contrasted with the quarter-filled case, where a strong Hubbard term is required to stabilize the pinball liquid [69, 33, 38] as shown in Figure 1.10.

[6] The $'$ in our notation are $_{3\times3}$ in Figure2.6

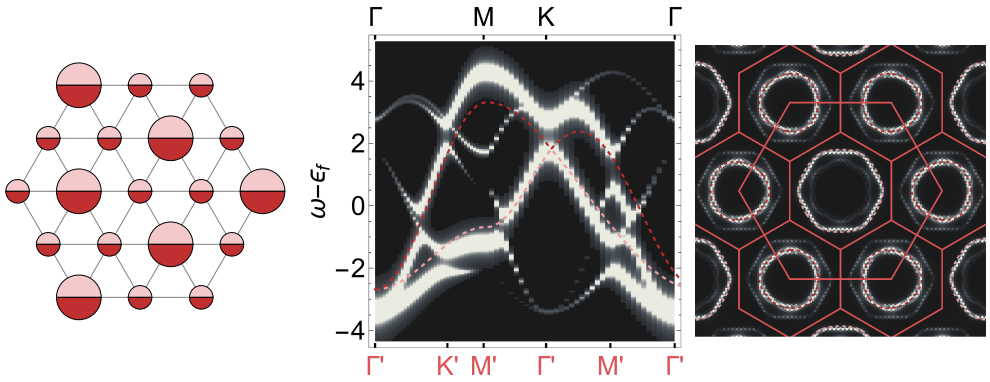

Fig. 3.8 (left) Typical charge- and orbital-density snapshot for pinball liquid ($V = 1.1, \tilde{U} = 1, t' = 0$). The radius of the disks is proportional to the charge density on the sites, and the light and dark fillings correspond to the partial orbital densities. (middle) Spectral function and (right) Fermi surface obtained from Equation (C.5) with a Lorentzian broadening $\eta = 0.02$ on 72×72 site lattices. The solid lines in the Fermi surface plots show the original and reduced Brillouin zone, whose symmetry points are labeled in Figure A.2. The dashed lines are the Fermi surfaces and band structures in the noninteracting limit. These figures are reproduced from [34].

The phase diagram in Figure 3.6 shows that the selection between the pinball liquid order and its dual inverse pinball liquid is entirely governed by kinetic effects, as it is independent of Coulomb interactions and transition is controlled through t'/t. This can be understood by observing that the electrostatic energies of the pinball liquid and inverse pinball liquid are formally equal and do not depend on the sign of the charge disproportionation δ (see Section 3.3). Notice that the stabilization of the inverse pinball liquid is also influenced by the number available states. If the spin degree of freedom is included for the same number of electrons, see the work of Ralko, Merino and Fratini in Ref. [35], then the number of available states is doubled and the inverse pinball liquid phase is transformed into the pinball liquid phase on this quarter-filled system.

Similar to the inverse pinball liquid, metallic behavior arises in the pinball liquid from the motion of electrons living on the honeycomb network. At this value of t', the noninteracting Fermi surface (dashed line) is composed of a large electronlike surface around the Γ point and smaller holelike pockets around the K points. Contrary to the inverse pinball liquid shown previously, however, the overall shape of the Fermi surface is only weakly affected by charge ordering of the PL type because the original Fermi pockets do not cross the boundaries of the reduced Brillouin zone (Fig. 3.8).

Pinball charge order

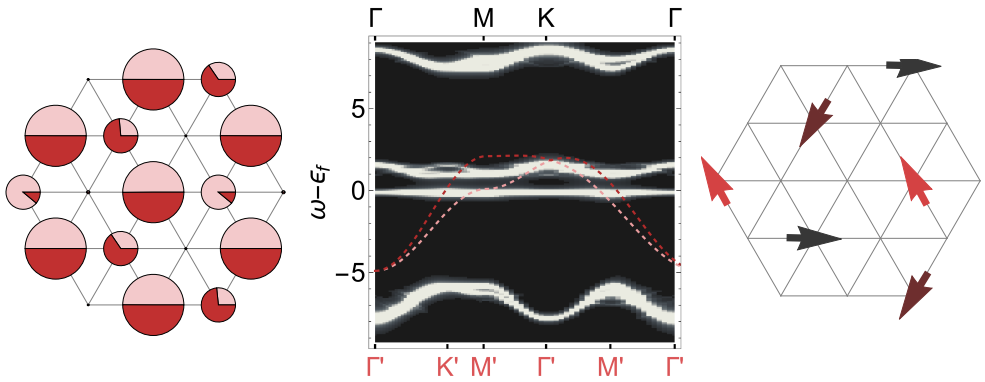

Fig. 3.9 (left) Typical charge- and orbital-density snapshot for $\mathrm{PCO_I}$ ($t'/t = 0.5$, $\tilde{U} = 1$, $V = 2.6$). The radius of the disks is proportional to the charge density on the sites, and the light and dark fillings correspond to the partial orbital densities. (right) Spectral function obtained from Equation (C.5) with a Lorentzian broadening $\eta = 0.02$ on 72×72 site lattices. The dashed lines are band structures in the noninteracting limit. These figures are reproduced from [34]. (right) Vectorial representation of orbital order. Orbital vectors on singly occupied sites exhibit the 120° order with the same norm than in the 120° phase (see Figure 3.16).

At large V, the system undergoes further charge ordering, stabilizing a 2-1-0 charge pattern termed pinball charge order (Fig. 3.9). Simple electrostatic arguments predict that the pinball charge order is stabilized for $V > \tilde{U}/3$, as discussed in Section 3.3 above, which nicely agrees with the numerical results at large $\tilde{U}$ and V (see left panel of Fig. 3.5).

The threefold disproportionation splits the electronic dispersion into three separate bands per orbital state. Counting the occupied states leaves us with a central half-filled band, which should lead, in principle, to a metallic behavior. We find instead that the pinball charge order phase found in the whole region $t'/t \gtrsim 0.1$, denoted $\mathrm{PCO_I}$ in Figures 3.5 and Figure 3.6, is insulating (see the spectral function in Fig. 3.9). This is ascribed to the presence of a spiral 120° orbital order on the singly occupied B sites, identical to the order of the local electronic densities of the 120° phase (see Section 3.4.4), caused by the local interaction $\tilde{U}$, as seen in orbital order of the right snapshot in Figure 3.9. The order of the Hartree terms within 120° changes with the ratio t'/t following the threefold orbital order of the 120° phase.

Other orbital orderings on the B sublattice are possible within the present 2-1-0 charge arrangement upon varying t'/t (Fig. 3.6). These are $\mathrm{PCO_{II}}$ for $t'/t \lesssim 0.1$ and

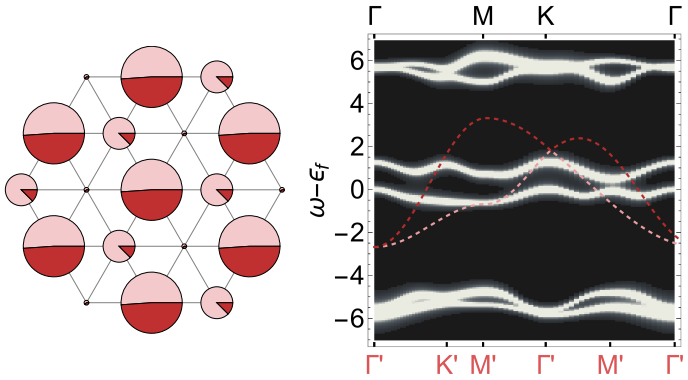

Fig. 3.10 (left) Typical charge- and orbital-density snapshot for PCO_{II} ($t'/t = 0$, $\tilde{U} = 1$, $V = 2$). The radius of the disks is proportional to the charge density on the sites, and the light and dark fillings correspond to the partial orbital densities. (right) Spectral function obtained from Equation (C.5) with a Lorentzian broadening $\eta = 0.02$ on 72×72 site lattices. The dashed lines are band structures in the noninteracting limit. These figures are reproduced from [34].

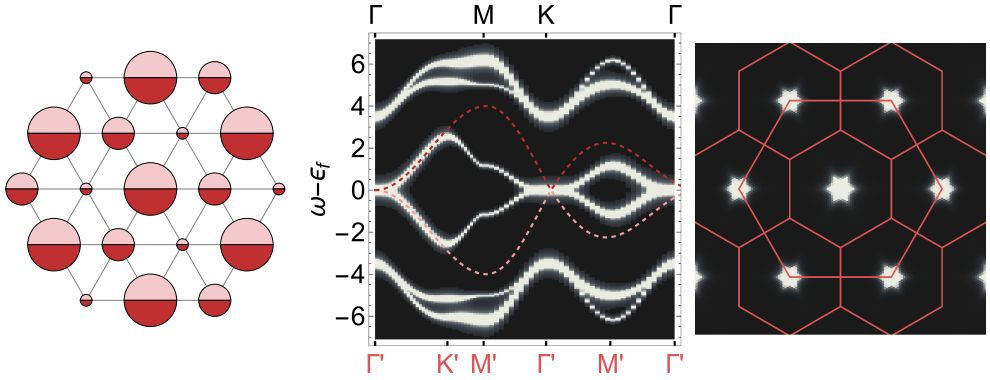

Fig. 3.11 (left) Typical charge- and orbital-density snapshot for PCO_{III} ($V = 2, \tilde{U} = 1, t' = -1$). The radius of the disks is proportional to the charge density on the sites, and the light and dark fillings correspond to the partial orbital densities. (middle) Spectral function and (right) Fermi surface obtained from Equation (C.5) with a Lorentzian broadening $\eta = 0.02$ on 72×72 site lattices. The solid lines in the Fermi surface plots show the original and reduced Brillouin zone, whose symmetry points are labeled in Figure A.2. The dashed lines are the Fermi surfaces and band structures in the noninteracting limit. These figures are reproduced from [34].

large V (uniformly polarized B sites, Fig. 3.10) and $\mathrm{PCO_{III}}$ for $t'/t \lesssim 0.1$ and low V (unpolarized B sites, Fig. 3.11).

$\mathrm{PCO_{II}}$ is also an insulator because the ferro-orbital polarization is sufficient to split the narrow half-filled band at the Fermi energy into two separate components (Fig. 3.10). Note that this is the only phase in the whole phase diagram which supports a nonzero $\langle \tau^z \rangle$.

$\mathrm{PCO_{III}}$ instead has a metallic character. It is the phase originally found in some mean-field studies at low V, including the region where we find that the $\sqrt{12} \times \sqrt{12}$ droplet phase is stabilized instead (see the paragraph below), that we presented in Section 2.4.2 such has the F asymmetric CDW in Figure 2.5. In the limit $t' = -t$, shown in Figure 3.11, it is a semimetal with bands touching at the Γ and K points with an electron hole symmetry preserved from the noninteracting limit.

The transition from inverse pinball liquid to the $\mathrm{PCO_I}$ upon increasing V can be seen as a charge order transition within the metallic honeycomb lattice. Although this argument, seen in Section 3.3, does not explain the exact locus of the transition reported in Figure 3.5, the shape of this transition is almost a straight line with the predicted slope $-\frac{\tilde{U}}{6}$.

We conclude the description of this phase by giving an intuitive understanding of the band structures. We can identify three sets of bands in Figure 3.9, Figure 3.10 and Figure 3.11. These sets are independent in the sense that a gap $\propto V$ exists between them and each site of the three sublattices can be associated directly to n_A for the lower bands, n_B for the middle bands, around the Fermi energy, and n_C for the upper bands. Focusing on the middle bands means looking at the singly occupied site n_B and then metallic or insulating properties will be driven by their orbital order. The shape of middle bands in the metallic $\mathrm{PCO_{III}}$ is similar to the noninteracting case and therefore form a homogeneous metal on singly occupied sites n_B, whereas $\mathrm{PCO_I}$ and $\mathrm{PCO_{II}}$, orbitally ordered, are insulators with a gap $\propto \tilde{U}$.

$\sqrt{12} \times \sqrt{12}$ droplet phase

In addition to the broken symmetry phases already reported in the literature, our unrestricted Hartree-Fock study has revealed, for $t'/t > 0.1$, an additional phase in the small-$\tilde{U}$ regime, located between the two charge-ordered phases found at small and large V. This phase has a large periodicity with 12 sites in the unit cell (see Figure 3.12).

The $\sqrt{12} \times \sqrt{12}$ droplet phase is characterized by the coexistence of peaks in the charge-charge correlation function at the K points (characterizing threefold order) plus

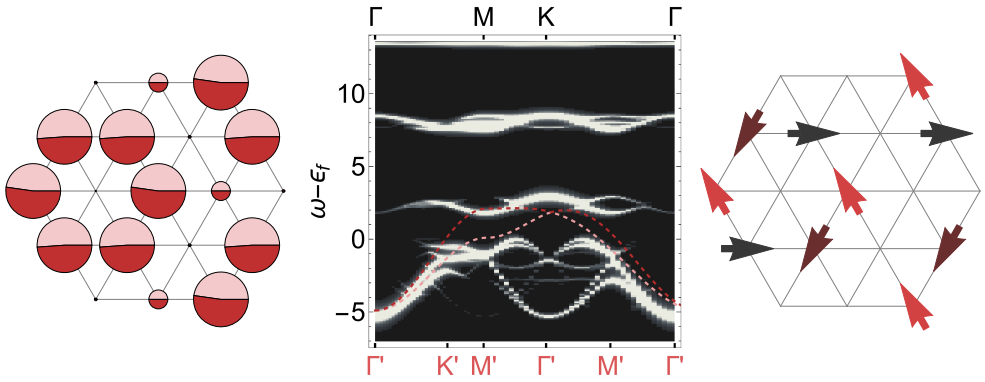

Fig. 3.12 (left) Typical charge- and orbital-density snapshot for $\sqrt{12} \times \sqrt{12}$ droplet phase ($t'/t = 0.5$, $\tilde{U} = 1$, $V = 2.5$). The radius of the disks is proportional to the charge density on the sites, and the light and dark fillings correspond to the partial orbital densities. (middle) Spectral function obtained from Equation (C.5) with a Lorentzian broadening $\eta = 0.02$ on 72×72 site lattices. The dashed lines are band structures in the noninteracting limit. These figures are reproduced from [34]. (right) Vectorial representation of orbital order. We displayed vectors only on filled hexagons because the norm on the other sites is at least six times smaller. To reveal the order, the scale of vectors is ten times bigger than in Figure 3.9 and Figure 3.16.

all the M (whose combination describes a phase with fourfold symmetry [92]) and $K/2$ points (see Table 3.2). The latter are absent in the phases with pure threefold symmetry. The evolution of M-point charge-charge correlation is shown on the right panel in Figure 3.5. This charge-charge correlation is proportional to the $K/2$-point correlation.

The real-space snapshot in Figure 3.12 shows that the charges form disconnected hexagonal droplets, composed of essentially doubly occupied sites. These are surrounded by sites which are either empty or almost empty. The latter are responsible of an additional orbital ordering, nonzero orbital correlations at points M and $K/2$, by taking uniformly charges from hexagons. On right panel of Figure 3.12, we displayed the vectorial representation in real space on the lattice for the hexagons, which is already small [norm about ten times smaller than $\mathrm{PCO_I}$ (Fig. 3.9) and 120° phase (Fig. 3.16)], but we did not display the even smaller order on the almost empty sites because their norm is almost an order of magnitude smaller than on the hexagons.

The $\sqrt{12} \times \sqrt{12}$ droplet phase is stabilized with respect to the PCO phase by purely kinetic effects. It can be shown straightforwardly that the potential energies of the droplet and PCO phases coincide when $\tilde{U} = 0$ (the cost due to V being exactly equal), while the droplet phase is rapidly destabilized by $\tilde{U}$ due to the larger double occupation (see Section 3.3).

Unlike PCO_I and PCO_{II}, this phase has a strongly insulating character due to the charge order, opening of a gap $\propto V$ at the Fermi energy (Fig. 3.12).

We note that the emergence of a charge pattern with a high-order periodicity such as the one found here is not at all trivial given that the electron-electron repulsion is restricted to only nearest-neighbor sites and is not present in a purely Hartree approach; the additional Fock approximation renormalizes the kinetic energy needed to stabilize this phase.

The region in parameter space where the $\sqrt{12} \times \sqrt{12}$ droplet phase is stabilized actually includes the limit $t' = t$ where Equation 2.14 becomes equivalent to the spinful extended Hubbard model, but it was overlooked in previous studies [95, 92, 93, 70, 94, 120]. Interestingly, the present 12-site period is very close to the 13-site star of David modulation found in the triangular dichalcogenide compound $1T$-TaS_2 [20] presented in Chapter 1. The hexagonal droplets in Figure 3.12 are also similar to those recently predicted theoretically in the kagome lattice at $n = 1/3$ filling [115, 121], but in that case they are a natural consequence of the larger unit cell of the underlying lattice (see also Refs. [98, 122]).

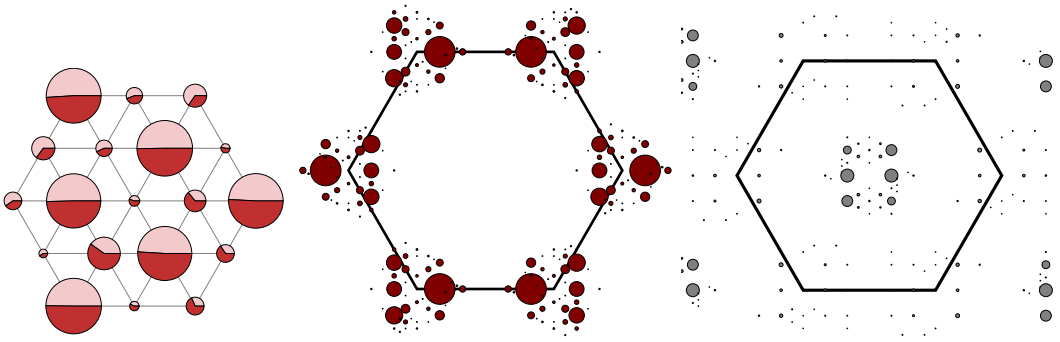

Fig. 3.13 Charge (left) and orbital (right) correlation on 36×36 lattice for the C/ODW phase ($V = 1.5, \tilde{U} = 1, t' = 0$). The black hexagon is the first Brillouin zone. The radius of the disks corresponds to the weight of the corresponding $\vec{k}$-point in arbitrary unit. In the charge correlation, we did not display the large disks on points Γ and K.

Finally, we mention that the $\sqrt{12} \times \sqrt{12}$ phase obtained in the interval $-1/3 < t'/t \lesssim -0.1$ (see left panel of Fig. 3.6) has the doubly occupied hexagons replaced by empty sites and vice versa and can therefore be considered as the dual to the droplet phase described above, just as the inverse pinball liquid is the dual to the pinball liquid. The two are separated by a phase with coexisting incommensurate charge and orbital order, denoted C/ODW (see snapshots Figure 3.13 and Figure 3.14). Because our real space approach is not optimized for the description of incommensurate order, the latter is identified as incommensurate by the presence of clouds of peaks in both the charge

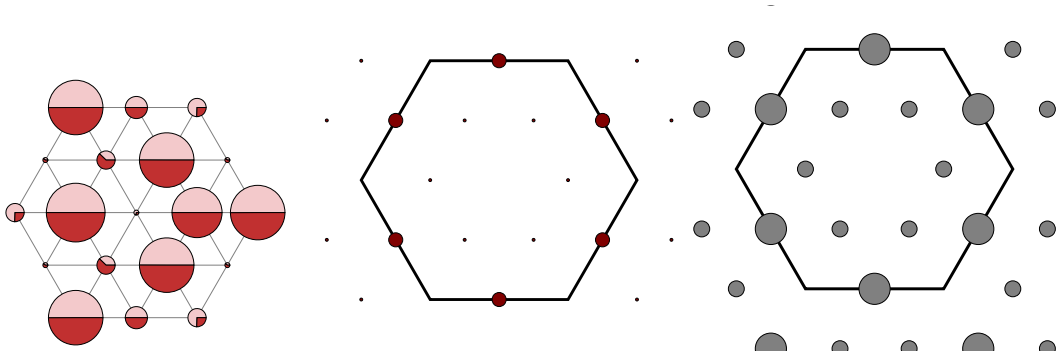

Fig. 3.14 Charge (left) and orbital (right) correlation on 36×36 lattice for the C/ODW phase ($V = 1.8, \tilde{U} = 1, t' = 0$). The black hexagon is the first Brillouin zone. The radius of the disks corresponds to the weight of the corresponding $\vec{k}$-point in arbitrary unit. They are the same than Figure 3.13 for the orbital correlation and ten times smaller for the charge correlation. In the charge correlation, we did not display the large disks on points Γ and K.

and orbital correlation as displayed in Figure 3.13 or coexistence of different orders, shown in Figure 3.14, in analogy with some areas in the ODW region of the phase diagram (see below). From one run to another, unrestricted Hartree-Fock gives similar clouds of correlations peaks.

3.4.4 Charge-homogeneous phases

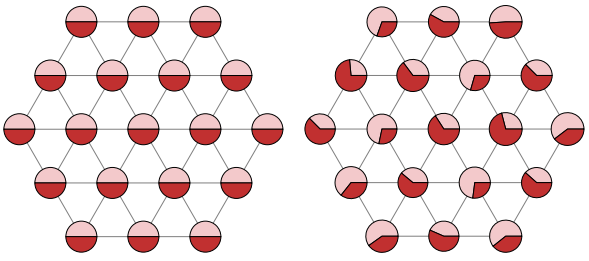

Fig. 3.15 Typical charge- and orbital-density snapshots in the different phases realized in the model: (left) HM and (right) ODW. The radius of the disks is proportional to the charge density on the sites, and the light and dark fillings correspond to the partial orbital densities.

Several phase transitions are also found within the charge homogeneous region at low V. The system evolves upon increasing the effective local interaction from a paraorbital metal at small $\tilde{U}$, the equivalent of the paramagnetic metal by making the correspondance between spins and orbitals, denoted as homogeneous metal (HM), to a

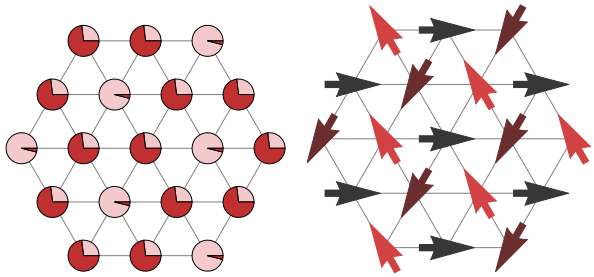

Fig. 3.16 (left) Typical charge- and orbital-density snapshot of the 120° phase. The radius of the disks is proportional to the charge density on the sites, and the light and dark fillings correspond to the partial orbital densities. (right) Vectorial representation of the orbital order. Notice that although two sites have the same orbital filling (Hartree parameters), their vectorial representation that takes into account the Fock parameters is different (see Appendix C.1).

spiral 120° orbitally ordered insulating phase at large $\tilde{U}$. Snapshots of this two phases are displayed in left panels of Figure 3.15 and Figure 3.16.

Homogeneous metal

The homogeneous metal corresponds to the solution of the tight-binding Hamiltonian and presents no order, neither for the charges nor the orbitals with a null charge gap, Equation C.4, consistent with the prediction of a metallic state. Notice that the kinetic energy of this phase remains constant upon varying the interactions and the total energy of this phase is directly the sum of its kinetic energy and potential energy which agrees with our arguments in Section 3.3 and is confirmed by the agreement between the static model and unrestricted Hartree-Fock for the transition line to the inverse pinball liquid.

120° phase

For strong local Coulomb interaction $\tilde{U}$, a Mott state is expected with one electron per site exactly on only one orbital which, at the present mean-field level, is represented by an orbital broken symmetry. For example, if one considers only Hartree approximation, z component of orbitals, stripe order is stabilized, but taking into account the Fock approximation allows orbital to form a threefold order by adding x and y orbital component. For $t' = t$, the local electronic densities are arranged as follows orbital $\uparrow$ on site A ($n_{A\uparrow} = 1, n_{A\downarrow} = 0$), orbital $\downarrow$ on site B ($n_{B\uparrow} = 0, n_{B\downarrow} = 1$) and equally filled on site C ($n_{C\uparrow} = 1/2, n_{C\downarrow} = 1/2$) of the three sublattice. This orbital order is surprising because of the strong cost in $\tilde{U}$, however this cost is exactly counterbalance

by the *orbital flip*, a local current that allows the electron to change orbital on the same site. It is a good example where corrections to the electrostatic limit are introduced by the Fock term. Due to the degeneracy of the model at the isotropic point $t' = t$, the solution on the Fock term changed at each run of the unrestricted Hartree-Fock algorithm. Nevertheless, the correlation is always, and only, on the K-point. On the three sublattice corresponding to this order, the sum of orbital vectors is null, i.e. $\langle \vec{\tau}_A + \vec{\tau}_B + \vec{\tau}_C \rangle = 0$[7], moreover, $|\vec{\tau}_i| = |\vec{\tau}_j| \, \forall i, j$ which implied that there exists a plane containing all the orbital vectors. The orbital moments of the 120° phase are arranged in planes perpendicular to the lattice as soon as $t' \neq t$.

Orbital density wave

In the intermediate local Coulomb interaction area, the system goes through an intermediate region with more complex orderings, denoted as ODW in the left phase diagram of Figure 3.5. A precise study of this intermediate region is beyond the scope of this thesis because the unrestricted Hartree-Fock method in real space is not suited to address incommensurate orders (see Section 3.4.1). No symmetrization can be used and each run must be launched for a large system and last a large number of iterations (typically more than 10^5), which involves a non-reasonable computation time to check the accuracy and detect spurious solutions. However, we would like to stress the following points: (i) Within our real-space unrestricted approach, we have recovered the two intermediate mean-field phases of the spinful Hubbard model [84, 85], namely an incommensurate orbital (spin) ordered phase whose wave vector evolves with $\tilde{U}$ and a zigzag stripe compatible with the points $k = (\pm\pi, 0)$. (ii) While previous studies have looked for solutions breaking the symmetry at a single wave vector, we find solutions compatible with two or more coexisting k vectors, typically on K- and M-points close to the transition to the 120° phase, possibly a mean-field indication of a tendency to a structureless orbital liquid state. (iii) Away from the case of the isotropic Hubbard model, i.e., as soon as $t' \neq t$, the zigzag stripe phase seems to disappear, and only the incommensurate regions with coexisting order survive. (iv) At $t' = 0.5$, the critical parameter $\tilde{U}_c$ is decreased by 25% with respect to the isotropic case $t' = t$, in agreement with the corresponding reduction of the bandwidth. (v) The orbital density wave phases exhibit a finite charge gap meaning they are insulating in contradiction with previous studies [84–86, 95].

[7] Notice that this is not possible with only Hartree approximation

3.4.5 Discussion on accuracy of electrostatic arguments

Unrestricted Hartree-Fock presented here and classical approach of Section 3.3 are in perfect agreement for the metal to inverse pinball liquid transition as well as for the Mott state to the pinball charge order. It is also matching the exact diagonalization results in the asymptotic limit (see next Section). These predicted lines are drawn on the unrestricted Hartree-Fock phase diagram in Figure 3.5.

Two surprising effects arise about the transition between the 120° phase and $\mathrm{PCO_I}$ with the unrestricted Hartree-Fock method. First, this prediction works even when the half-filled sites are not completely polarized, in other words the ideal case of electrostatic limit is not reached yet. The unrestricted Hartree-Fock method lowers the on-site Coulomb cost with the Fock terms. Second, in the completely frustrated case, i.e. when $t = t' = 1$, the specific patterns of these two phases remain in the strong interaction limit with the sites not polarized in 120° order. As mentioned before, the Fock term enforces a solution which lowers the energy with local current, the *orbital flip*, in order to compensate exactly the static cost.

Nevertheless, the qualitative description of Section 3.3 suffers of few limitations. (i) It does not capture the correlation between the pins and the balls which increases the screening of the band structure of the honeycomb lattice. This is the reason why we find the inverse pinball liquid in a larger area in the classical model and thus why we do not have a quantitative agreement for the transition to the $\sqrt{12} \times \sqrt{12}$ droplet charge order nor the pinball charge order which are predicted for larger V. (ii) The stabilization of the $\sqrt{12} \times \sqrt{12}$ droplet charge order away from the predicted $V = 0$ is an evidence of the purely kinetic origin of this phase. (iii) The transition from the metal to the Mott insulator found in unrestricted Hartree-Fock is not exactly vertical, as it is with static arguments, because of the coupling between the short range Coulomb interaction and the hopping integrals. (iv) We can not predict with the electrostatic model a transition to different orbital-ordered phases as they are all electrostatically equivalent nor distinguish between different charge orders, such as pinball liquid and its dual or polarized pinball charge order, stripe and $\sqrt{12} \times \sqrt{12}$ droplet charge order.

In order to confirm the unrestricted Hartree-Fock results, which does not take into account correlations by construction (decoupling of product of $n_{i\sigma}$ operators), we shall now make a comparison with another numerical approach, the exact diagonalization.

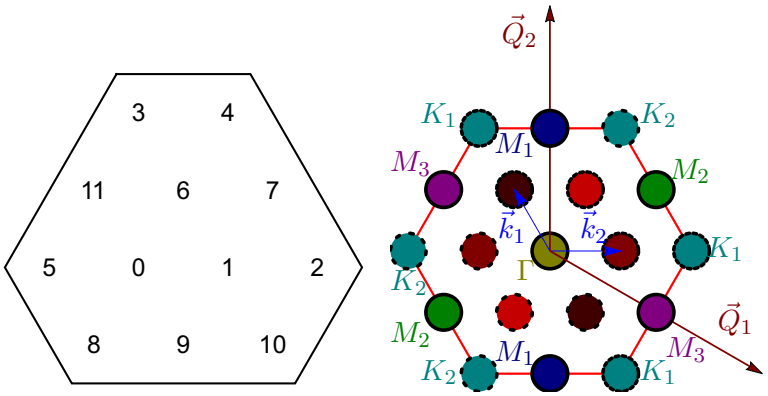

Fig. 3.17 (left) 12-site cluster used for exact diagonalization and (right) its Brillouin zone where high symmetry points are labelled. The non-labelled $\vec{k}$-points are $K/2$. Colors show points connected by C_2 point group symmetry. Only Γ and M (solid line edges) remain invariant while K and $K/2$ (dashed line edges) are connected to non equivalent points.

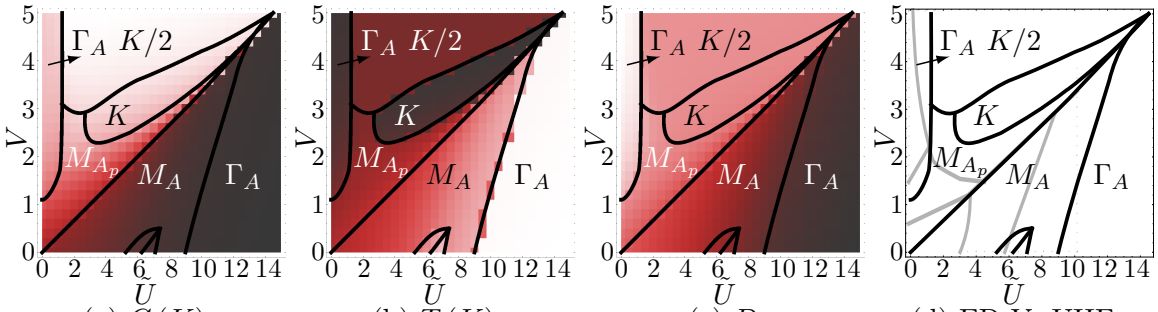

(a) $C\,(K)$ (b) $T\,(K)$ (c) D (d) ED Vs UHF

Fig. 3.18 Phase diagrams obtained from exact diagonalization on a 12-site cluster at fixed $t' = 0.5t$. Panels (a) to (c) are reproduced from [34]. (a) Charge-charge correlation $C\,(K)$. (b) Orbital-orbital correlation $T\,(K)$. (c) Expectation value of the double occupation D. (d) Comparison with UHF pahse diagram (gray lines). The color maps are in arbitrary scale, increasing from dark to bright. On each panel are shown the ground-state symmetry sectors (translation and point group) and first-order transition lines (thick lines) reflecting symmetry breaking driven either by the charges, the orbitals or both. The symmetry sectors in the small dome at low V is respectively $K/2$ and M_{A_p} as $\tilde{U}$ increases.

3.5 Comparison with Exact diagonalization

In this section, we shall briefly compare our results with exact diagonalization results. Whereas I performed exact diagonalization computations on this model, in order to focus on the problem of the next chapter, the final results presented here are obtained by Arnaud Ralko. A detailed presentation of this method will be done in the next chapter, in Section 4.4, when presenting the results I myself obtained on the effective model for the Mott regime.

To ascertain if the variety of phases found at mean-field level in phase diagram of Figure 3.5 is robust against quantum fluctuations, we have performed a systematic study of the model Equation 2.14 via Lanczos diagonalization on a 12-site cluster. Such a cluster is compatible with all the symmetries of the expected charge-ordered phases except for PCO_I, which has a nine-site unit cell due to the presence of additional 120° orbital order. It is also compatible with the orbital order found by unrestricted Hartree-Fock in the low-V region, 120° phase, but not with the $(\pm\pi, 0)$ zigzag stripes and the incommensurate stripes characteristic of intermediate $\tilde{U}$, denotes by ODW in unrestricted Hartree-Fock phase diagram.

For these calculations, we have taken the largest available cluster fulfilling all the symmetry requirements mentioned above, namely, the 12-site tilted cluster, as depicted in the left panel of Figure 3.17, with $L = 2$ in definition given in Section A.1.2.

Since the Hamiltonian does not preserve the orbital flavor, $\langle \tau^z \rangle \neq 0$ a priori, one has to consider, for a fixed number of particles, all the orbital sectors.

In addition, due to the structure of the hopping matrix, as soon as $t' \neq t$, the three directions of the lattice become inequivalent hence breaking the C_{6v} point-group symmetry. The system can thus be block-diagonalized simultaneously for $\vec{k}$-points, representation of translations, compatible with the remaining C_2 symmetries, which contain only two generators, I and R_π, the identity matrix and the rotation of an angle of π around the z axis. This is true for only points Γ and M; K and $K/2$ are not compatible with such symmetries. It is shown on the Brillouin zone Figure 3.17 where $\vec{k}$-points connected by R_π have the same color and solid edge points are invariant by this symmetry.

In a given $\vec{k}$-sector, the ground state (GS) can then be either symmetric (referred to as A) or antisymmetric (A_p) against the C_2 symmetries. This will be used in the interpretation of the exact diagonalization phase diagram. In the next chapter, especially in Section 4.4, we shall give a more exhaustive description of exact diagonalization and an introduction to the symmetry for the bosonic effective model derived from perturbation theory. The noteworthy difference is the fermionic sign.

Table 3.3 Comparison of the charge-charge correlation $C\left(\vec{k}\right)/N_s$ for the high symmetry points K and M in the different charge-ordered phases, computed analytically on the ideal patterns, via unrestricted Hartree-Fock and exact diagonalization. The values for PCO, IPL/PL, and $\sqrt{12}\times\sqrt{12}$ correspond to $t'/t = 0.5$ and $(\tilde{U}, V)$ of (6,4), (1,1.2), and (0,3), respectively.

		PCO	IPL/PL	$\sqrt{12}\times\sqrt{12}$
Analytical	K	1/3	1/4	1/4
	M	0	0	1/9
UHF	K	0.302	0.121	0.227
	M	0	0	0.065
ED	K	0.308	0.157	0.262
	M	0.006	0.055	0.063

Figure 3.18 shows the phase diagram obtained in the $\left(\tilde{U}, V\right)$ plane for $t' = 0.5t$ by combining the symmetry character of the ground state for the charge-charge [Fig. 3.18(a)] and the orbital-orbital [Fig. 3.18(b)] correlations at the corner of the Brillouin zone (K) and the average double occupation [Fig. 3.18(c)]. The transition lines for both the unrestricted Hartree-Fock calculations (gray) and exact diagonalization (black) are drawn in panel (d). Our exact diagonalization results for small clusters confirm that the very rich physical picture created by the interplay between charge and orbital degrees of freedom persists even beyond the mean-field level. A large number of domains with different symmetries are obtained, separated by first-order transitions, as displayed in three right panels of Figure 3.18; these domains can be associated with all of the different phases found in phase diagram of Figure 3.5 as explained below.

3.5.1 Charge-ordered phases

The buildup of K-point charge correlations in Figure 3.18(a), which is expected in all the charge-ordered phases described in Section 3.4.2, shows remarkable agreement with the unrestricted Hartree-Fock charge-ordering transition lines reported in the left phase diagram of Figure 3.5 and asymptotically follows the analytical prediction $V_c = \tilde{U}/3$ (see Section 3.3). We provide in Table 3.3 some representative values of $C\left(\vec{k}\right)$ at points K and M for the different charge-ordered phases, as computed numerically by both unrestricted Hartree-Fock and exact diagonalization and analytically on ideal electrostatic patterns (see more details about the electrostatic case in Section 3.3 above). As one can see, a quantitative agreement is found between the two numerical methods, which allows for direct identification of mean-field phases in exact diagonalization

results. From Figure 3.18 and Table 3.3, we associate the different charge-ordered phases as follows: $K/2$ and $K \rightarrow$ PCO, $M_{A_p} \rightarrow$ PL, and $\Gamma_A \rightarrow \sqrt{12} \times \sqrt{12}$.

First, we identify both $K/2$ and K ground states with the broad PCO region of Figure 3.5. The additional transition seen here, which is absent in unrestricted Hartree-Fock, may have origin either the exact treatment of the correlations or the size of the lattice. Indeed, the ninefold orbital order present in the PCO_I phase found in unrestricted Hartree-Fock is not compatible with the 12-site cluster used for exact diagonalizrion, so that different orderings are stabilized instead. Accordingly, this change of symmetry is not observable in $C(K)$, but it is clearly seen in $T(K)$ in Figure 3.18(b).

Second, by looking at the charge correlations in real space $\langle\psi'|n_0 n_i|\psi'\rangle$ (not shown), with $|\psi'\rangle$ the vector of the subspace having an electron on site labelled 0, it is possible to associate the M_{A_p} ground state with pinball liquid order. The latter is found here instead of the inverse pinball liquid expected from unrestricted Hartree-Fock because the considered cluster is too small to capture the subtle kinetic effects which distinguish between these two phases. This is confirmed by the fact that the pinball liquid is also selected in the unrestricted Hartree-Fock solution when a 12-site cluster is considered, as we have checked. Due to the continuous evolution of the local electronic densities as a function of the strenth of the interactions for the pinball liquid phases, for a set of $\left(\tilde{U}, V\right)$ at the center of a pinball liquid area, the correlations have a larger mismatch with the expected ideal value. As this evolution is different between exact diagonalizations and unrestricted Hartree-Fock approach, there is also a difference in the value of the correlations between the two methods. Notice that the charge-charge correlation is equal for the pinball liquid and its dual, the inverse pinball liquid.

Third, the $\sqrt{12} \times \sqrt{12}$ droplet phase found in the mean field can be associated with the Γ_A ground state at low $\tilde{U}$ in Figure 3.18. This phase has a charge signature corresponding to a mixture of the high-symmetry $\vec{k}$ vectors K, M, and $K/2$ on the charge-charge correlation, with dominant weight on the first two, which agrees with unrestricted Hartree-Fock and analytical results (see Table 3.3), involving a charge modulation on 12 sites. Also, it is in this phase that we find the strongest double occupancy [Fig. 3.18(c)], which corresponds to the doubly occupied sites on the hexagons in Figure 3.12. Our exact diagonalization results confirm the finding that the $\sqrt{12} \times \sqrt{12}$ droplet phase remains stable in the spinful extended Hubbard model ($t' = t$).

3.5.2 Orbitally ordered phases

The different phases found in unrectricted Hartree-Fock upon increasing $\tilde{U}$ at low V also have their direct analogs in exact diagonalization. We associate the spiral 120° phase obtained in unrectricted Hartree-Fock with the Γ_A phase at large $\tilde{U}$ and small V: here the double occupation is strongly suppressed, indicating a Mott insulating state with large threefold orbital correlations compatible with such an order [88, 123]. We note that the critical value for the Mott transition, $U_c \approx 9t$, is smaller than the value $U_c \approx 12t$ reported from analogous exact diagonalization calculations in the isotropic case [88], which can be understood by observing that the bandwidth is reduced by roughly 25% for the considered $t' = 0.5t$ (right panel of Fig. 3.1). We also observe a small dome in the middle of the M_A phase, which we tentatively associate with the orbital density wave orders obtained by unrestricted Hartree-Fock on larger systems as suggested by the signatures in $T(K)$. In this dome, two distinct symmetry sectors corresponding to two different phases are encountered as $\tilde{U}$ increases, $K/2$ and M_{A_p}, respectively.

3.6 Conclusion and perspectives

In this chapter, we studied the interplay between frustrated electron-electron interactions and multiorbital effects on the spinless multiorbital Hubbard model that we derived in the previous chapter for the specific case of e_g-orbitals that corresponds to the physical situation in $AgNiO_2$.

After considering the noninteracting case, we obtained a sketch of the phase diagram with simple tight-binding and electrostatic considerations, corresponding to the weak and strong interaction limits of the Hartree approximation, respectively. Then, we introduced the unrestricted Hartree-Fock method, which provides an accurate description of the multiband kinetic properties. The results based on such technique reveal a very rich phase diagram. A number of original charge-ordered and orbitally ordered phases are displayed, whose occurrence can be tuned by varying the band structure parameters and which could be relevant to a variety of d-electron systems on the triangular lattice. These include threefold metallic charge-ordered phases such as the pinball liquid, which was originally predicted to occur in quarter-filled lattices and is shown here to be stable at half filling, as well as its dual, the inverse pinball liquid. These metallic charge orders are directly relevant to $AgNiO_2$. In this material, a robust threefold charge-ordered metal has been experimentally observed [9, 11], with oxygen atoms moving away from nickel at the center of hexagons due to the Coulomb

interaction that matches the pinball liquid pattern, which we therefore associate with a pinball state (see also Ref. [35]). An original insulating droplet phase with a large $\sqrt{12} \times \sqrt{12}$ periodicity is also obtained here, which was overlooked in previous studies of the extended Hubbard model and which could be closely related to the star of David charge-ordered phase of the triangular dichalcogenide compound $1T$-TaS_2 [20]. The insulating threefold pinball charge order phase obtained here could also find a possible experimental realization, as suggested in triangular adsorbate layers [124]. All these possible connections with the experiments emphasize the general nature of our study and should motivate further investigations in stabilizing original charge orders driven by frustrated electronic interactions and kinetic effects.

The unrestricted Hartree-Fock results are generally confirmed by exact diagonalization approach where the main features of the phase diagram are recovered.

Finally, we note that we have restricted our study to a perfectly stoichiometric case where the e_g doublet is initially quarter filled, corresponding to an average valence Ni^{3+} in $AgNiO_2$. It has been proposed, however, that the filling of the e_g levels in nickelates might actually differ from this value [125, 126], as extra electrons could be transferred from the oxygen $2p$-orbitals provided that the electrostatic cost $\tilde{U} = U - 3J_H$ on the Ni sites is sufficiently low [83, 122]. The very observation of a pinball state in $AgNiO_2$ indicates that the effective interaction $\tilde{U}$ is low in this material (see Fig. 3.5), and the existence of a "negative charge transfer" from the oxygen atoms is indeed compatible with the estimates of Ref. [11], which indicate a reduced average valence of 2.85+ per Ni. Studying the present model away from the perfectly quarter-filled configuration will certainly be of interest in view of these considerations.

Some results remain not fully understood, e.g. the mechanism of the transition from the metallic inverse pinball liquid phase to the insulating $\sqrt{12} \times \sqrt{12}$ droplet charge order, as well for the three transitions from orbital ordered state to the non-ordered ones. Also, the special case $t' = -t$, with the electron hole symmetry, can have interesting properties because the mean-field approach failed to give consistent results where conducting phases can be stabilized even for large values of $\tilde{U}$ instead of a Mott state. In order to study this special case, we chose to perform a perturbation theory with the Mott state as a starting point and derive a new effective Hamiltonian. This will be the purpose of the next Chapter.

Chapter 4

Orbital order in the Mott regime

4.1 Introduction

In the previous chapter, we have focused on the charge degree of fredom. We will now refine our interest on the orbital degree of freedom to explore more specifically the properties of the Mott state. In the strong Coulomb interaction regime, the charges are frozen in an insulating state, either a charge order, such as the Pinned Charge Order or the $\sqrt{12} \times \sqrt{12}$ Charge Order, or a Mott state. In the latter, there is one electron per site exactly. To explore the orbital degree of freedom, we apply a perturbation theory on the spinless multiorbital extended Hubbard model in the Mott state, a target space where all sites are singly occupied. In the following, we will consider the two e_g orbitals that can be seen as pseudo-spins 1/2. It is well known that the standard (extended) Hubbard model gives us a Heisenberg model in this limit [127]. Thus, in our derivation, we must recover the SU(2) Heisenberg Model at $t' = t$.

In this chapter, we will first derive the effective Heisenberg-like model from perturbation theory. Then, we will solve this new model with two methods, classical approach followed by Exact Diagonalization.

4.2 Derivation of the effective Hamiltonian

Let us recall the multiorbital extended Hubbard model seen in the previous chapter

$$H = \underbrace{-\sum_{\langle ij\rangle,\tau\tau'} \left(t_{ij}^{\tau\tau'} d_{i\tau}^{\dagger} d_{j\tau'} + \text{h.c.} \right)}_{K} + \underbrace{\tilde{U} \sum_{i=1}^{N_s} n_{i\uparrow} n_{i\downarrow} + V \sum_{\langle ij\rangle} \left(n_{i\uparrow} + n_{i\downarrow}\right) \left(n_{j\uparrow} + n_{j\downarrow}\right)}_{H_0}, \quad (4.1)$$

where K is the kinetic part of the Hamiltonian and H_0 the Coulomb interactions. We rewrite the variables $t = \rho c$ and $t' = \rho s$ with $c = \cos\theta$ and $s = \sin\theta$. The hopping integrals become

$$t_{\vec{u}_1} = \rho \begin{pmatrix} c & 0 \\ 0 & s \end{pmatrix}, \; t_{\vec{u}_2} = \frac{\rho}{4} \begin{pmatrix} c+3s & \sqrt{3}(c-s) \\ \sqrt{3}(c-s) & 3c+s \end{pmatrix}$$

and

$$t_{\vec{u}_3} = \frac{\rho}{4} \begin{pmatrix} c+3s & -\sqrt{3}(c-s) \\ -\sqrt{3}(c-s) & 3c+s \end{pmatrix},$$

where $\vec{u}_{l=1,2,3}$ are the three directions of the lattice $\vec{u}_1 = (1,0)$, $\vec{u}_2 = \left(1/2, \sqrt{3}/2\right)$, and $\vec{u}_3 = \left(-1/2, \sqrt{3}/2\right)$. For $\theta = \pi/4$, which corresponds to the isotropic case ($t = t'$), the off-diagonal terms cancel and we recover the SU(2) point where the model reduces to the standard hopping integrals for the single-band spinful Hubbard model.

4.2.1 Population imbalance chemical potential

In real systems, the orbitals are not necessarily degenerate. Indeed, even though we considered the crystal-field splitting, other effects that we neglected can split the orbitals, such as the Jahn-Teller effect [74, 75]. The motivation here is to add the energy gap between orbitals in case they are not strictly degenerate. This energy gap between orbitals has the form of a magnetic field, which is convenient because it will allow us to compare our results with previous study on the Heisenberg model in a magnetic field. So the field is the analog for the orbitals to the magnetic field

$$H_1 = -h \sum_{i=1}^{N_s} \tau_i^z. \tag{4.2}$$

This term is analogous to a chemical potential which splits the orbitals, formally,

$$H_1 = -\sum_{i=1}^{n_s} \mu_\uparrow n_{i\uparrow} + \mu_\downarrow n_{i\downarrow}$$

with $\mu_\uparrow = -\mu_\downarrow = \mu$.

This term is added to the Hamiltonian H and we will now apply a perturbation theory to address the large $\tilde{U}$ region of the phase diagram. We take the Coulomb interaction terms H_0 as the unperturbed Hamiltonian and we will treat the rest $(K + H_1)$ perturbatively.

4.2.2 Ground state of the unperturbed Hamiltonian

We refine our study on the Mott state. As seen in the previous chapter, it is necessary, in order to avoid charge order, to have the local Coulomb interaction three times greater than the nearest neighbor Coulomb interaction ($V < \tilde{U}/3$). Then, we need the local Coulomb interaction to be much greater than the kinetic energy, which is the case when $\tilde{U} \gg t, t'$.

The ground state of the unperturbed Hamiltonian H_0 in this limit, referred to as the classical ground state in the following, is infinitely degenerate. This term is diagonal in real space[1] and Mott states, one electron per site exactly, denoted $|n^{(0)}\rangle$, gives the lowest classical energy

$$E_0|n^{(0)}\rangle = H_0|n^{(0)}\rangle = 3N_sV|n^{(0)}\rangle.$$

The general form of this state is

$$|n^{(0)}\rangle = \prod_{i=1}^{Ns} d^\dagger_{i\tau_i}|0\rangle,$$

where $\tau_i = \uparrow, \downarrow$ is the occupied orbital on site i. It is necessary to fix a gauge convention for the fermionic sign. We choose a gauge where sites, from 1 (left) to N_s (right), are together with first orbital $\uparrow$ (left) and $\downarrow$ (right)

$$d^\dagger_{1\uparrow}d^\dagger_{1\downarrow}d^\dagger_{2\uparrow}d^\dagger_{2\downarrow}...d^\dagger_{N_s\uparrow}d^\dagger_{N_s\downarrow}|0\rangle. \tag{4.3}$$

We note D the ensemble of all 2^{N_s} Mott states.

4.2.3 First order corrections

The first order correction to the energy is

$$E_n^{(1)} = \langle n^{(0)}| \left(K + H_1\right) |n^{(0)}\rangle = 0 - \mu \sum_{i=1}^{N_s} \langle n^{(0)}|n_{i\uparrow}|n^{(0)}\rangle - \langle n^{(0)}|n_{i\downarrow}|n^{(0)}\rangle.$$

This energy depends on the considered Mott state n. The perturbation at first order on K is always zero because applying the perturbation on the classical ground state

$$d^\dagger_{i\tau_i}d_{j\tau_j}|n^{(0)}\rangle$$

[1] The kinetic term is diagonal in reciprocal space.

gives a state with the site j empty and i doubly occupied, which is out of the target sub-space. The energy of this state is higher. Indeed, $E = E_0 + \tilde{U} - V$ and at most $V = \tilde{U}/3$ according to Section 3.3, so, $E_{\min} = E_0 + 2\tilde{U}/3 > E_0$. In addition, it is not a Mott state so it does not belong to the ensemble of the classical ground state, which is required by the perturbation theory.

Now that we have computed the correction to the energy, one needs the correction to the wavefunction

$$|n^{(1)}\rangle = \sum_{k \notin D} \frac{\langle k^{(0)}| \left(K + H_1\right) |n^{(0)}\rangle}{E_0 - E_k^{(0)}} |k^{(0)}\rangle = \sum_{k \notin D} \left(0 + E_n^{(1)}\right) \frac{\langle k^{(0)}|n^{(0)}\rangle}{E_0 - E_k^{(0)}} |k^{(0)}\rangle,$$

where one sums over all states different from the Mott states. The basis is orthonormal, so it cancels the contribution at the first order to the wavefunction

$$|n^{(1)}\rangle = \sum_{k \notin D} E_n^{(1)} \frac{\delta_{k,n}}{E_0 - E_k^{(0)}} |k^{(0)}\rangle = 0.$$

Because the first order in perturbation is always zero for the kinetic term, we will go further, i.e. to the second order in perturbation.

4.2.4 Second order corrections

The second order of perturbation theory for a degenerate ground state of H_0 is

$$H_{mn}^{\text{eff}} = \sum_{l \notin D} \frac{\langle m| \left(K + H_1\right) |l\rangle \langle l| \left(K + H_1\right) |n\rangle}{E_0 - E_1} \tag{4.4}$$

$$= \sum_{l \notin D} \frac{1}{E_0 - E_1} \Bigg(\langle m|K|l\rangle\langle l|K|n\rangle + \langle m|K|l\rangle \underbrace{\langle l|H_1|n\rangle}_{=0} + \underbrace{\langle m|H_1|l\rangle}_{=0} \langle l|K|n\rangle$$

$$+ \underbrace{\langle m|H_1|l\rangle}_{=0} \underbrace{\langle l|H_1|n\rangle}_{=0} \Bigg) \tag{4.5}$$

where $E_m = E_n = E_0$ the energy of the classical ground states $|m\rangle$ and $|n\rangle$, $E_l = E_1$ the energy of the virtual state $|l\rangle$ and the difference $E_0 - E_l = V - \tilde{U}$.

The second order corrections are null for H_1. Indeed this perturbation is a diagonal operator so the latter does not project a classical ground state to another state, which means the ensemble of indexes l in Equation 4.5 is empty, therefore there is no correction at second order.

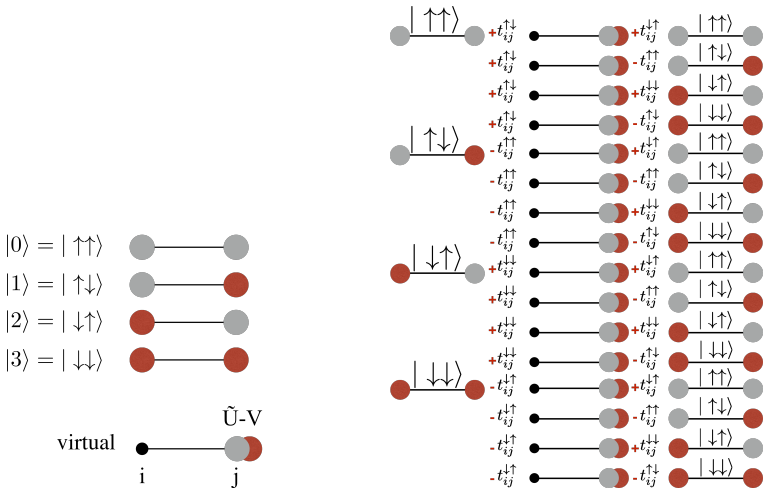

Fig. 4.1 (top left) The 4 inequivalent processes on one link starting from a Mott state with one electron on site i and one on site j to a virtual state (bottom left), unique if it exists, with two electrons on site j by application of the perturbation K. The red and gray disks represent the electron on orbital $\uparrow$ and $\downarrow$, respectively. (right) The 16 inequivalent processes on one link starting from the same Mott state to the virtual state then return to one of the initial states by the second application of the perturbation K (Mott state). Each step, the system gain or lose an energy $t_{ij}^{\tau\tau'}$ depending on the fermionic sign (in red).

As K does not project $|n\rangle$ nor $|m\rangle$ on any other classical ground state that belongs to the ensemble D as mentioned above, we can add this ensemble in the sum over l without changing the results to make appear the resolution of the identity ($I = \sum_l |l\rangle\langle l|$), so we obtain

$$H^{\text{eff}}_{mn} = \frac{\langle m|KK|n\rangle}{E_0 - E_1} \tag{4.6}$$

$$= -\frac{1}{W} \sum_{\langle ij\rangle,\tau\tau'} \sum_{\langle kl\rangle,\tau''\tau'''} t_{ij}^{\tau\tau'} t_{kl}^{\tau''\tau'''} \langle m|(d^\dagger_{i\tau} d_{j\tau'} + \text{h.c})(d^\dagger_{k\tau''} d_{l\tau'''} + \text{h.c})|n\rangle, \tag{4.7}$$

where $W = \tilde{U} - V$. Notice that because of the condition on the strength of Coulomb interaction, the prefactor $\frac{1}{V-\tilde{U}}$ is always negative. This statement will be important later because this prefactor will give an antiferromagnetic coupling at the origin of the frustration.

Equation 4.7 describes processes where an electron jumps on a neighbor and comes back on the same site, but not necessarily on the same orbital. The second order perturbation on the microscopic model defined on nearest neighbors makes the effective Hamiltonians depend only on bonds (i, j), so it is convenient to think in term of links between two nearest neighbors. On a bond between site i and j, let us consider the 4 states, denoted as $|n\rangle = |\tau_i\tau_j\rangle$, with $n = 0, 1, 2, 3$ and $\tau = \uparrow, \downarrow$, the two e_g orbitals. By application of the perturbation K, there is only one virtual state, if it exists. The left panel of Figure 4.1 summarizes the four Mott states (top) and the virtual state (bottom). The second application of the perturbation K projects the virtual state to all possible $|n\rangle$. Each application of K lowers the energy by $t_{ij}^{\tau\tau'}$. All 16 possible processes in one direction with the corresponding energy $t_{ij}^{\tau\tau'}$ and the fermionic sign in red are listed on the right panel in Figure 4.1. The fermionic sign here comes from the rewriting of the virtual state in our gauge choice (see Eq. 4.3). Figure 4.1 represents the action of the perturbation in one bond direction.

In the basis $|0\rangle, |1\rangle, |2\rangle, |3\rangle$, gathering all these processes and taking into account their complex conjugate gives the following effective Hamiltonian on one bond

$$H^{\text{eff}}_{\vec{u}_l} = \frac{\rho^2}{W} \begin{pmatrix} -2t_{\vec{u}_l}^{\uparrow\downarrow 2} & -t_{\vec{u}_l}^{\uparrow\downarrow}\left(t_{\vec{u}_l}^{\downarrow\downarrow} - t_{\vec{u}_l}^{\uparrow\uparrow}\right) & -t_{\vec{u}_l}^{\uparrow\downarrow}\left(t_{\vec{u}_l}^{\downarrow\downarrow} - t_{\vec{u}_l}^{\uparrow\uparrow}\right) & 2t_{\vec{u}_l}^{\uparrow\downarrow 2} \\ -t_{\vec{u}_l}^{\uparrow\downarrow}\left(t_{\vec{u}_l}^{\downarrow\downarrow} - t_{\vec{u}_l}^{\uparrow\uparrow}\right) & -t_{\vec{u}_l}^{\uparrow\uparrow 2} - t_{\vec{u}_l}^{\downarrow\downarrow 2} & 2t_{\vec{u}_l}^{\uparrow\uparrow} t_{\vec{u}_l}^{\downarrow\downarrow} & -t_{\vec{u}_l}^{\uparrow\downarrow}\left(t_{\vec{u}_l}^{\uparrow\uparrow} - t_{\vec{u}_l}^{\downarrow\downarrow}\right) \\ -t_{\vec{u}_l}^{\uparrow\downarrow}\left(t_{\vec{u}_l}^{\downarrow\downarrow} - t_{\vec{u}_l}^{\uparrow\uparrow}\right) & 2t_{\vec{u}_l}^{\uparrow\uparrow} t_{\vec{u}_l}^{\downarrow\downarrow} & -t_{\vec{u}_l}^{\uparrow\uparrow 2} - t_{\vec{u}_l}^{\downarrow\downarrow 2} & -t_{\vec{u}_l}^{\uparrow\downarrow}\left(t_{\vec{u}_l}^{\uparrow\uparrow} - t_{\vec{u}_l}^{\downarrow\downarrow}\right) \\ 2t_{\vec{u}_l}^{\uparrow\downarrow 2} & -t_{\vec{u}_l}^{\uparrow\downarrow}\left(t_{\vec{u}_l}^{\uparrow\uparrow} - t_{\vec{u}_l}^{\downarrow\downarrow}\right) & -t_{\vec{u}_l}^{\uparrow\downarrow}\left(t_{\vec{u}_l}^{\uparrow\uparrow} - t_{\vec{u}_l}^{\downarrow\downarrow}\right) & -2t_{\vec{u}_l}^{\uparrow\downarrow 2} \end{pmatrix}. \tag{4.8}$$

We will now write this matrix explicitly for the three different directions using the different hopping integrals:

$$H^{\text{eff}}_{\vec{u}_1} = \frac{\rho^2}{W}\begin{pmatrix} 0 & 0 & 0 & 0 \\ 0 & -1 & 2cs & 0 \\ 0 & 2cs & -1 & 0 \\ 0 & 0 & 0 & 0 \end{pmatrix},$$

$$H^{\text{eff}}_{\vec{u}_2} = \frac{\rho^2}{8W}\begin{pmatrix} -3(c-s)^2 & -\sqrt{3}(c-s)^2 & -\sqrt{3}(c-s)^2 & 3(c-s)^2 \\ -\sqrt{3}(c-s)^2 & -5c^2-6sc-5s^2 & (3c+s)(c+3s) & \sqrt{3}(c-s)^2 \\ -\sqrt{3}(c-s)^2 & (3c+s)(c+3s) & -5c^2-6sc-5s^2 & \sqrt{3}(c-s)^2 \\ 3(c-s)^2 & \sqrt{3}(c-s)^2 & \sqrt{3}(c-s)^2 & -3(c-s)^2 \end{pmatrix}$$

and

$$H^{\text{eff}}_{\vec{u}_3} = \frac{\rho^2}{8W}\begin{pmatrix} -3(c-s)^2 & \sqrt{3}(c-s)^2 & \sqrt{3}(c-s)^2 & 3(c-s)^2 \\ \sqrt{3}(c-s)^2 & -5c^2-6sc-5s^2 & (3c+s)(c+3s) & -\sqrt{3}(c-s)^2 \\ \sqrt{3}(c-s)^2 & (3c+s)(c+3s) & -5c^2-6sc-5s^2 & -\sqrt{3}(c-s)^2 \\ 3(c-s)^2 & -\sqrt{3}(c-s)^2 & -\sqrt{3}(c-s)^2 & -3(c-s)^2 \end{pmatrix}.$$

4.2.5 Pseudospin representation

The two e_g orbitals can be viewed as a pseudospin. The question here is *Can we write the effective Hamiltonian in terms of spin 1/2 operators?* It is always possible to write a 4×4 hermitian matrix as a linear combination of Kronecker products of Pauli matrices (see Appendix E). We can use Equation E.3 to express the Hamiltonian in the new basis. Let us now explicitly write $H^{\text{eff}}_{\vec{u}_{l=1,2,3}}$ in the three directions

$$H^{\text{eff}}_{\vec{u}_1} = \frac{\rho^2}{W}\left(\tau\left(\sigma_i^+\sigma_j^- + \sigma_i^-\sigma_j^+\right) + \frac{1}{2}\sigma_i^z\sigma_j^z - \frac{1}{2}\right), \tag{4.9}$$

$$\begin{aligned} H^{\text{eff}}_{\vec{u}_2} &= \frac{\rho^2}{W}\left(\delta\left(\sigma_i^+\sigma_j^- + \sigma_i^-\sigma_j^+\right) + \xi\sigma_i^z\sigma_j^z + \alpha\left(\sigma_i^+\sigma_j^+ + \sigma_i^-\sigma_j^-\right)\right. \\ &- \left.\beta\left(\sigma_i^z\sigma_j^+ + \sigma_i^z\sigma_j^- + \sigma_i^+\sigma_j^z + \sigma_i^-\sigma_j^z\right) - \frac{1}{2}\right), \end{aligned} \tag{4.10}$$

$$\begin{aligned} H^{\text{eff}}_{\vec{u}_3} &= \frac{\rho^2}{W}\left(\delta\left(\sigma_i^+\sigma_j^- + \sigma_i^-\sigma_j^+\right) + \xi\sigma_i^z\sigma_j^z + \alpha\left(\sigma_i^+\sigma_j^+ + \sigma_i^-\sigma_j^-\right)\right. \\ &+ \left.\beta\left(\sigma_i^z\sigma_j^+ + \sigma_i^z\sigma_j^- + \sigma_i^+\sigma_j^z + \sigma_i^-\sigma_j^z\right) - \frac{1}{2}\right), \end{aligned} \tag{4.11}$$

with

$$\sigma^{\pm} = \frac{1}{2}\left(\sigma^x \pm \sigma^y\right)$$

and

$$\begin{cases} \alpha &= \frac{3(c-s)^2}{8} = \frac{3}{8} - \frac{3cs}{4} \\ \beta &= \frac{\sqrt{3}(c-s)^2}{8} = \frac{\sqrt{3}}{8} - \frac{\sqrt{3}cs}{4} \\ \delta &= \frac{(3c+s)(c+3s)}{8} = \frac{3}{8} + \frac{5cs}{4} \\ \tau &= 2cs \\ \xi &= \frac{1}{8} + \frac{3cs}{4}. \end{cases}$$

We can notice from these expressions that they are all a function of $cs = \cos(\theta)\sin(\theta) = \sin(2\theta)/2$, so the Hamiltonian is π-periodic. The case $t = t'$ correspond to $\theta = \pi/4$ and it is interesting to notice that the Hamiltonian is symmetric with respect to this value $H(\theta - \pi/4) = H(-\theta - \pi/4)$. We just need to study the Hamiltonian in the range $[\pi/4, 3\pi/4]$, other values of θ can be deduced using these two properties. The SU(2) point, for $t = t'$, is the only case where the Hamiltonian has symmetries.

As the energy is defined with respect to an arbitrary constant, in the following we will set to zero the diagonal component to these terms to simplify the expressions.

We finish this section with the pseudospin representation of the correction at first order to the energy which is rather simple because the matrix representation is directly a Pauli matrix

$$H_1 = -\mu \sum_i \sigma_i^z. \tag{4.12}$$

We can see that the chemical potential μ from Equation 4.12 matches the pseudo-magnetic field h in Equation 4.2.

Finally, the total effective Hamiltonian is

$$H^{\text{eff}} = \sum_{i=1}^{N_s} \sum_{l=1}^{3} H_{\vec{u}_l}^{\text{eff}} + H_1. \tag{4.13}$$

The index i stands for an orbital on site $\vec{r}_i = \alpha_i \vec{u}_1 + \beta_i \vec{u}_2$, α_i, β_i are integers, which interacts with an orbital on the direction l such that the position of the latter is $\vec{r}_i + \vec{u}_{l=1,2,3}$.

4.3 Classical orbitals

To study the effective Hamiltonian, Equation 4.13, we start with a simple method of classical approach analogous to classical spin. In fact, we will see that this approach captures most of the physics if we compare with exact diagonalizations (See Section 4.4). We will perform two equivalent classical treatments: with N_s vectors of three dimensions $\vec{\tau}_i = (\tau_i^x, \tau_i^y, \tau_i^z)$ using Equations 4.9, 4.10 and 4.11 in Section 4.3.1 and with an approach

in terms of linear combination of orbitals $|\tau_i\rangle = \tau_{i\uparrow}|\uparrow\rangle + \tau_{i\downarrow}|\downarrow\rangle$ using Equation 4.8 in Section 4.3.2. The idea for both of them is to minimize the energy. While equivalent, these methods take different path to minimize the energy and can help in avoiding spurious local minima.

In this section, we will first describe the two methods and show they are equivalent, then introduce the order parameters to identify the different phases and quickly review some results for the standard Heisenberg model before finally present the phase diagram.

Nota Bene: The prefactor $\frac{\rho^2}{W}$ corresponds to an antiferro-orbital coupling because its sign, positive, remains the same for the considered range of parameters. For now on, we normalize the Hamiltonian with this factor.

4.3.1 Classical spin approach

The idea of the first method is to minimize the energy with respect to $3N_s$ parameters, the ensemble of local orientations of pseudospin $\{\vec{\tau}_i = (\tau_i^x, \tau_i^y, \tau_i^z)\}$. In the Hamiltonian, we substitute the Pauli matrices $\vec{\sigma}_i$ by the coordinates of the vectors $\vec{\tau}_i$.

The number of parameters to minimize can be reduced by N_s using the fact that the norm of the vector $\vec{\tau}_i$ is a constant, so we can write their coordinates with spherical coordinates:

$$\begin{cases} \tau_i^x &= \cos\alpha_i \sin\beta_i \\ \tau_i^y &= \sin\alpha_i \sin\beta_i \\ \tau_i^y &= \cos\beta_i, \end{cases}$$

with $\beta_i \in [0, \pi[$ and $\alpha_i \in [0, 2\pi[$. Now, we have only $2N_s$ variables to minimize. Let us write explicitly the form of the energy

$$E = \sum_{\langle ij \rangle} h_{ij} + H_1$$

with

$$
\begin{aligned}
h_{\vec{u}_1} &= \frac{1}{2}\left(\cos\left(\beta_i\right)\cos\left(\beta_j\right) + 2cs\cos\left(\alpha_i-\alpha_j\right)\sin\left(\beta_i\right)\sin\left(\beta_j\right)\right), \\
h_{\vec{u}_2} &= \frac{1}{8}\Big(\cos\left(\beta_i\right)\Big(\sqrt{3}(2cs-1)\cos\left(\alpha_j\right)\sin\left(\beta_j\right) + (6cs+1)\cos\left(\beta_j\right)\Big) \\
&+ \sin\left(\beta_i\right)\big(8cs\sin\left(\alpha_i\right)\sin\left(\alpha_j\right)\sin\left(\beta_j\right) \\
&\quad + \cos\left(\alpha_i\right)\Big((2cs+3)\cos\left(\alpha_j\right)\sin\left(\beta_j\right) + \sqrt{3}(2cs-1)\cos\left(\beta_j\right)\Big)\Big)\Big), \\
h_{\vec{u}_3} &= \frac{1}{8}\Big(\cos\left(\beta_i\right)\Big(-\sqrt{3}(2cs-1)\cos\left(\alpha_j\right)\sin\left(\beta_j\right) + (6cs+1)\cos\left(\beta_j\right)\Big) \\
&+ \sin\left(\beta_i\right)\big(8cs\sin\left(\alpha_i\right)\sin\left(\alpha_j\right)\sin\left(\beta_j\right) \\
&\quad + \cos\left(\alpha_i\right)\Big((2cs+3)\cos\left(\alpha_j\right)\sin\left(\beta_j\right) - \sqrt{3}(2cs-1)\cos\left(\beta_j\right)\Big)\Big)\Big), \\
H_1 &= -h\sum_{i=1}^{N_s}\cos\left(\beta_i\right).
\end{aligned}
$$

One can notice that it depends only on the product cs, as previously mentioned in Section 4.2.5.

To minimize this function, we developed a C++ program using the library Dlib [128], especially the function find_min_box_constrained. The strategy to find the minimum is the Broyden-Fletcher-Goldfarb-Shanno (BFGS) algorithm, where the derivative is computed numerically. The algorithm stops when the difference between variables from two iterations is less than an arbitrary precision, here set to 10^{-14}, exactly as introduced for mean-field in Equation 3.10.

The only size effect of this approach is that the unit-cell of the global minimum must be compatible with the studied cluster. The reason is simple: if a solution is found for a size n times the unit-cell, for example 3, $N_s = 3n$, we can plug this solution for any cluster such that $N_s/3$ is an integer and the energy per site will be the same. In practice, it is really convenient, especially in case of incommensurate state as the order depends on the size of the finite system, because we can compare the energy per site of the different sizes. Here, we took every clusters such as $L_x = L_y$ or $L_x = 3L_y$ and $N = L_xL_y/3$ is an integer. L_x and L_y are the number of sites along the directions $\vec{u}_1$ and $\vec{u}_2$. We computed for cluster up to 576 sites. Larger sizes are easily accessible in terms of memory, but the computation time of each point takes too much time to perform a scan over the whole range of parameters.

The range for the parameter θ has been discussed previously in Section 4.2.5 and the range that we choose for the field h is $[0, 6]$ because it captures all the physics. Indeed, the cutoff is done for $h = 6$ because it is a value high enough to overcome all other terms and ensure to be in the ferro-orbital phase. It is enough to consider only

positive values because due to the symmetries between orbitals ↑ and ↓; a negative sign of h corresponds to change the sign of the chemical potential. As our two e_g orbitals are equivalent, it just switches orbital ↑ and ↓.

We performed scans for given value of θ from $h = 0$ to $h = 6$ and vice versa where we initialized the local orientations of the orbitals $\vec{\tau}_i$ for each scan with random numbers. At each step in h, increasing or decreasing h by a small amount, we inject the previous solution, i.e. the ensemble of $\{\vec{\tau}_i\}$, as a starting point for the minimization. It speeds up the algorithm because if the solution at the current step is close to the previous one, for example when the phase is the same or in case of second order transition, the procedure will find quickly the solution. The fact that we scan by increasing then decreasing h avoids to be trapped in a local minima in case of a first order transition. Finally, we used this trick to scan in h as we expect rather smooth transition with classical approach, the field will polarize the orbitals, but not in θ because more drastic changes can happen in case of transition.

4.3.2 Linear Combination

Instead of substituting the Pauli matrices σ_i by a vector τ_i, we can also work in a basis of bonds. We will see later that this assumption makes this approach equivalent to the classical calculations that we explained previously. A site is now described by a vector which is a linear combination of orbitals ↑ and ↓: $|\tau_i\rangle = \tau_{i\uparrow}|\uparrow\rangle + \tau_{i\downarrow}|\downarrow\rangle = \tau_{i\uparrow}d^\dagger_{i\uparrow}|0\rangle + \tau_{i\downarrow}d^\dagger_{i\downarrow}|0\rangle$. The wave function to minimize is

$$|\mathrm{WF}\rangle = \sum_{i,\tau} \tau_{i\tau}|\tau\rangle,$$

where $\tau_{i\tau} \in \mathbb{C}$ and $|\tau\rangle = |\uparrow\rangle, |\downarrow\rangle$. It means we will minimize the wave function

$$E = \langle \mathrm{WF}|H^{\mathrm{eff}}|\mathrm{WF}\rangle.$$

Only terms of the form $\sigma_i^\alpha \sigma_j^\beta$ exist , with $\alpha, \beta = x, y, z$. This observation will simplify the problem to solve because we only need to compute terms of the form

$$\langle \mathrm{WF}|\sigma_i^\alpha \sigma_j^\beta|\mathrm{WF}\rangle = \langle \mathrm{WF}|\sigma_i^\alpha|\mathrm{WF}\rangle\langle \mathrm{WF}|\sigma_j^\beta|\mathrm{WF}\rangle.$$

The only non-zero term of each bracket are on one site

$$\langle \tau_i\tau_j|\sigma_i^\alpha \sigma_j^\beta|\tau_i\tau_j\rangle = \langle \tau_i|\sigma_i^\alpha|\tau_i\rangle\langle \tau_j|\sigma_j^\beta|\tau_j\rangle,$$

where a link between two nearest neighbors is

$$|\tau_i\tau_j\rangle = |\tau_i\rangle \otimes |\tau_j\rangle = \tau_{i\uparrow}\tau_{j\uparrow}|\uparrow\uparrow\rangle + \tau_{i\uparrow}\tau_{j\downarrow}|\uparrow\downarrow\rangle + \tau_{i\downarrow}\tau_{j\uparrow}|\downarrow\uparrow\rangle + \tau_{i\downarrow}\tau_{j\downarrow}|\downarrow\downarrow\rangle,$$

with $|\tau\tau'\rangle = |\tau\rangle \otimes |\tau'\rangle$. The basis $\{|\tau_i\rangle\}$ is orthonormal , so

$$\langle\tau_i|\tau_j\rangle = \delta_{ij}. \tag{4.14}$$

We can rewrite $|\tau_i\rangle = \cos(\beta_i/2)\,|\uparrow\rangle + \sin(\beta_i/2)\,e^{i\alpha_i}|\downarrow\rangle$ with $\alpha_i, \beta_i \in [0, 2\pi[$, as it satisfies Equation 4.14.

All the statements we made for the first approach apply here as well.

- We also developed a C++ code using Dlib library with the same options.
- The size effects behave the same.
- We took the same clusters.
- We used the same tricks to speed up the convergence of the Broyden-Fletcher-Goldfarb-Shanno algorithm.

This method is more time consuming than the direct substitution that we saw previously in Section 4.3.1 because it deals with complex numbers. Nevertheless, we also used this approach because we can directly compare the results from both methods to avoid being trapped in a local minimum. Indeed, these methods never assure that the solution that we find is a global minimum, even for a closed domain as it never scan the whole ensemble of each parameters.

To see the equivalence with the direct substitution seen in Section 4.3.1, we introduce a vector

$$\vec{\tau_i'} = \begin{pmatrix} \langle\tau_i|\sigma^x|\tau_i\rangle \\ \langle\tau_i|\sigma^y|\tau_i\rangle \\ \langle\tau_i|\sigma^z|\tau_i\rangle \end{pmatrix} = \begin{pmatrix} \cos\alpha_i \sin\beta_i \\ \sin\alpha_i \sin\beta_i \\ \cos\beta_i \end{pmatrix} = \begin{pmatrix} \tau_i^{x'} \\ \tau_i^{y'} \\ \tau_i^{z'} \end{pmatrix}.$$

We see immediately that it matches the previous form of the vector seen in Section 4.3.1. We substitute these coordinates with the Pauli matrices in the Hamiltonian as we did previously, and we obtain the same energy because this vector satisfies the only constraint which is to cover all the unit sphere.

4.3.3 Order parameters

Before presenting the results, we will introduce the order parameters used to characterize all phases.

- The polarization along one direction $\alpha = x, y, z$ that we introduced in Section C.1 (see Equation C.2)

$$\tau^{\alpha} = \frac{1}{N_s} \sum_{i=1}^{N_s} \tau_i^{\alpha}.$$

  Typically, τ^z will be non-zero at large field h, as the latter minimize the energy when the orbitals have a finite polarization along the z axis.

- The structure factor, similar to the orbital-orbital correlation (see Equation C.3)

$$\langle \tau\left(\vec{k}\right) \tau\left(-\vec{k}\right) \rangle = \frac{1}{N_s^2} \sum_{\vec{k} \in \mathrm{BZ}} \vec{\tau}_i . \vec{\tau}_j e^{-i\vec{k}.(\vec{r}_i - \vec{r}_j)},$$

  where BZ stands for Brillouin zone. The latter is defined in Section A.1.2. To shorten the notation, we will write the structure factor $\tau\left(\vec{k}\right)$ in the following.

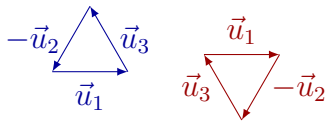

Fig. 4.2 The two types of triangles considered for the chirality.

- The chirality gives information about the order in a triangle. The two types of triangle are depicted in Figure 4.2: up (blue) and down (red). From now on, let us consider only the up triangles. Because chirality is defined on this three-sublattice, it is only relevant when the structure factor is on the K-point. The chirality can be of two types, scalar or vectorial. The scalar chirality is [129]

$$\chi^s = \frac{1}{N_s} \sum_{i=1}^{N_s} \vec{\tau}_i . (\vec{\tau}_{i+\mathrm{nn1}} \times \vec{\tau}_{i+\mathrm{nn2}}),$$

  with i+nn1, respectively i+nn2, the index nearest neighbors along $\vec{u}_1$, respectively $\vec{u}_2$. The latter is equal to zero when it is chiral, i.e. when the vectors of each triangle on the lattice can form a closed loop (in a plane), which is characteristic of the 120° order because all vectors have the same norm. The vectorial chirality

on one triangle is [130]

$$\vec{\chi}_i = \frac{2}{3\sqrt{3}} \left(\vec{\tau}_i \times \vec{\tau}_{i+\mathrm{nn1}} + \vec{\tau}_{i+\mathrm{nn1}} \times \vec{\tau}_{i+\mathrm{nn2}} + \vec{\tau}_{i+\mathrm{nn2}} \times \vec{\tau}_i \right)$$

which gives informations about orders between the triangles. It is more convenient to look at this quantity in the reciprocal space:

$$\chi(\vec{k}) = \frac{1}{N_s^2} \sum_{\vec{k} \in FBZ} \vec{\chi}_i . \vec{\chi}_j e^{-i\vec{k}.(\vec{r}_i - \vec{r}_j)},$$

analogous to the structure factor. To compare with the scalar form, $\chi(\Gamma) = 1$. when $\chi^s = 0$.

4.3.4 Heisenberg model

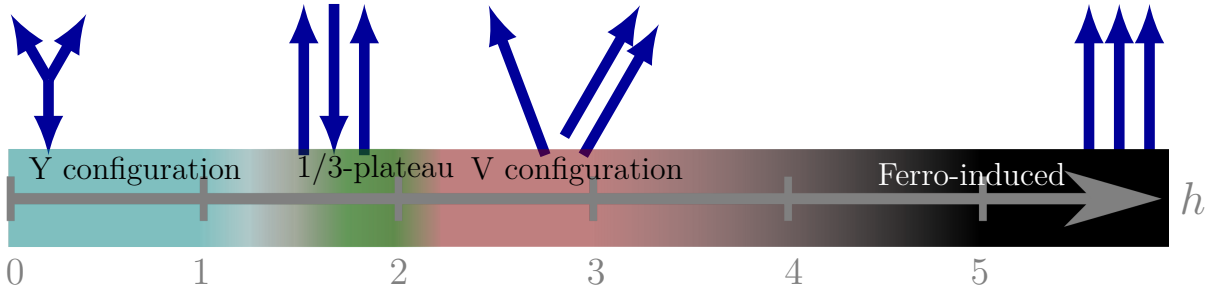

Fig. 4.3 Cartoon of a phase diagram for the Heisenberg model on the triangular lattice with a magnetic field when gathering results from different approaches (see text). The 1/3-plateau is not present in classical approaches. The different phases of the phase diagram are sketched on the top. From left to right: Y configuration, 1/3-plateau, V configuration and Ferro-induced phase.

As mentioned before, the isotropic case $t = t'$, or $\theta = \pi/4$, corresponds to the Heisenberg model. It is always good for a new model such as the one studied here to benchmark known limit cases. Although Heisenberg model has a simple form, it is still widely studied because of the difficulties encountered to solve it, especially when the frustration is strong. An exhaustive bibliography about the Heisenberg model for the triangular lattice is beyond the scope of this thesis, however a schematic phase diagram is shown Figure 4.3 where each color corresponds to a phase. This is shown by a gradient in opacity in the figure.

This schematic phase diagram is based on previous studies. One can cite for example an attempt to solve it exactly in 1986 [131], more recently Monte Carlo simulations in

2011 [132], Density Matrix Renormalization Group (DMRG) approach in 2012 [133], 1/S expansion by Chubukov group in 2014 [134], Classical and Cluster Mean-Field (CMF) approaches in 2014 [135] followed by the recent (October 2015) dilute Bose gas expansion, valid in the high field regime performed by the same group [136].

There are four phases: the Y configuration, the 1/3-plateau (only for quantum approaches), the V configuration and the fully polarized phase. Cartoons of the classical phases are drawn on top of the phase diagram in Figure 4.3.

Depending on the method, the transition lines do not appear at the same value of h. The transition lines also shifts from one study to another because of the cutoff on the order parameters. The transition from the V configuration to the Ferro-induced is a perfect example.

Notice that our study is consistent with these results, excepted the 1/3-plateau which is not possible classically, but found in the quantum approach (See Section 4.4).

One needs to define when the order parameters is close enough to zero. In the example of the V configuration to ferro-induced phase, the value of h_c at which the transition happen will strongly depends on this criteria because $1 - S^z$ goes smoothly and slowly to zero. If the criteria is 0.1 or 0.01, in this case, it can shift h_c to a value close to 3, to a critical field h_c close to 5.

4.3.5 Classical phase diagram

The phase diagram from the classical approach is presented in Figure 4.4. It is build by gathering results for both methods (Section 4.3.1 and Section 4.3.2) using sizes up to 576 sites. Before describing the different areas, let us give a quick overview of what can be expected then emphasize specific values of θ.

The line at $\theta = \frac{\pi}{4}$ corresponds to the isotropic case, in other words to the Heisenberg model. We have already discussed the results. Away from the isotropic case, we have a XXZ-like model with extra terms. One of them is $\alpha\left(\sigma_i^+\sigma_j^+ + \sigma_i^-\sigma_j^-\right) = \frac{\alpha}{2}\left(\sigma_i^x\sigma_j^x - \sigma_i^y\sigma_j^y\right)$. When α is large and positive, close to $\theta = \frac{3\pi}{4}$ (modulo π), the orbitals are aligned in the same way along y axis to minimize the energy. At strong field h, there is a large gap between the orbitals. Thus, only one is filled. It is the ferro-orbital phase, where $\tau^z = 1$.

There are specific values of θ we want to emphasize for the correspondence with the previous chapter.

- $\theta = \frac{\pi}{4}$ is the isotropic case, it corresponds to the Heisenberg model as mentioned previously.

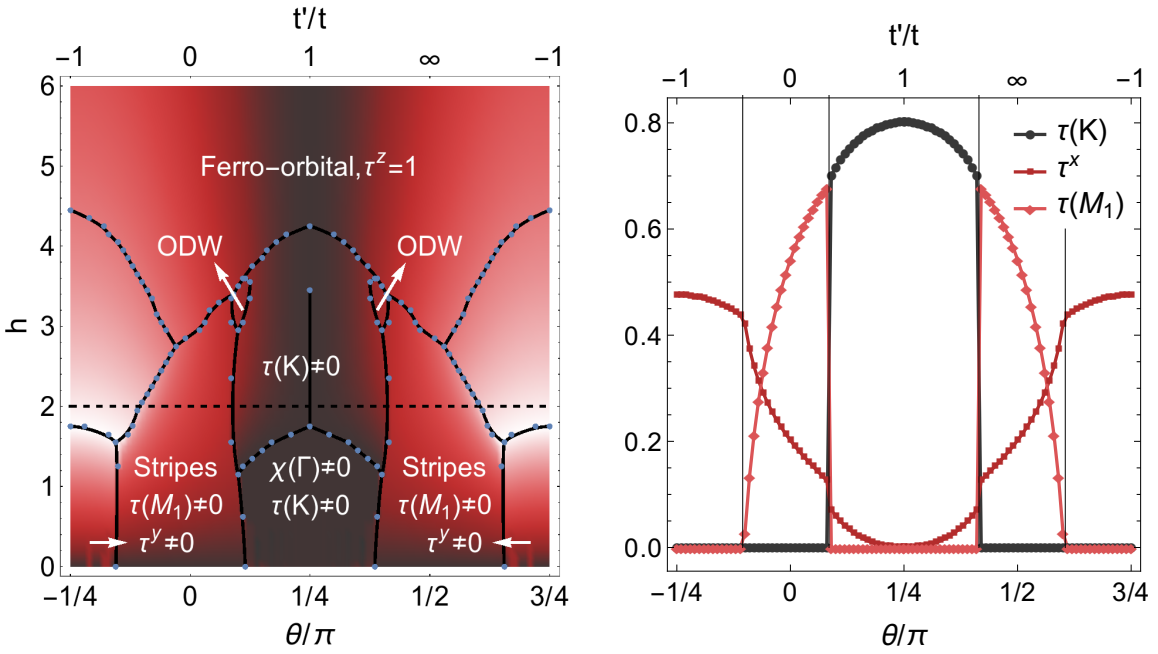

Fig. 4.4 (left) Phase diagram for classical orbitals as a function of θ and h. The labels are the different order parameters used to identify the phases. The background correspond to the value of τ^x. (right) Evolution at $h = 2$ (dashed line on left panel) of some order parameters: τ^x, $\tau(K) = \tau(K_1) + \tau(K_2)$ and $\tau(M_1)$.

- $\theta \simeq 0.147584\pi$ corresponds to $t'/t = 1/2$.
- $\theta \simeq -0.102416\pi$ corresponds to $t'/t = -1/3$.
- $\theta = -\frac{\pi}{4}$ ($t'/t = -1$) is the electron/hole symmetric point (See Section 3.2).
- $\theta = \frac{\pi}{2}$ corresponds to $t = 0$.

We will now describe the phase diagram in more details.

Close to the Heisenberg model

Let us focus first on the area of the phase diagram close to the Heisenberg model, so around $\theta = \frac{\pi}{4}$, where we recover all known classical phases (see Section 4.3.4).

The 120° phase appears at zero-field characterized by all the τ^α are zero, structure factor has a peak on the K-point and the vectorial chirality has a peak on the Γ point. Because of the degeneracy of this state, the 120° order can belong to any plane.

In presence of a weak field, in the area $\chi(\Gamma) = 0$ and $\tau(K) = 0$ on Figure 4.4, it becomes the more general Y configuration, as sketched in the left panel of Figure 4.5,

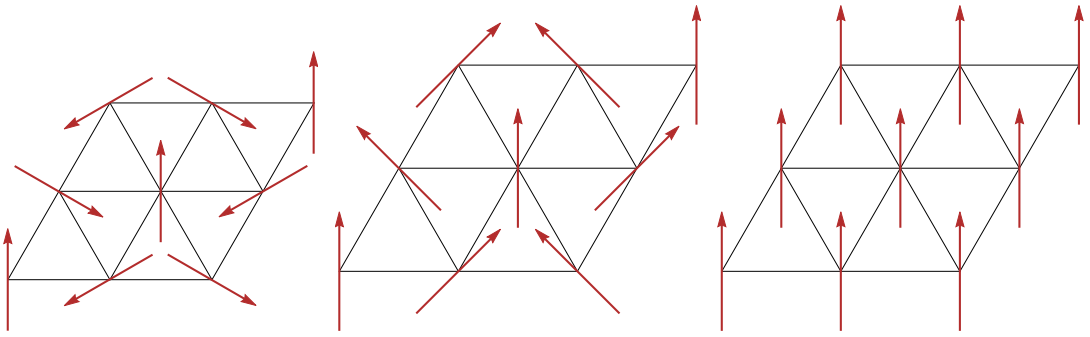

Fig. 4.5 Sketches of the phases found in model Equation 4.13 close the Heisenberg model. From left to right: The Y configuration, the V configuration and the ferro-orbital phase. The orbitals are projected in the xz-plane.

where orbitals start to have a finite τ^z component which lifts the degeneracy for $\theta \neq \pi/4$ and therefore project orbital in the xy-plane.

There is a transition to another threefold orbital order, the V configuration, sketched in the middle panel of Figure 4.5. The structure factor remains at the K-point with two orbitals are equivalent on the three-sublattice but the chirality goes to zero (area $\tau\,(K) = 0$ on Figure 4.4).

At strong filed, the ferro-orbital phase is stabilized, see sketch on the right panel of Figure 4.5, with all orbitals completely polarized, $\tau^z = 1$, thus all other order parameters are zero (area $\tau^z = 1$ on Figure 4.4). This phase is the equivalent to the field-induced ferromagnetic phase in the Heisenberg model.

Away from the isotropic case

Let us now explore the other areas of the classical phase diagram.

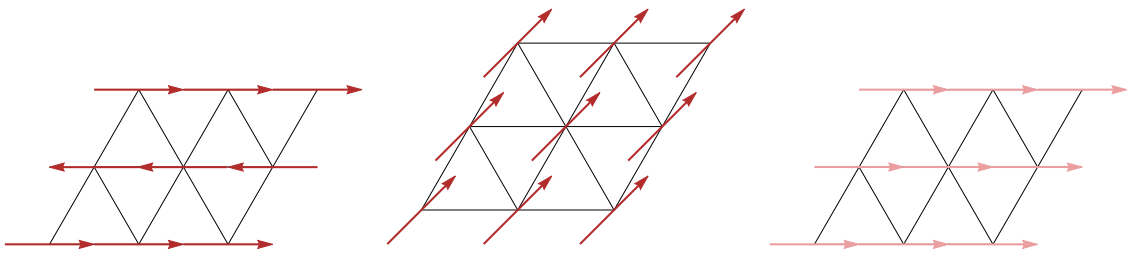

Fig. 4.6 Sketches of the commensurate phases found in model Equation 4.13 that are missing in the Heisenberg model. From left to right: Stripes phase, xz phase. and y phase. The orbitals are projected in the xz-plane on the left and middle and yz-plane on the right.

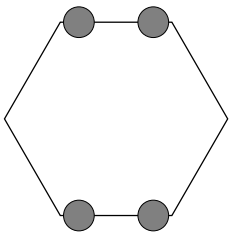

Fig. 4.7 Orbital density wave found in model Equation 4.13 that are missing in the Heisenberg model. Structure factor of the ODW in the first Brillouin Zone for $\theta = 0.4\pi$ and $h = 3$ for a cluster of 324 sites. The two inequivalent points are represented with the corresponding equivalent on the other edge. The radius of the disk is in arbitrary unit. The disk at the Γ point does not appear.

Away from the isotropic case, in the area $\tau(M) = 0$ on Figure 4.4, a transition happens to striped order characterized by a peak in structure factor at the M_1 point (see Brillouin zone in Figure 3.17). This point corresponds to stripes in the $\vec{u}_1$ direction, as sketched on left panel of Figure 4.6. It comes from the anisotropy of the model. It is an effective ferro-orbital coupling (negative coupling) in the $\vec{u}_1$ direction and antiferro-orbital coupling (positive coupling) in the other directions.

There is an incommensurate order called Orbital Density Wave (ODW) in the area between the threefold orbital order and the stripes. The structure factor is on the border of the Brillouin zone, between the K and M_1 point, as shown in Figure 4.7.

Far from the isotropic case ($\theta \simeq \frac{3\pi}{4}$) every orbital are along the y axis at zero field (area $\tau^y \neq 0$ on Figure 4.4), as sketched in right panel of Figure 4.6. The field will continuously mix the y component with the x and z components. In terms of structure factor, it corresponds to a peak at the Γ-point. We can explain this phase by writing the Hamiltonian (Eq. 4.13) with the Pauli matrices instead of the σ^+ and σ^- operators, which leads to a $-\alpha\sigma_i^y\sigma_j^y$ term. Because the term α is large in this case, we can see that the term $-\alpha\sigma_i^y\sigma_j^y$ drives the system. It minimizes the energy to have two nearest neighbors with the same sign giving a non-zero τ_i^y component.

Finally, the area without label is a phase where all sites are equivalent so the structure factor has a peak at the Γ-point with non-zero τ^x and τ^z components, as sketched in the middle panel of Figure 4.6. Notice the absence of the polarization along y axis.

With this simple classical approach, we unravel three novel phases far from the isotropic point. However we miss the 1/3-plateau stabilized by the quantum fluctuation that we neglected. We will treat exactly the effective Hamiltonian in the next section

to recover the 1/3-plateau because of the presence of quantum fluctuations and to confirm that we capture the physical properties with the classical approach.

4.4 Exact Diagonalization

In this section, we will solve the Hamiltonian exactly because the former approach does not capture the quantum fluctuations of the system.

Due to the huge size of Hilbert space, exact diagonalization can be done for small systems only. Indeed, the memory consumption is at least proportional to the Hilbert space size for sparse matrices[2] and Hilbert space size grows exponentially with the number of sites: $2^N = e^{N \ln 2}$. It means each time that the size of the cluster increases by one, the resources consumed qre double, so we immediately see that the size of the system is the limitation.

We will see in the first part of this section that we can use the symmetries of the system to reduce the size of Hilbert space, in particular the translations and the point group symmetries, because we can block-diagonalize the Hamiltonian. Then, we will present the results obtained with brute-force diagonalization for the two available clusters within our computing limitation: 12 and 16 sites. Brute-force diagonalization gives access to the spectrum and the wavefunctions as to the degeneracy. Finally, we will present the results obtained with the Lanczos algorithm, an iterative method which gives access to the ground state of a non-degenerate system. It allows us to increase the size of the system up to 24 sites[3]. The problem is then to extract the thermodynamic limit from such small sizes with so few points.

The states of the art for the Heisenberg model are:

- 39 spins 1/2 for the Heisenberg model on the triangular lattice reached in Januar 2004 with SPINPACK [137].
- 42 spins 1/2 on a linear chain (January 2009) and square lattice (April 2008) with the same program package [137].
- 63 spins 1/2 on a kagome lattice in 2013 [138].

Because our system does not have all the symmetries of the Heisenberg model, we are far from reaching such size. Indeed, S^z is not conserved and, as we will see right after, our Hamiltonian is C_2 in general, not C_{6v}.

[2] A sparse matrix is a matrix where only non-zero elements are stored.

[3] A 36 sites cluster can be reached but is not included because the computation time is too long with respect to the duration of the thesis.

4.4.1 Symmetries

Introduction to symmetries

To overcome memory limitation due to the large size of Hilbert space, we will use the symmetry of the system. Indeed, if we consider N_S symmetries, the size of the Hilbert space (N_H) can be reduced up to N_H/N_S.

To study the Hamiltonian, we use a cluster with a finite size that we repeat to simulate an infinite lattice using translations via the Periodic Boundary Conditions (See Section A.1.2). Formally, the two-dimensional plane becomes a torus. A cluster has different symmetries, discrete (invariance by translation, rotation, reflexion, and so on and so forth) or continuous, such as SU(2), symmetries which can be in real space or in the phase state. In the following, we will focus on the discrete symmetries of the system. Using symmetries for the Hamiltonian means applying a unitary transformation such that the Hamiltonian becomes block-diagonal. Each of these blocks is associated to a symmetry sector (introduced short after) and forms a subspace that can be diagonalized independently. From this last statement, we understand first that it reduces the size of Hilbert space.

Using symmetries can be also very interesting in case of a degenerate state when using the Lanczos algorithm which does not work with degenerate ground state. Each of these ground states can be in a different block making a block to diagonalize non degenerate.

There are three symmetry categories in our system: Translations, point group symmetries and, at zero-field, an orbital symmetry between the orbitals $\uparrow$ and $\downarrow$. The orbital $\uparrow$ is represented numerically by 1 and the orbital $\downarrow$ by a 0. With this symmetry, we can toggle all orbitals $\uparrow$ in $\downarrow$ and vice versa, e.g. $|\uparrow\downarrow\rangle = |\downarrow\uparrow\rangle$. We will not focus too much on this symmetry because it corresponds to only one line in the phase diagram.

Let us introduce some definitions.

Applying a symmetry S on a vector $|r\rangle$ gives another vector

$$S|r\rangle = \omega|S(r)\rangle,$$

where $|S(r)\rangle$ is the image of $|r\rangle$ by the symmetry S.

There exists a integer n such that $S^n = I$, so applying n times the symmetry S let a vector invariant

$$S^n|r\rangle = \omega^n|r\rangle,$$

and thus $\omega^n = 1$ giving $\omega = e^{i2\pi\frac{k}{n}}$, the nth root of unit, with k an integer. The quantity ω is the character of the symmetry S.

We introduce the inverse of the symmetry S^{-1}, defined as

$$S^{-1}S = SS^{-1} = I$$

or, equivalently,

$$S^{-1}|S(r)\rangle = \omega^*|r\rangle.$$

It implies that $\omega\omega^* = 1$.

For an ensemble of symmetries, a set of characters is called a symmetry sector.

Let us take the symmetry "up/down" $|\uparrow\downarrow\rangle = \omega_{\text{up/down}}|\downarrow\uparrow\rangle$. If $\omega_{\text{up/down}} = 1$, the wavefunction is symmetric and if $\omega_{\text{up/down}} = -1$, the wavefunction is antisymmetric.

We work in an orthogonal basis, which simplifies the problem.

Translations

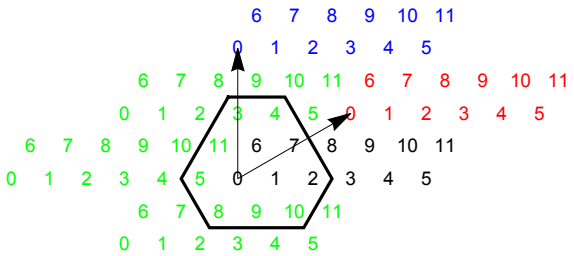

Fig. 4.8 Diamond representation of a 12 sites cluster. The two arrows are the translation vectors of the cluster. The position of each cluster is a linear combination of these two arrows with integer coefficients. We label the sites of the cluster from 0 to 11. The black numbers are the first cluster, red and blue numbers are the clusters translated by the arrows. Green numbers are other clusters repeated with the combination of the two arrows.

The translation symmetry decreases the most the size of the basis because the number of translation symmetries is the number of sites. We construct them with two operators, T_1 and T_2, where T_i shifts all the orbital states by one unit vector along the direction of the lattice $\vec{u}_i$. Figure 4.9 is a graphical representation of this operator. Because of the periodic boundary conditions, which are represented by the Figure 4.8 for a cluster of 12 sites, $T_1^{L_x} = I$ and $T_2^{L_y} = I$. Also, $T_{-1} = T_1^{L_x-1}$ and $T_{-2} = T_2^{L_y-1}$. These two operators commute

$$T_1T_2 = T_2T_1.$$

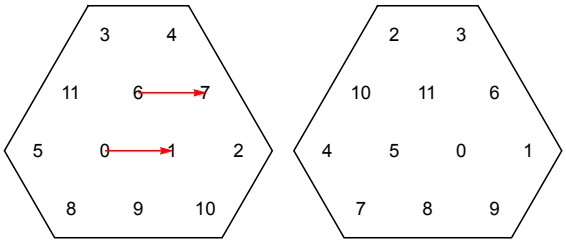

Fig. 4.9 The translation symmetry T_1 shifts all the sites by the vector $\vec{u}_1$, represented here by the red arrow on the right. On the left panel, the corresponding indexes after shifting all the sites.

The last statement means we can always apply these two symmetries at the same time. It is not the case, for example, with the point group symmetry, as we shall see later. The set of all translation symmetry operators is

$$T(x,y) = T_1^x T_2^y,$$

with $x \in [0, L_x[$ and $y \in [0, L_y[$. This set is not unique; we just take an arbitrary choice of all the nonequivalent symmetry operators. The character of the generic translation operator $T(x,y)$ is $\omega_k = e^{i\vec{k}.\vec{r}(x,y)}$, with $\vec{r}(x,y) = x\vec{u}_1 + y\vec{u}_2$ and $\vec{k}$, the momentum, is the ensemble of the points in the Brillouin Zone. Each representation of the translation symmetry corresponds to a $\vec{k}$ point in the First Brillouin Zone.

Point Group Symmetries

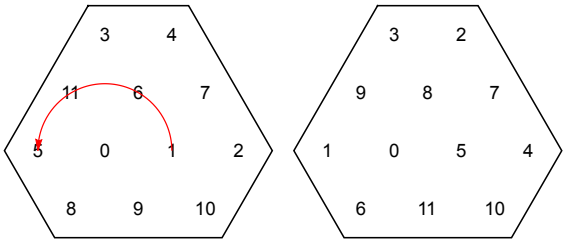

Fig. 4.10 The rotation symmetry C_2 rotates all the sites by an angle π around the point (0,0), represented here by the red arrow on the right. On the left panel, the corresponding indexes after rotating all the sites.

A Point Group is a group of symmetries that keep at least one point fixed, typically, rotations (one fixed point) and reflexions (fixed line). The point group symmetry of the effective Hamiltonian is C_2. It means that it is invariant by I and a rotation of π. A Graphical representation of C_2 is depicted in Figure 4.10. The table of irreducible

Table 4.1 Character table of C_2.

	I	C_2
A	1	1
B	1	-1

Table 4.2 Character table of C_{6v} for representations of dimension one.

	I	$2C_6$	$2C_3$	C_2	$3\sigma_v$	$3\sigma_d$
A_1	1	1	1	1	1	1
A_2	1	1	1	1	-1	-1
B_1	1	-1	1	-1	1	-1
B_2	1	-1	1	-1	-1	1

representations of this point group is listed Table 4.1. For $\theta = \pi/4$, because all three directions are equivalent, i.e. the Hamiltonian is isotropic, we can apply I, rotate the system by $\pi/3$ ($2C_6$, $2C_3$, C_2) and perform mirror symmetries with axes along the directions of the lattice ($3\sigma_v$) and the bisectors of the directions of the lattice ($3\sigma_d$). The set of all these operations is the point group C_{6v} and the irreducible one-dimensional representations are listed Table 4.2. The representations of higher dimensions are out of the scope of this thesis.

A cluster is invariant by rotation if the norm of the vector for the Periodic Boundary Conditions are equal. It is the case for both the regular and the tilted cluster, but not for the rectangular cluster (See Section A.1.2).

Compatible symmetries

All symmetries cannot be applied at the same time. Both the Hamiltonian and the cluster has to be compatible with all considered symmetries. We define two compatible symmetries if they commute. An example of two compatible symmetries is given Figure 4.11 for the application of two translations, T_1 and T_2, on a nine sites cluster. We see that these operators commute because the result does not depend on the order of the application. However, it is not the case for the translations with the point group. we can show it with an example by taking the same nine-site cluster, but for the translation T_1 and the rotation R_π. If we apply $T_1 R_\pi$ and we compare with $R_\pi T_1$, the news indexes does not match (see Fig. 4.12). Here, R_θ is the operator that rotates the system by π around the point (0,0).

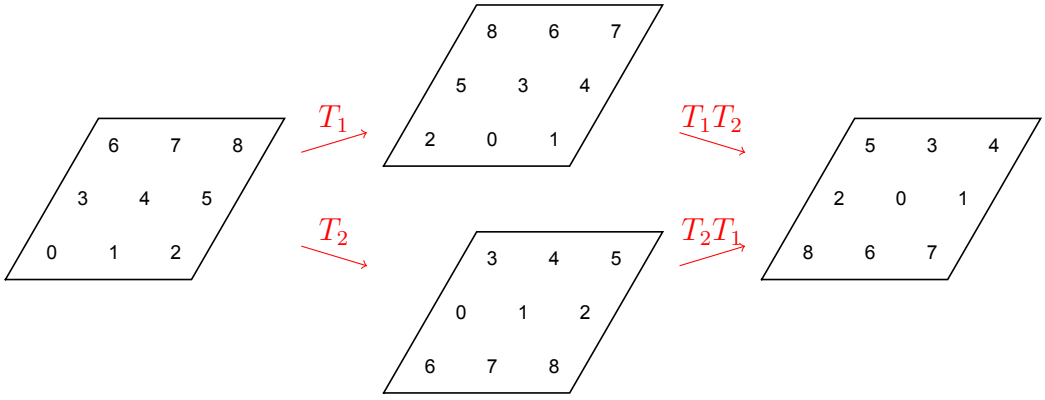

Fig. 4.11 On the left, a cluster of nine sites for the triangular lattice with periodic boundary conditions. Each site has a label from 0 to 8. The application of the symmetry operator T_1, respectively T_2, gives the cluster on the center top, respectively bottom. The application of T_2, respectively T_1, on the latter gives the same cluster in both cases.

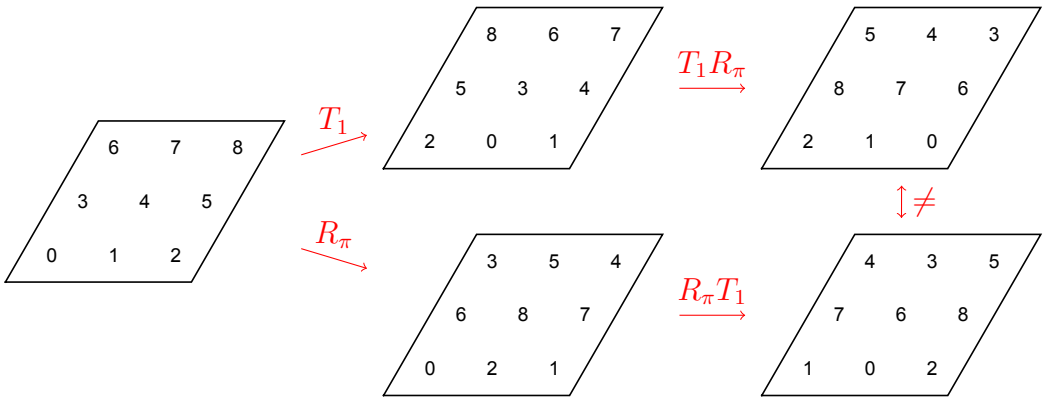

Fig. 4.12 On the left, a cluster of nine sites for the triangular lattice with periodic boundary conditions. Each site has a label from 0 to 8. The application of the symmetry operator T_1, respectively R_π, gives the cluster on the center top, respectively bottom. The application of R_π, respectively T_1, on the latter gives different clusters: on the right top, respectively bottom.

Although translations and point group symmetries do not commute in general, they are compatible in certain symmetry sectors. Relevant example for the following are the Γ-point and the M-points which are compatible with C_2, whereas K-points are not.

Representatives

In practice, we do not compute explicitly the unitary transformation to make the Hamiltonian block-diagonal. Indeed, the matrix representation of such operator is too large and it is what we try to avoid when we use the symmetries. We want to work with the smallest possible basis. This basis, which is of course a subspace of the Hilbert space, is an ensemble of states called representatives $|r_i\rangle$. A representative is a state from which one can build other states by applying symmetries. Applying all symmetries on each representative gives the whole ensemble of states of the Hilbert space.

Each set of representatives for which the Hamiltonian is block-diagonal form a subspace called symmetry sector.

Let us look at a simple example where we consider a block diagonal matrix A

$$A = \begin{pmatrix} \overbrace{\begin{pmatrix} \mathrm{U} & -t \\ -t & \mathrm{U} \end{pmatrix}}^{\omega_1} & \begin{matrix} 0 & 0 & 0 \\ 0 & 0 & 0 \end{matrix} \\ \begin{matrix} 0 & 0 \\ 0 & 0 \\ 0 & 0 \end{matrix} & \overbrace{\begin{pmatrix} \mathrm{U} & -t & -t \\ -t & U & -t \\ -t & -t & \mathrm{U} \end{pmatrix}}^{\omega_2} \end{pmatrix}$$

The two blocks are boxed and correspond to a symmetry sector $\omega_{i=1,2}$ with ω_1 has two representatives and ω_2 has three representatives. These blocks can be diagonalized independently.

In practice, our Hamiltonian is not obviously block diagonal. To build the basis of a symmetry sector, in other words, the ensemble of representatives of a symmetry sector, we take all possible states not connected by any operation of symmetry.

The eigenvector $|\psi\rangle$ of the new eigenvalue problem, i.e. finding the eigenstates of the Hamiltonian in the subspace of a symmetry sector, is

$$|\psi\rangle = \sum_{i=1}^{N_r} \alpha_i |r_i\rangle,$$

with N_r the number of representatives $|r_i\rangle$, and the wavefunction of the ground state of the Hamiltonian $|\tilde{\psi}\rangle$ is connected to this eigenvector by symmetry operations

$$|\tilde{\psi}\rangle = \frac{1}{N_S}\sum_{p=1}^{N_S} S_p|\psi\rangle,$$

with $\{S_p\}$ the ensemble of the N_S symmetries. Finally, the wavefunction as a function of the representatives and the symmetries is

$$|\tilde{\psi}\rangle = \frac{1}{N_S}\sum_{p=1}^{N_S} S_p \sum_{i=1}^{N_r} \alpha_i|r_i\rangle. \tag{4.15}$$

It gives a basis which can be larger than the actual basis of the symmetry sector. Indeed, the previous operation does not involve the symmetry sector, only the symmetry operations. We need to do a reduction.

Reduction

The reduction is an operation which gives the actual basis of a symmetry sector. If the sum of all characters associated to an operation of symmetry that let a representative invariant is zero, then this state is not a representative associated to the symmetry sector. Let us rewrite Equation 4.15

$$|\tilde{\psi}\rangle = \frac{1}{N_S}\sum_{i=1}^{N_r} \alpha_i \left(\left(\sum_{q\in E_i} \omega_q \right) |r_i\rangle + \sum_{q\in \bar{E}_i} \omega_q |S_q(r_i)\rangle \right),$$

with E_i the ensemble of symmetries that let $|r_i\rangle$ unchanged and $\bar{E}_i$ are the other symmetries. If $\sum_{q\in E_i}\omega_q = 0$, the representatives associated to the indexes $q \in E_i$ do not contribute to the first term of the wavefunction. One can show they also do not contribute to the second part.

The reduction has been done properly if the sum over all symmetry sectors of the dimensions of each basis associated to the symmetry sector times its dimension is equal to the size of the Hilbert space.

Now, we have the smallest basis possible by application of symmetries. Its size will depend on the symmetry sector, and we don't know *a priori* in which symmetry sector is the ground state, and for all set of symmetries, there is a symmetry sector with all the characters equal to one, so there is no reduction. When we apply the Hamiltonian to a ket, it projects the ket in the whole Hilbert space. Then, we apply the symmetry

operators to find the representatives. It is possible that the representative does not exist if it has been removed by the reduction. In this case, this resulting ket does not contribute.

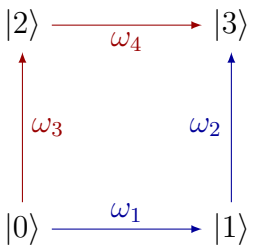

Fig. 4.13 Two paths connect $|0\rangle$ and $|3\rangle$. The blue path goes through $|1\rangle$, such as $|3\rangle = S_1 S_2 |0\rangle = \omega_1 \omega_2 |0\rangle$. The red path goes through $|2\rangle$, such as $|3\rangle = S_3 S_4 |0\rangle = \omega_3 \omega_4 |0\rangle$.

There is a physical meaning to this operation of reduction. Each symmetry operation on a vector gives different character. Let us consider two vectors $|0\rangle$ and $|3\rangle$ connected by symmetries. If the path taken to go from one vector to another is not unique (See Fig. 4.13 for an example), these vectors will not contribute if the character associated to the symmetry operations, $\omega_1\omega_2$ and $\omega_3\omega_4$ in this example, are different. It means that the link between a vector and its representative does not depend on the symmetries applied, but only on the symmetry sector. Notice that there is always a symmetry sector where all paths are equivalent ($\omega_i = 1$), so all representatives contribute.

Observables

Let us see how to write a matrix element of an operator $\hat{O}$ which commutes with the Hamiltonian $o_{ij} = \langle \tilde{r}_i | \hat{O} | \tilde{r}_j \rangle$ where $\{|\tilde{r}_i\}$ is the orthonormal basis in the whole Hilbert space. The basis of the representatives is orthonormal $\langle r_i | r_j \rangle = \delta_{ij}$. The operator $\hat{O}$ project the ket $|r_j\rangle$ in the whole Hilbert space

$$\hat{O}|r_j\rangle = \sum_k \alpha_k |k\rangle.$$

To each of the resulting states $|k\rangle$ corresponds a representative $|r_{l(k)}\rangle$ by application of the symmetry $S_{m(k)}$. Only the representatives equal to $|r_i\rangle$ will contribute to the matrix element, so, such that $l(k) = i$. A matrix element is

$$o_{ij} = \langle \tilde{r}_i | \hat{O} | \tilde{r}_j \rangle = \sum_{k \text{ such that } l(k)=i} \alpha_k \omega_{m(k)} \sqrt{\frac{\deg(p_i)}{\deg(p_j)}},$$

where $\deg(p_i)$ is the degeneracy of the representative p_i.

The degeneracy of the representative $|r_i\rangle$ is

$$\deg(r_i) = \sum_{q \in E_i} \omega_q,$$

with E_i the ensemble of the indexes q of the symmetry S_q which let the representative unchanged, ie $S_q|r_i\rangle = \omega_q|S_q(r_i)\rangle = \omega_q|r_i\rangle$. One can show that it does not depend on the symmetry sector and it is equal to the number of symmetries that let the representative unchanged, $\mathrm{Card}(E_i)$. If the latter is null in a symmetry sector, it corresponds to a representative which has been eliminated during the reduction process.

4.4.2 Quantum phase diagrams

Methods

In this section, we briefly describe the tools that we used to build the phase diagrams.

To identify the transition lines, we used the continuity of the first two derivative of the energy and to characterize the phases, we will use the same order parameters than for the classical approach, presented in Section 4.3.3, with few differences. We compute correlations of observables rather than their mean-values; the form of the structure factor remains unchanged, however the polarization along one direction $\alpha = x, y, z$ and the chirality change. The former becomes the correlation with respect to an arbitrary reference (here the first site)

$$\tau^\alpha = \frac{1}{4N_s} \sum_{i=1}^{N_s} \langle \sigma_1^\alpha \sigma_i^\alpha \rangle, \tag{4.16}$$

in practice we use only the z component, and the latter will not be computed in this dissertation because of lack of time, as it requires even for the scalar chirality, to code a large number of operators: 36 terms of product of 6 nondiagonal operators. Beside, the computation time for such quantity can be large. Real space correlations are computed to draw snapshots of the different phases, using the following formula

$$\tau_i = \frac{1}{4N_s} \sum_{i=1}^{N_s} \left(2\langle \sigma_1^+ \sigma_i^- \rangle + 2\langle \sigma_1^- \sigma_i^+ \rangle + \langle \sigma_1^z \sigma_i^z \rangle \right). \tag{4.17}$$

We used two methods to obtain the results in exact diagonalizations, the brute-force diagonalization and Lanczos algorithms.

The brute-force exact diagonalization consists to diagonalize the complete Hamiltonian. It gives access to the whole spectra and all associated eigenvectors. However it suffers of large computing limitations in terms of time and memory consumption that make it suitable for small systems only, the 12-site and 16-site clusters in this work.

Lanczos algorithm is an iterative method to compute the lowest eigenvalue and its eigenvector if it is not degenerate. We will not present the details of the method here, it is presented in many books (see for example Vernay thesis in Ref. [139]), nevertheless let us introduce the idea. The matrix, here the Hamiltonian H, is transformed into a tridiagonal matrix T. *How is that convenient?* A routine to diagonalize a tridiagonal matrix, such as QR algorithm implemented in dstevx function of LAPACK [104], needs only two vectors: the diagonal and the subdiagonal elements of the matrix. These same vectors will be used to store the eigenvalue (energy of the ground state) and its eigenvector (ground state), so no extra memory is used for the output, making the memory consumption linear with the Hilbert space size, whereas as the memory consumption for brute-force diagonaliation is the Hilbert space size square. It allows us to reach a cluster of 24 sites.

As we mentioned before, exact diagonalization methods can return the eigenvector only for non-degenerate ground state. Indeed, in case of degeneracy, the algorithm will pick a random vector that belongs to the subspace of the ground state. Using the symmetries helps because the degeneracy can be lifted, but *how do we know that the ground state is not degenerate?* Short answer, we do not. A symmetry breaking on the average of quantities that are not explicitly broken in the Hamiltonian, e.g. $\langle \tau_i^x \rangle = \langle \tau_j^x \rangle$ whereas $\langle \tau_i^z \rangle$ and $\langle \tau_j^z \rangle$ can be different in this case or $\langle n_i \rangle = \langle n_j \rangle$ in multiorbital extended Hubbard model that we studied in the previous chapter, is an evidence of degeneracy in the symmetry sector. Although the smooth variation of quantities, such as order parameters and correlations, as a function of a parameter is a clue that the ground state is not degenerate, it is not enough to show the absence of degeneracy.

We obtained these results by developing a C++ program using fast linear algebra libraries, Armadillo [114], openBLAS [111, 112] and LAPACK [104]. We used translations and C_2 symmetries and diagonalized the Hamiltonian in each symmetry sector, that allows us to easily parallelize the code.

Zero-field results

The spectra as a function of θ for clusters of 12 and 16 sites are shown Figure 4.14 at zero-field (left and right, respectively). Some gaps are closing as a function of θ

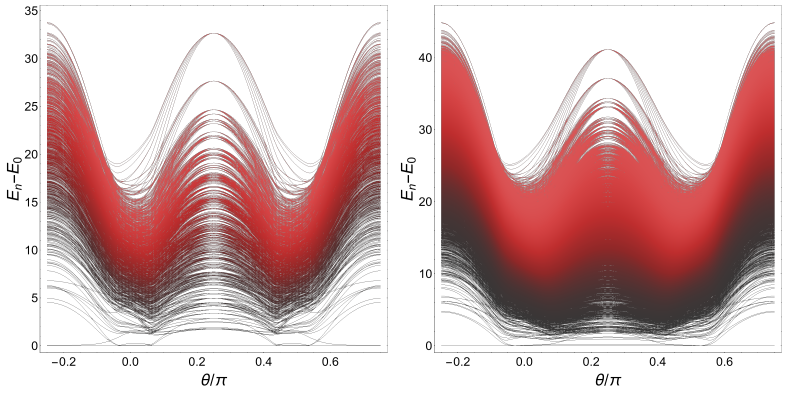

Fig. 4.14 The Spectrum, obtained with brute-force exact diagonalizations, minus the energy of the ground state $E_n - E_0$ for clusters of (left) 12 and (right) 16 sites as a function of θ over one period at $h = 0$.

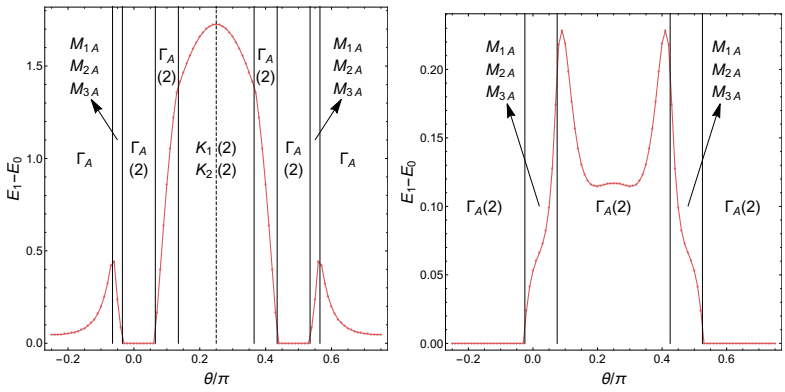

Fig. 4.15 Energy of the second eigenvalue minus the energy of the ground state $E_1 - E_0$ for clusters of (left) 12 and (right) 16 sites as a function of θ over one period. Labels correspond to the symmetry sector associated to the eigenvalue with the degeneracy between brackets. For the 12-site cluster, equivalent symmetry sector to $K_1\,(2)$ and $K_2\,(2)$ are $A\,(2)$ and $B\,(2)$. On the same cluster, for $\theta = \pi/4$ (dashed line), the degeneracy of the two symmetry sectors is 3.

while others remain open. One can notice the qualitative differences between the two sizes that are related to a size effect. We start by focusing on the gap between the first two energies shown on Figure 4.15. A closing or opening gap is a precursor of a phase transition at the thermodynamic limit. On the 12-site cluster, one can identify 5 areas but only 3 one the 16-site cluster.

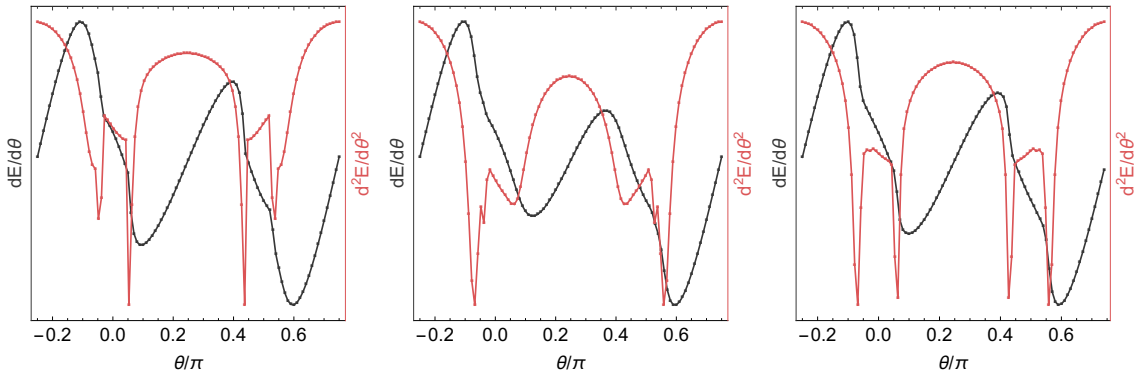

(a) 12 sites (b) 16 sites (c) 24 sites

Fig. 4.16 First (black) and second (red) derivative of energy of the ground state of clusters of 12 (left), 16 (middle) and 24 (right) sites as a function of θ over one period.

These areas can be seen also by looking at the continuity of the first and second derivatives, as shown in Figure 4.16 for 12-, 16- and 24-site clusters. We clearly see the second derivative (red line) is discontinuous where the gaps close or open. Although the derivative in Figure 4.16 are with respect to θ, one can mention that the same transitions are found for the derivative with respect to h. A cluster of 16 sites is not a good candidate to describe the physics of triangular lattice because the number of sites is not a multiple of 3. Both 12-site and 24-site cluster give similar results. In both cases we have four phase transitions and we recover the same number of transition than with the classical approach, even though the values are different because of correlations and size effects.

Close to the isotropic case for the 12-site cluster, on the left panel of Figure 4.15, the second eigenvalue is either on K-points if translation symmetries are used or in symmetry sector A and B when using C_2 point group symmetry. The energy of the second eigenvalue is twofold degenerate for each symmetry sector, excepted on the SU(2) point ($\theta = \pi/4$) where they are threefold degenerate. Away from this area, the second eigenvalue belongs to $\vec{k}$-points, Γ- and M-points, that can be diagonalized with C_2 point group symmetry. Notice that the second eigenvalue on the 16-site cluster is instead in the Γ_A symmetry sector because the K-points are absent of the Brillouin zone for this cluster.

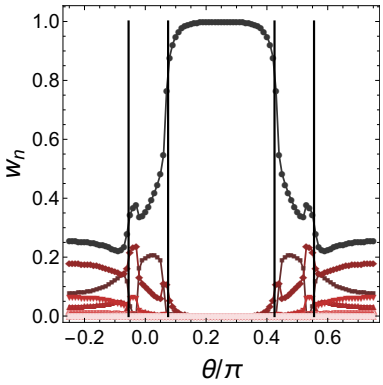

Fig. 4.17 Orbital sector w_n at zero-field as defined in Equation 4.18 as a function of θ. From darker to lighter red, n increases from 0 to 24.

τ^z, the orbital sector, is a good quantum number in our model only at $\theta = \pi/4$, the case where the Hamiltonian commutes with τ^z, $\left[H^{\text{eff}}, \tau^z\right]$. This information can be of relevance to reach larger cluster size because one can reduce the Hilbert space size by considering only states to given orbital sectors, e.g. $\tau^z = 0$ at zero-field. Here, we wonder if considering τ^z as a good quantum number for $\theta \neq \pi/4$ is a good approximation by looking at the mixing of the orbital sectors. Figure 4.17 represents, for the 24-site cluster at $h = 0$, the weight of each orbital sector $\tau^z = |n_\uparrow - n_\downarrow|/2$

$$w_{\tau^z} = \langle n_{\uparrow=N_s/2-\tau^z} \rangle + \langle n_{\uparrow=N_s/2+\tau^z} \rangle. \tag{4.18}$$

It shows which vectors of the Hilbert space contribute to the wavefunction. We can see that almost all the weight is on states of $\tau^z = 0$ close to the isotropic case so diagonalizing the Hamiltonian in the orbital sector $\tau^z = 0$ can be a good approximation. For intermediate values of θ, $\tau^z = 1, 2, 3$ also contribute to the wavefunction. It is then possible to constraint the Hilbert space to states in orbital sectors $\tau^z = 0, 1, 2, 3$. At $\theta = 3\pi/4$ all orbital sectors have no neglected weight, so no approximation on the Hilbert space can be done. The fact that the wavefunction has weight on orbital sectors $n \neq 0$, on the contrary to the Heisenberg model, comes from the additional $\sigma_i^\pm \sigma_j^\pm$ and $\sigma_i^\pm \sigma_j^z$ terms that couple different orbital sectors. Notice that this value as a meaning only at low field because it breaks the $\uparrow/\downarrow$ symmetry so one can look at $w_{n_\uparrow} = \langle n_{\uparrow=N_s/2-n} \rangle$; $w_{n_\downarrow} = \langle n_{\downarrow=N_s/2-n} \rangle$ being always zero for h positive.

Results in presence of a pseudo-magnetic field

The phase diagrams obtained in the presence of a pseudo-magnetic field for 12 and 24 sites are displayed in Figure 4.18 where we also draw the classical phase diagram for

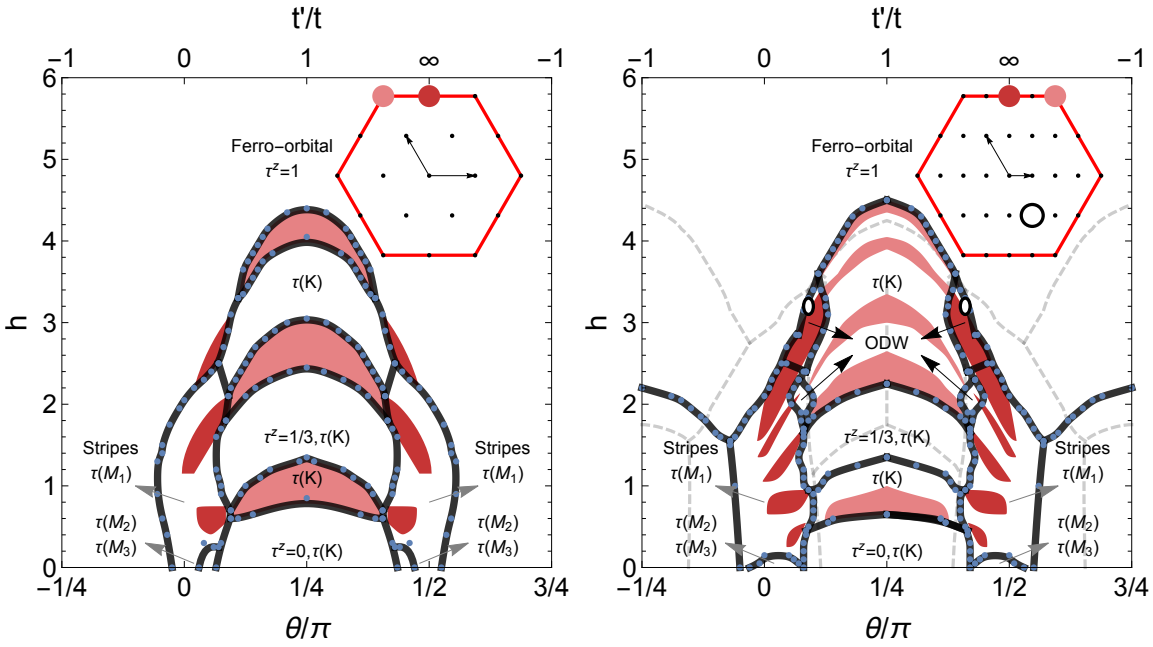

Fig. 4.18 Quantum phase diagram for a cluster of 12 (left) and 24 (right) sites. We draw the classical phase diagram (light grey dashed lines) for convenient comparison. Colored areas represent the different symmetry sectors of the wavefunction: white for the Γ-point, light red of the K-point, dark red for the M_1-point and the two small oval white areas with dark edges at the transition between ODW and ferro-orbital are at the $K/2$-points, as shown on the Brillouin zone in inset.

convenient comparison. In addition to transition lines and labels of the phases, the colored areas represent the different symmetry sectors of the wavefunction: white for the Γ-point, light red of the K-point, dark red for the M_1-point and the two small oval white areas with dark edges at the transition between ODW and ferro-orbital are at the $K/2$-points, as shown on the Brillouin zone in inset. We do not display the 16-site phase diagram as the K-points, important for this system, are absent of the Brillouin zone.

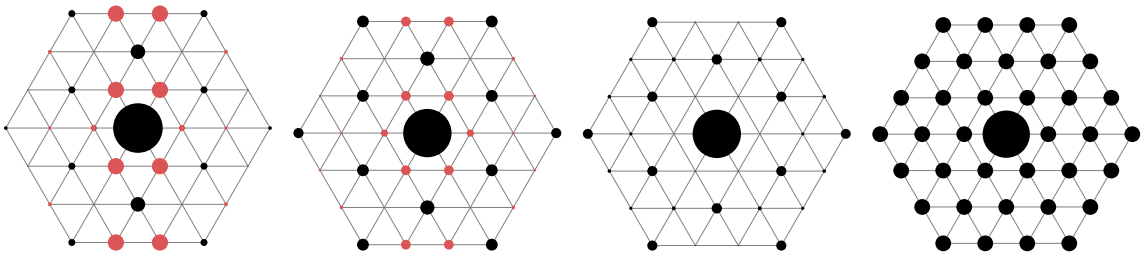

Fig. 4.19 Correlations in real space from Equation 4.17. for some phases at $\theta = \pi/4$: zero-orbital polarization ($h = 0$), 1/3-plateau ($h = 1.5$), V configuration ($h = 3$) and ferro-orbital ($h = 5$) The radius of the disks in proportional to the correlations. Black and red correspond to correlations and anti-correlations, respectively.

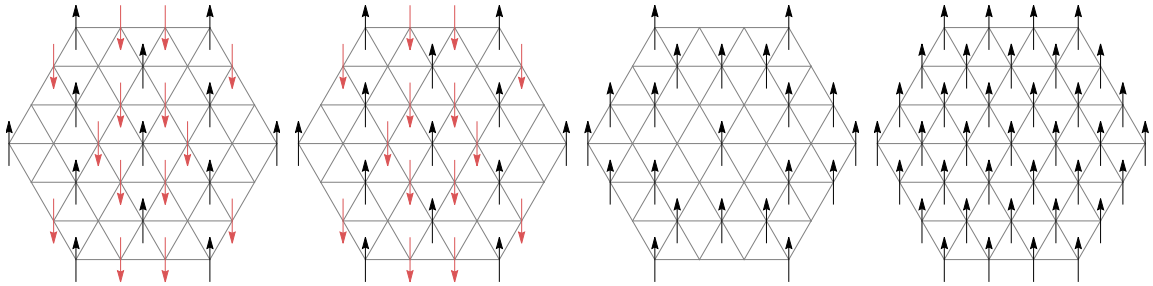

Fig. 4.20 Sketches of the phases at $\theta = \pi/4$ built using the sign of correlations in real space from Figure 4.19. From left to right: zero-orbital polarization ($h = 0$), 1/3-plateau ($h = 1.5$), V configuration ($h = 3$) and ferro-orbital ($h = 5$). No arrow means an absence of correlations. Notice that the zero-orbital polarization and the 1/3-plateau phases have the same representation.

Around $\theta = \pi/4$, there are five phases. Real space correlations of some of them are shown in Figure 4.19 with a corresponding sketch in Figure 4.20. At low field, a plateau of zero-orbital polarization is found. While increasing the field, the τ^z increases almost continuously. We associate this phase to the Y configuration because of the finite orbital polarization and the anti-correlation in real space with the nearest neighbors. Small intermediate plateaus appear with discontinuous second derivative of

the energy. The number of these transitions increases with the size of the cluster so can be associated to size effect and are ignored. Then the 1/3-plateau is reached, before going the same process where the orbital polarization increases almost continuously but with a positive correlation with nearest neighbor so we associate this phase to the V configuration. All these phases have a finite correlation on K-points. There is also a small correlation on the M-points coming from the fact that the 24-site cluster does not respect rotation symmetry. It is worth to notice that, because the 12-site cluster respect the rotation symmetry, no M-points peaks appears in this area for the 12-site cluster. Finally, at high field, the ferro-orbital phase ($\tau^z = 1$) is reached.

The small plateaus of orbital magnetization, zero-polarization and the 1/3-plateau, come from the fact that, at $\theta = \pi/4$, τ^z is a good quantum number, i.e. τ^z commutes with the Hamiltonian. Although it is not true as soon as $\theta \neq \pi/4$, it is effectively the case in this area of the phase diagram, as shown at zero-field.

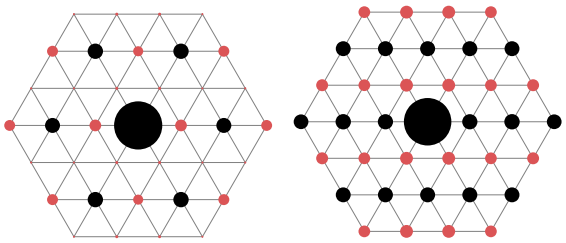

Fig. 4.21 Correlations in real space for phases at $\theta = \pi/2$ in the M-points area: M_2 M_3 ($h = 0$), and M_1 stripes ($h = 1$), The radius of the disks in proportional to the correlations. Black and red correspond to correlations and anti-correlations, respectively.

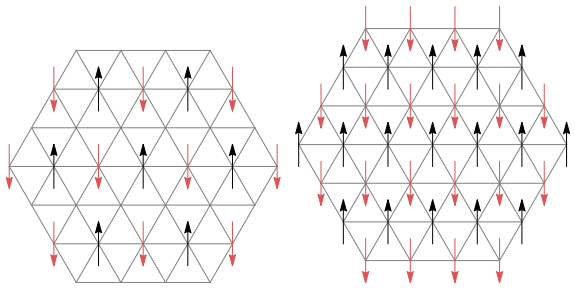

Fig. 4.22 Sketches of the phases at $\theta = \pi/2$ in the M-points area: built using the sign of correlations in real space from Figure 4.21: M_2 M_3 ($h = 0$), and M_1 stripes ($h = 1$). No arrow means an absence of correlations.

Away from the isotropic case $\theta = \pi/4$, around $\theta = \pi/2$, two stripe orders are stabilized. Their real space correlations are shown in Figure 4.21 with a corresponding

sketch in Figure 4.22. A stripe order on the M_1-point is stabilized at intermediate field, whereas peaks in correlations are on M_2- and M_3-points at low field.

While increasing h, one can see that the ground state changes of symmetry sector, alternating from Γ to K or M_1. However, in analogy with the different plateaus of orbital polarization, we associated these changes in symmetry sector to size effects as their number increases with the size.

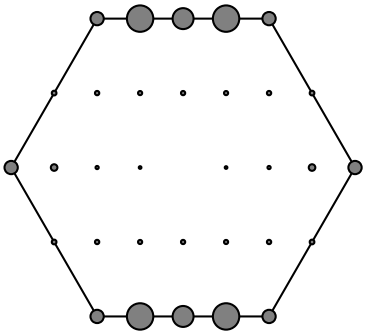

Fig. 4.23 Correlations in the Brillouin zone of the ODW phase obtained in exact diagonalization for $\theta = 0.38\pi$ and $h = 3.2$. The radius of the disks in proportional to the correlations. The Γ-point is not displayed.

Between the M-points and K-points areas, there is an orbital density wave (ODW) with a peak in correlations at the only point available between K and M_1. The weight continuously goes from K- to M_1-points with a maximum on middle. The 24-site cluster is the first size that allow such state; the 12-site cluster does not have any point on the ΓM lines therefore no orbital density wave is found. In addition, there is no set of parameter for which the ground state is in $K/2$-point symmetry sector. Nevertheless, one can see that there is already a small area where the ground state is in the M-point symmetry sector at the crossing of K-, M- and Γ-points region. It is a precursor to the orbital density wave.

Finally, far from the isotropic case, around $\theta = 3\pi/4$, there are peaks in correlations, excepted on the Γ-point in the correlations. No plateau has been found before orbital saturation at high field. The absence of transition while increasing the field for the 12-site cluster is associated to a size effect. Although the first two derivatives of the energy are continuous for the 12-site cluster, the behavior of the second derivative already present evidence of the transition that appears when increasing the size of the system.

To conclude, let us compare the results from classical and quantum approaches. The transition lines in the phase diagrams are in good agreement in both approaches; we can divide the phase diagram in five parts: (i) high field with the ferro-orbital

phase, (ii) close to the isotropic case for the Heisenberg limit, (iii) the M area with stripe orders, (iv) the orbital density wave between the two latter, and (v) far from the isotropic case with correlations on the Γ-point only. The shapes of the transition lines are also similar between the classical and quantum approach. Moreover, as already pointed out, we can identify the lower and upper parts of the threefold orbital order ($\tau(K) \neq 0$) to the Y and V configurations, respectively, by looking at the real space snapshots of the correlations.

There are, however, few differences. First, the presence of two plateaus, zero-polarization and the 1/3-plateau, only possible with quantum fluctuations. This 1/3-plateau has been already observed [135]. Second, another stripe phase is found with the quantum approach in the M area. Finally, far away from the isotropic case, only one transition is found with the quantum approach while increasing the field whereas two transitions are found classically.

Further comparison requires more investigation, such as computing the $\langle \tau^y \tau^y \rangle$ correlation to properly identify the phase around $\theta = 3\pi/4$.

4.5 Conclusion

Using perturbation theory in the Mott regime, we derived a generic Heisenberg-like effective Hamiltonian for the e_g-orbitals that makes possible analogy with spins (Equation 4.8) with a known limiting case which is the standard Heisenberg model. We study this model for the triangular lattice with two approaches to build the phase diagrams, both classical and quantum, and unravel rich phase diagrams including new phases without threefold orders away from the isotropic case.

Using the strength of symmetries and the Lanczos algorithm, we were able to diagonalize the Hamiltonian for a 24-site cluster.

The known phases from the Heisenberg model have an extension as a function of the anisotropy of the band structure of e_g-orbitals and are therefore not limited to the isotropic case. However, new phases are stabilized due to the influence of the kinetic effects on these orbitals: stripe orders, phases with finite polarization along a given direction and orbital density waves. These phases have been found with the two methods that we used, i.e. the classical approach and the exact diagonalizations.

Although the two approaches are consistent with each other, let us remind the few main differences: (i) no plateau can be found classically (ii) there are two different phases with quantum approach in the M area of the phase diagram, and (iii) a phase at intermediate field around $\theta = 3\pi/4$ is found classically.

We have also identified some open questions that remain to be addressed for this model, is there a chiral order with quantum approach and how it behaves, what is the origin the stripe orders, is the phase at $\theta = 3\pi/4$ found with exact diagonalization as a correlation on the y component, how strong are the size effects with exact diagonalization.

Chapter 5

Conclusion of the dissertation

During this dissertation, we studied theoretically how the frustration of Coulomb interactions and multiorbital kinetic effects on triangular lattices can lead to a variety of original electronic phases. Our studies are motivated by the physical properties of an important class of layered compounds with d-bands, such as layered transition-metal dichalcogenides and $2H$-$AgNiO_2$ that we presented in the first chapter. These systems exhibit various charge orders, for example the $\sqrt{13} \times \sqrt{13}$ star of David pattern for the former and the metallic threefold charge order for the latter. Due to the geometry of the underlying atomic lattices, a form of frustration arises from the degeneracy of the classical ground state where all local constrains can not be satisfied. Such frustration can lead to novel phases when the quantum fluctuations are included. We introduced the charge frustration in analogy of magnetic frustration and indeed found a specific phase that comes from this effect, the pinball liquid. This is a peculiar state where an insulating threefold charge order (pins) is surrounded by a metallic honeycomb lattice with itinerant electrons (balls), first predicted in the context of quarter-filled organic compounds but never observed experimentally in these compounds.

In order to address the multiorbital problem, we derived a generic multiorbital extended Hubbard model in the second chapter. We refined this generic model to the specific case of e_g-orbitals with one electron per site in average and we assumed a strong local Coulomb interaction U leading to a spinless model. A brief review of the single-band spinful Hubbard model at half filling, its extended version and the multiorbital spinfull extended Hubbard model revealed the richness of Hubbard models and the expected states in the limiting cases that correspond to these models.

In the third chapter, we performed a complete study of the model, as a function of all microscopic parameters, focusing on the interplay between frustrated electron-electron interactions and multiorbital effects for the specific case of e_g-orbitals. To this end, we

used different means: noninteracting limit, electrostatic considerations, unrestricted Hartree-Fock approach and exact diagonalization. We started with the tight-binding approach revealing a Lifshitz transition, the presence of Van Hove singularities and different topologies of the Fermi surface. Using electrostatic considerations, we built an effective model to sketch a preliminary phase diagram. Such a simple model already unravels a phase diagram with the main features of the full phase diagrams found with unrestricted Hartree-Fock and exact diagonalization, but does not give all informations about orbital and charge orders, or what can happen for intermediate values of interactions. We performed an unrestricted Hartree-Fock approach, a method without assumption on the symmetry breaking, suitable for large unit-cell phases and revealed a number of charge-ordered and orbital-order phases. More than ten phases have been found, including (i) a homogeneous metal at weak interactions, (ii) a Mott state at strong local Coulomb interactions, (iii) a pinball charge order at strong local and non-local interactions, (iv) a charge order without orbital order at strong short-range Coulomb interactions and weak local interactions and (v) a pinball liquid phase at intermediate values of interactions. Apart from the phases known for the single-band spinful extended Hubbard model, equivalent to the spinless extended Hubbard model for e_g-orbital, such as the homogeneous metal and the different orders at low short-range Coulomb interactions or at strong Coulomb interactions, we found (i) the pinball liquid and its dual, the inverse pinball liquid, that is experimentally observed in $AgNiO_2$, (ii) the large unit-cell $\sqrt{12} \times \sqrt{12}$ insulating charge order, which could be related to the $\sqrt{13} \times \sqrt{13}$ star of David charge order in dichalcogenide compound $1T$-TaS_2, and (iii) incommensurate charge and orbital density waves. These phases are purely stabilized by the quantum fluctuations as we were able to show in two ways. First, they are discriminated from other classically degenerate orders by the band structure. Second, although these phases are stabilized in a broad range of parameters, varying the band structure induces transitions to other classically degenerate orders, e.g. pinball liquid and $\sqrt{12} \times \sqrt{12}$ charge order to their dual and PCO_I to PCO_{III}. One of the achievements of this thesis has been to find large unit-cell orders with a model with only nearest neighbors interactions which was made possible by the use of the unrestricted Hartree-Fock method in real space, in contrast to previous work where the constraints did not allow all symmetry breakings [95, 93]. In order to validate these results, we performed a comparison with exact diagonalization results, obtained by Arnaud Ralko, which confirmed qualitatively the unrestricted Hartree-Fock phase diagram.

We noticed that the unrestricted Hartree-Fock method failed to capture the physical properties for parameters of the band structure t'/t far from the isotropic case, especially at $t' = -t$, for strong local Coulomb interactions. To address this problem, we choose to develop a perturbation theory starting from the Mott state and derived a Heisenberg-like Hamiltonian. In addition to the terms corresponding to the Heisenberg model, the specific form of the hopping integrals of e_g-orbitals induces an anisotropy and extra terms $\sigma_i^{\pm}\sigma_j^{\pm}$ and $\sigma_i^{z}\sigma_j^{\pm}$, that couples all orbital sectors. In order to investigate the model, we included a chemical potential to favor one orbital having the form of a magnetic field. We studied the new model with both a classical approach and exact diagonalization in the quantum case, using the strength of symmetries and Lanczos algorithm to reach a 24-site cluster size. Beside the standard phases obtained close to the isotropic case where the effective Hamiltonian reduces to the Heisenberg model, namely the Y and V configurations, the 1/3-plateau and the ferro-orbital phase, we found phases with a finite τ^y component and finite τ^x and τ^z components far from the isotropic case. For intermediate values of the band structure anisotropy t'/t, stripe orders are also stabilized with structure factor either on M_2- and M_3-points at low pseudo-magnetic field and M_1-point at stronger pseudo-magnetic field. At intermediate values of the pseudo-magnetic field h, an orbital density wave is stabilized between the threefold orbital orders of the isotropic case and stripe orders. Phase diagrams from classical approach and exact diagonalization qualitatively agree with two noteworthy differences (i) the 1/3 plateau can not be stabilized classically and (ii) although we could not completely characterize the phase far from the isotropic case in exact diagonalization, the extra transition found classically does not seem to subsist in exact diagonalization according to the continuity of the derivatives of the energy.

The interplay between multiorbital kinetic effects, frustration and electron-electron interactions on the triangular lattice can stabilize various phases and tuning them can induce transitions. Whereas we were able to understand many of the key features of the phases diagrams for both the multiorbital spinless extended Hubbard model and the Heisenberg-like Hamiltonian, some points still need to enlightened. For the multiorbital spinless extended Hubbard model: What is the role of the filling? What is the mechanism for the transition from the inverse pinball liquid to the $\sqrt{12} \times \sqrt{12}$ charge order? For the Heisenberg-like Hamiltonian: Is there a chiral order? What is the origin of the stripe order? is the phase found far away from the isotropic case found with exact diagonalization as a correlation on the y component? What are the size effects in exact diagonalization? The purpose of future work will be to answer these open questions.

References

[1] Antoine Georges. Strongly correlated electron materials: Dynamical mean-field theory and electronic structure. *AIP Conference Proceedings*, 715(1):3–74, 2004.

[2] Antoine Georges, Luca de' Medici, and Jernej Mravlje. Strong correlations from hund's coupling. *Annual Review of Condensed Matter Physics*, 4(1):137–178, 2013.

[3] Touru Yamauchi, Masahiko Isobe, and Yutaka Ueda. Charge order and superconductivity in vanadium oxides. *Solid State Sciences*, 7(7):874 – 881, 2005. Selected articles from the 4th International Conference on Inorganic MaterialsAntwerp, Belgium 19-21 Septembre 2004.

[4] J. Chang, E. Blackburn, A. T. Holmes, N. B. Christensen, J. Larsen, J. Mesot, Ruixing Liang, D. A. Bonn, W. N. Hardy, A. Watenphul, M. v. Zimmermann, E. M. Forgan, and S. M. Hayden. Direct observation of competition between superconductivity and charge density wave order in yba2cu3o6.67. *Nat Phys*, 8(12):871–876, Dec 2012.

[5] Eduardo H. da Silva Neto, Pegor Aynajian, Alex Frano, Riccardo Comin, Enrico Schierle, Eugen Weschke, András Gyenis, Jinsheng Wen, John Schneeloch, Zhijun Xu, Shimpei Ono, Genda Gu, Mathieu Le Tacon, and Ali Yazdani. Ubiquitous interplay between charge ordering and high-temperature superconductivity in cuprates. *Science*, 343(6169):393–396, 2014.

[6] Yuxuan Wang and Andrey Chubukov. Charge-density-wave order with momentum $(2q, 0)$ and $(0, 2q)$ within the spin-fermion model: Continuous and discrete symmetry breaking, preemptive composite order, and relation to pseudogap in hole-doped cuprates. *Phys. Rev. B*, 90:035149, Jul 2014.

[7] Yuxuan Wang, Debanjan Chowdhury, and Andrey V. Chubukov. Fluctuating charge order in the cuprates: Spatial anisotropy and feedback from superconductivity. *Phys. Rev. B*, 92:161103, Oct 2015.

[8] D. JÉROME. The physics of organic superconductors. *Science*, 252(5012):1509–1514, 1991.

[9] E. Wawrzyńska, R. Coldea, E. M. Wheeler, I. I. Mazin, M. D. Johannes, T. Sörgel, M. Jansen, R. M. Ibberson, and P. G. Radaelli. Orbital degeneracy removed by charge order in triangular antiferromagnet agnio$_2$. *Phys. Rev. Lett.*, 99:157204, Oct 2007.

[10] E. Wawrzyńska, R. Coldea, E. M. Wheeler, T. Sörgel, M. Jansen, R. M. Ibberson, P. G. Radaelli, and M. M. Koza. Charge disproportionation and collinear magnetic order in the frustrated triangular antiferromagnet agnio$_2$. *Phys. Rev. B*, 77:094439, Mar 2008.

[11] G. L. Pascut, R. Coldea, P. G. Radaelli, A. Bombardi, G. Beutier, I. I. Mazin, M. D. Johannes, and M. Jansen. Direct observation of charge order in triangular metallic agnio$_2$ by single-crystal resonant x-ray scattering. *Phys. Rev. Lett.*, 106:157206, Apr 2011.

[12] B. E. Brown. The crystal structures of NbT_2 and $TaTe_2$. *Acta Crystallographica*, 20(2):264–267, Feb 1966.

[13] K. C. Woo, F. C. Brown, W. L. McMillan, R. J. Miller, M. J. Schaffman, and M. P. Sears. Superlattice formation in titanium diselenide. *Phys. Rev. B*, 14:3242–3247, Oct 1976.

[14] J. A. Holy, K. C. Woo, M. V. Klein, and F. C. Brown. Raman and infrared studies of superlattice formation in tise$_2$. *Phys. Rev. B*, 16:3628–3637, Oct 1977.

[15] L. Perfetti, P. A. Loukakos, M. Lisowski, U. Bovensiepen, H. Berger, S. Biermann, P. S. Cornaglia, A. Georges, and M. Wolf. Time evolution of the electronic structure of 1t-tas$_2$ through the insulator-metal transition. *Phys. Rev. Lett.*, 97:067402, Aug 2006.

[16] John A. Wilson. Questions concerning the form taken by the charge-density wave and the accompanying periodic-structural distortions in $2h - Tase_2$, and closely related materials. *Phys. Rev. B*, 17:3880–3898, May 1978.

[17] Corsin Battaglia, Hervé Cercellier, Florian Clerc, Laurent Despont, Michael Gunnar Garnier, Christian Koitzsch, Philipp Aebi, Helmuth Berger, László Forró, and Claudia Ambrosch-Draxl. Fermi-surface-induced lattice distortion in Nbte$_2$. *Phys. Rev. B*, 72:195114, Nov 2005.

[18] K. Rossnagel and N. V. Smith. Spin-orbit coupling in the band structure of reconstructed 1t-tas$_2$. *Phys. Rev. B*, 73:073106, Feb 2006.

[19] E. Morosan, H. W. Zandbergen, B. S. Dennis, J. W. G. Bos, Y. Onose, T. Klimczuk, A. P. Ramirez, N. P. Ong, and R. J. Cava. Superconductivity in cuxtise2. *Nat Phys*, 2(8):544–550, Aug 2006.

[20] B. Sipos, A. F. Kusmartseva, A. Akrap, H. Berger, L. Forro, and E. Tutis. From mott state to superconductivity in 1t-tas2. *Nat Mater*, 7(12):960–965, Dec 2008.

[21] R. Ang, Y. Miyata, E. Ieki, K. Nakayama, T. Sato, Y. Liu, W. J. Lu, Y. P. Sun, and T. Takahashi. Superconductivity and bandwidth-controlled mott metal-insulator transition in 1t-tas$_{2-x}$se$_x$. *Phys. Rev. B*, 88:115145, Sep 2013.

[22] K Rossnagel. On the origin of charge-density waves in select layered transition-metal dichalcogenides. *Journal of Physics: Condensed Matter*, 23(21):213001, 2011.

[23] Yijun Yu, Fangyuan Yang, Xiu Fang Lu, Ya Jun Yan, ChoYong-Heum, Liguo Ma, Xiaohai Niu, Sejoong Kim, Young-Woo Son, Donglai Feng, Shiyan Li, Sang-Wook Cheong, Xian Hui Chen, and Yuanbo Zhang. Gate-tunable phase transitions in thin flakes of 1t-tas$_2$. *Nat Nano*, 10(3):270–276, Mar 2015. Article.

[24] Yoichi Kamihara, Takumi Watanabe, Masahiro Hirano, and Hideo Hosono. Iron-based layered superconductor la[o1-xfx]feas (x = 0.05-0.12) with tc = 26 k. *Journal of the American Chemical Society*, 130(11):3296–3297, 2008. PMID: 18293989.

[25] Ren Zhi-An, Lu Wei, Yang Jie, Yi Wei, Shen Xiao-Li, Zheng-Cai, Che Guang-Can, Dong Xiao-Li, Sun Li-Ling, Zhou Fang, and Zhao Zhong-Xian. Superconductivity at 55 k in iron-based f-doped layered quaternary compound sm[o 1- x f x] feas. *Chinese Physics Letters*, 25(6):2215, 2008.

[26] K Haule and G Kotliar. Coherence-incoherence crossover in the normal state of iron oxypnictides and importance of hund's rule coupling. *New Journal of Physics*, 11(2):025021, 2009.

[27] Naoya Arakawa. Orbital-cooperative spin fluctuation and orbital-dependent transport in ruthenates. *Phys. Rev. B*, 90:245103, Dec 2014.

[28] M. Yi, Z.-K. Liu, Y. Zhang, R. Yu, J.-X. Zhu, J. J. Lee, R. G. Moore, F. T. Schmitt, W. Li, S. C. Riggs, J.-H. Chu, B. Lv, J. Hu, M. Hashimoto, S.-K. Mo, Z. Hussain, Z. Q. Mao, C. W. Chu, I. R. Fisher, Q. Si, Z.-X. Shen, and D. H. Lu. Observation of universal strong orbital-dependent correlation effects in iron chalcogenides. *Nat Commun*, 6, Jul 2015. Article.

[29] Jun Kondo. Resistance minimum in dilute magnetic alloys. *Progress of Theoretical Physics*, 32(1):37–49, 1964.

[30] A. Menth, E. Buehler, and T. H. Geballe. Magnetic and semiconducting properties of smb$_6$. *Phys. Rev. Lett.*, 22:295–297, Feb 1969.

[31] Chisa Hotta and Nobuo Furukawa. Strong coupling theory of the spinless charges on triangular lattices: Possible formation of a gapless charge-ordered liquid. *Phys. Rev. B*, 74:193107, Nov 2006.

[32] Mitake Miyazaki, Chisa Hotta, Shin Miyahara, Keisuke Matsuda, and Nobuo Furukawa. Variational monte carlo study of a spinless fermion t-v model on a triangular lattice: Formation of a pinball liquid. *Journal of the Physical Society of Japan*, 78(1):014707, 2009.

[33] L. Cano-Cortés, A. Ralko, C. Février, J. Merino, and S. Fratini. Geometrical frustration effects on charge-driven quantum phase transitions. *Phys. Rev. B*, 84:155115, Oct 2011.

[34] C. Février, S. Fratini, and A. Ralko. Multiorbital kinetic effects on charge ordering of frustrated electrons on the triangular lattice. *Phys. Rev. B*, 91:245111, Jun 2015.

[35] Arnaud Ralko, Jaime Merino, and Simone Fratini. Pinball liquid phase from hund's coupling in frustrated transition-metal oxides. *Phys. Rev. B*, 91:165139, Apr 2015.

[36] H. Freimuth, H. Wiechert, H. P. Schildberg, and H. J. Lauter. Neutron-diffraction study of the commensurate-incommensurate phase transition of deuterium monolayers physisorbed on graphite. *Phys. Rev. B*, 42:587–603, Jul 1990.

[37] E. Wigner. On the interaction of electrons in metals. *Phys. Rev.*, 46:1002–1011, Dec 1934.

[38] Jaime Merino, Arnaud Ralko, and Simone Fratini. Emergent heavy fermion behavior at the wigner-mott transition. *Phys. Rev. Lett.*, 111:126403, Sep 2013.

[39] J. S. Olafsen and J. S. Urbach. Clustering, order, and collapse in a driven granular monolayer. *Phys. Rev. Lett.*, 81:4369–4372, Nov 1998.

[40] A D Yoffe. Layer compounds. *Annual Review of Materials Science*, 3(1):147–170, 1973.

[41] Kazunori Takada, Hiroya Sakurai, Eiji Takayama-Muromachi, Fujio Izumi, Ruben A. Dilanian, and Takayoshi Sasaki. Superconductivity in two-dimensional coo2 layers. *Nature*, 422(6927):53–55, Mar 2003.

[42] N. P. Ong and R. J. Cava. Electronic frustration on a triangular lattice. *Science*, 305(5680):52–53, 2004.

[43] M.-H. Julien, C. de Vaulx, H. Mayaffre, C. Berthier, M. Horvatić, V. Simonet, J. Wooldridge, G. Balakrishnan, M. R. Lees, D. P. Chen, C. T. Lin, and P. Lejay. Electronic texture of the thermoelectric oxide $na_{0.75}coo_2$. *Phys. Rev. Lett.*, 100:096405, Mar 2008.

[44] H. Alloul, I. R. Mukhamedshin, A. V. Dooglav, Ya. V. Dmitriev, V.-C. Ciomaga, L. Pinsard-Gaudart, and G. Collin. ^{23}na nmr study of sodium order in na_xcoo_2 with 22 k néel temperature. *Phys. Rev. B*, 85:134433, Apr 2012.

[45] H. Yoshida, Y. Muraoka, T. Sörgel, M. Jansen, and Z. Hiroi. Spin-$\frac{1}{2}$ triangular lattice with orbital degeneracy in a metallic oxide ag_2Nio_2. *Phys. Rev. B*, 73:020408, Jan 2006.

[46] Hatsumi Mori, Shoji Tanaka, and Takehiko Mori. Systematic study of the electronic state in θ-type bedt-ttf organic conductors by changing the electronic correlation. *Phys. Rev. B*, 57:12023–12029, May 1998.

[47] Chisa Hotta. Classification of quasi-two dimensional organic conductors based on a new minimal model. *Journal of the Physical Society of Japan*, 72(4):840–853, 2003.

[48] Hitoshi Seo, Jaime Merino, Hideo Yoshioka, and Masao Ogata. Theoretical aspects of charge ordering in molecular conductors. *Journal of the Physical Society of Japan*, 75(5):051009, 2006.

[49] Takehiko Mori and Tadashi Kawamoto. Organic conductors-from fundamentals to nonlinear conductivity. *Annu. Rep. Prog. Chem., Sect. C: Phys. Chem.*, 103:134–172, 2007.

[50] S. Aminpirooz, L. Becker, H. Rossner, A. Schellenberger, and E. Holub-Krappe. The structure of sodium intercalated 1t and 2h polytypes of tas2: a photoemission and {SEXAFS} study. *Surface Science*, 331-333, Part A:501 – 505, 1995. Proceedings of the 14th European Conference on Surface Science.

[51] F Clerc, C Battaglia, H Cercellier, C Monney, H Berger, L Despont, M G Garnier, and P Aebi. Fermi surface of layered compounds and bulk charge density wave systems. *Journal of Physics: Condensed Matter*, 19(35):355002, 2007.

[52] C. Riekel. Structure refinement of tise2 by neutron diffraction. *Journal of Solid State Chemistry*, 17(4):389 – 392, 1976.

[53] G. Li, W. Z. Hu, D. Qian, D. Hsieh, M. Z. Hasan, E. Morosan, R. J. Cava, and N. L. Wang. Semimetal-to-semimetal charge density wave transition in $1t$-tise$_2$. *Phys. Rev. Lett.*, 99:027404, Jul 2007.

[54] Timo Sörgel and Martin Jansen. Ag3Ni2O4-a new stage-2 intercalation compound of 2h-AgNiO2 and physical properties of 2h-agnio2 above ambient temperature. *Journal of Solid State Chemistry*, 180(1):8 – 15, 2007.

[55] Timo Sörgel. *Interkalationsverbindungen von Übergangsmetallschichtoxiden und -telluriden und elektrochemische Festkörpersynthesen.* PhD thesis, Max-Planck-Institut für Festkörperforschung, 2006.

[56] E. M. Wheeler, R. Coldea, E. Wawrzyńska, T. Sörgel, M. Jansen, M. M. Koza, J. Taylor, P. Adroguer, and N. Shannon. Spin dynamics of the frustrated easy-axis triangular antiferromagnet $2h$-agnio$_2$ explored by inelastic neutron scattering. *Phys. Rev. B*, 79:104421, Mar 2009.

[57] P. N. Bityutskii, , and V. I. Khitrova. Investigation of AgNiO2 and CoHO2 crystal structures. *Journal of Structural Chemistry*, 9(6):921–925, 1969.

[58] A. I. Coldea, L. Seabra, A. McCollam, A. Carrington, L. Malone, A. F. Bangura, D. Vignolles, P. G. van Rhee, R. D. McDonald, T. Sörgel, M. Jansen, N. Shannon, and R. Coldea. Cascade of field-induced magnetic transitions in a frustrated antiferromagnetic metal. *Phys. Rev. B*, 90:020401, Jul 2014.

[59] Hiroshi Uchigaito, Masafumi Udagawa, and Yukitoshi Motome. Mean-field study of charge, spin, and orbital orderings in triangular-lattice compounds anio2 (a = na, li, ag). *Journal of the Physical Society of Japan*, 80(4):044705, 2011.

[60] R. Cortés, A. Tejeda, J. Lobo-Checa, C. Didiot, B. Kierren, D. Malterre, J. Merino, F. Flores, E. G. Michel, and A. Mascaraque. Competing charge ordering and mott phases in a correlated sn/ge(111) two-dimensional triangular lattice. *Phys. Rev. B*, 88:125113, Sep 2013.

[61] J. Slezák, P. Mutombo, and V. Cháb. Stm study of a pb/si(111) interface at room and low temperatures. *Phys. Rev. B*, 60:13328–13330, Nov 1999.

[62] G. H. Wannier. Antiferromagnetism. the triangular ising net. *Phys. Rev.*, 79:357–364, Jul 1950.

[63] Toulouse. Theory of the frustration effect in spin glasses : I. *Communications on Physics*, 2:115, 1977.

[64] J Vannimenus and G Toulouse. Theory of the frustration effect. ii. ising spins on a square lattice. *Journal of Physics C: Solid State Physics*, 10(18):L537, 1977.

[65] Chanchal K. Majumdar and Dipan K. Ghosh. On next-nearest-neighbor interaction in linear chain. i. *Journal of Mathematical Physics*, 10(8):1388–1398, 1969.

[66] C K Majumdar. Antiferromagnetic model with known ground state. *Journal of Physics C: Solid State Physics*, 3(4):911, 1970.

[67] Elbio Dagotto and Adriana Moreo. Phase diagram of the frustrated spin-1/2 heisenberg antiferromagnet in 2 dimensions. *Phys. Rev. Lett.*, 63:2148–2151, Nov 1989.

[68] Masato Kaneko and Masao Ogata. Mean-field study of charge order with long periodicity in θ-(bedt-ttf)2x. *Journal of the Physical Society of Japan*, 75(1):014710, 2006.

[69] L. Cano-Cortés, J. Merino, and S. Fratini. Quantum critical behavior of electrons at the edge of charge order. *Phys. Rev. Lett.*, 105:036405, Jul 2010.

[70] Luca F. Tocchio, Claudius Gros, Xue-Feng Zhang, and Sebastian Eggert. Phase diagram of the triangular extended hubbard model. *Phys. Rev. Lett.*, 113:246405, Dec 2014.

[71] Masafumi Udagawa and Yukitoshi Motome. Charge ordering and coexistence of charge fluctuations in quasi-two-dimensional organic conductors θ-(BEDT-TTF)$_2x$. *Phys. Rev. Lett.*, 98:206405, May 2007.

[72] Kazuhiko Kuroki. Theoretical aspects of charge correlations in θ-(bedt-ttf) 2 x. *Science and Technology of Advanced Materials*, 10(2):024312, 2009.

[73] Samiyeh Mahmoudian, Louk Rademaker, Arnaud Ralko, Simone Fratini, and Vladimir Dobrosavljević. Glassy dynamics in geometrically frustrated coulomb liquids without disorder. *Phys. Rev. Lett.*, 115:025701, Jul 2015.

[74] H. A. Jahn and E. Teller. Stability of polyatomic molecules in degenerate electronic states. i. orbital degeneracy. *Proceedings of the Royal Society of London A: Mathematical, Physical and Engineering Sciences*, 161(905):220–235, 1937.

[75] Hiroaki Onishi and Takashi Hotta. Stripe charge ordering in triangular-lattice systems. *AIP Conference Proceedings*, 850(1):1075–1076, 2006.

[76] F. Vernay, K. Penc, P. Fazekas, and F. Mila. Orbital degeneracy as a source of frustration in linio$_2$. *Phys. Rev. B*, 70:014428, Jul 2004.

[77] J.-S. Kang, S. S. Lee, G. Kim, H. J. Lee, H. K. Song, Y. J. Shin, S. W. Han, C. Hwang, M. C. Jung, H. J. Shin, B. H. Kim, S. K. Kwon, and B. I. Min. Valence and spin states in delafossite $AgNio_2$ and the frustrated jahn-teller system $aNio_2$ ($a = \mathrm{Li}, \mathrm{Na}$). *Phys. Rev. B*, 76:195122, Nov 2007.

[78] J. Hubbard. Electron correlations in narrow energy bands. *Proceedings of the Royal Society of London A: Mathematical, Physical and Engineering Sciences*, 276(1365):238–257, 1963.

[79] C. Castellani, C. R. Natoli, and J. Ranninger. Magnetic structure of v_2o_3 in the insulating phase. *Phys. Rev. B*, 18:4945–4966, Nov 1978.

[80] Shiro Sakai. *Theoretical study of multi-orbital correlated electron systems with Hund's coupling*. PhD thesis, University of Tokyo, 12 2006.

[81] G. Jackeli and G. Khaliullin. Spin, orbital, and charge order at the interface between correlated oxides. *Phys. Rev. Lett.*, 101:216804, Nov 2008.

[82] Junjiro Kanamori. Electron correlation and ferromagnetism of transition metals. *Progress of Theoretical Physics*, 30(3):275–289, 1963.

[83] I. I. Mazin, D. I. Khomskii, R. Lengsdorf, J. A. Alonso, W. G. Marshall, R. M. Ibberson, A. Podlesnyak, M. J. Martínez-Lope, and M. M. Abd-Elmeguid. Charge ordering as alternative to jahn-teller distortion. *Phys. Rev. Lett.*, 98:176406, Apr 2007.

[84] H. R. Krishnamurthy, C. Jayaprakash, Sanjoy Sarker, and Wolfgang Wenzel. Mott-hubbard metal-insulator transition in nonbipartite lattices. *Phys. Rev. Lett.*, 64:950–953, Feb 1990.

[85] C. Jayaprakash, H. R. Krishnamurthy, S. Sarker, and W. Wenzel. Metal-insulator transition in the hubbard model on a triangular lattice. *EPL (Europhysics Letters)*, 15(6):625, 1991.

[86] C J Gazza, A E Trumper, and H A Ceccatto. The triangular-lattice hubbard model: a frustrated highly correlated electron system. *Journal of Physics: Condensed Matter*, 6(41):L625, 1994.

[87] A Feiguin, C J Gazza, A E Trumper, and H A Ceccatto. The hubbard model on the triangular lattice: a slave-boson study. *Journal of Physics: Condensed Matter*, 9(4):L27, 1997.

[88] Massimo Capone, Luca Capriotti, Federico Becca, and Sergio Caprara. Mott metal-insulator transition in the half-filled hubbard model on the triangular lattice. *Phys. Rev. B*, 63:085104, Feb 2001.

[89] Feng Lu, Wei-Hua Wang, and Liang-Jian Zou. Metal-insulator transition in the half-filling two-orbital hubbard model on the triangular lattice. *Phys. Rev. B*, 77:125117, Mar 2008.

[90] Luca F. Tocchio, Hélène Feldner, Federico Becca, Roser Valentí, and Claudius Gros. Spin-liquid versus spiral-order phases in the anisotropic triangular lattice. *Phys. Rev. B*, 87:035143, Jan 2013.

[91] A. Yamada. Magnetic properties and mott transition in the hubbard model on the anisotropic triangular lattice. *Phys. Rev. B*, 89:195108, May 2014.

[92] B. Davoudi, S. R. Hassan, and A.-M. S. Tremblay. Competition between charge and spin order in the $t-U-V$ extended hubbard model on the triangular lattice. *Phys. Rev. B*, 77:214408, Jun 2008.

[93] Jiming Gao and Jiaxiang Wang. The metal-insulator transition in the half-filled extended hubbard model on a triangular lattice. *Journal of Physics: Condensed Matter*, 21(48):485702, 2009.

[94] S. R. Hassan and L. de' Medici. Slave spins away from half filling: Cluster mean-field theory of the hubbard and extended hubbard models. *Phys. Rev. B*, 81:035106, Jan 2010.

[95] Giuseppe Santoro, Sandro Scandolo, and Erio Tosatti. Charge-density waves and surface mott insulators for adlayer structures on semiconductors: Extended hubbard modeling. *Phys. Rev. B*, 59:1891–1901, Jan 1999.

[96] Luca de' Medici, Jernej Mravlje, and Antoine Georges. Janus-faced influence of hund's rule coupling in strongly correlated materials. *Phys. Rev. Lett.*, 107:256401, Dec 2011.

[97] Luca de' Medici. Hund's coupling and its key role in tuning multiorbital correlations. *Phys. Rev. B*, 83:205112, May 2011.

[98] W. Koshibae and S. Maekawa. Electronic state of a coo_2 layer with hexagonal structure: A kagomé lattice structure in a triangular lattice. *Phys. Rev. Lett.*, 91:257003, Dec 2003.

[99] H. Alloul, I. R. Mukhamedshin, T. A. Platova, and A. V. Dooglav. Na ordering imprints a metallic kagomé lattice onto the co planes of na 2/3 coo 2. *EPL (Europhysics Letters)*, 85(4):47006, 2009.

[100] J. C. Slater and G. F. Koster. Simplified lcao method for the periodic potential problem. *Phys. Rev.*, 94:1498–1524, Jun 1954.

[101] Norio Kawakami, Tatsuya Usuki, and Ayao Okiji. Thermodynamic properties of the one-dimensional hubbard model. *Physics Letters A*, 137(6):287 – 290, 1989.

[102] C. C. J. Roothaan. New developments in molecular orbital theory. *Rev. Mod. Phys.*, 23:69–89, Apr 1951.

[103] David R. Penn. Stability theory of the magnetic phases for a simple model of the transition metals. *Phys. Rev.*, 142:350–365, Feb 1966.

[104] E. Anderson, Z. Bai, C. Bischof, S. Blackford, J. Demmel, J. Dongarra, J. Du Croz, A. Greenbaum, S. Hammarling, A. McKenney, and D. Sorensen. *LAPACK Users' Guide*. Society for Industrial and Applied Mathematics, Philadelphia, PA, third edition, 1999.

[105] R. Clint Whaley and Antoine Petitet. Minimizing development and maintenance costs in supporting persistently optimized BLAS. *Software: Practice and Experience*, 35(2):101–121, February 2005. `http://www.cs.utsa.edu/~whaley/papers/spercw04.ps`.

[106] R. Clint Whaley, Antoine Petitet, and Jack J. Dongarra. Automated empirical optimization of software and the ATLAS project. *Parallel Computing*, 27(1–2):3–35, 2001. Also available as University of Tennessee LAPACK Working Note #147, UT-CS-00-448, 2000 (`www.netlib.org/lapack/lawns/lawn147.ps`).

[107] R. Clint Whaley and Jack Dongarra. Automatically Tuned Linear Algebra Software. In *Ninth SIAM Conference on Parallel Processing for Scientific Computing*, 1999. CD-ROM Proceedings.

[108] R. Clint Whaley and Jack Dongarra. Automatically tuned linear algebra software. In *SuperComputing 1998: High Performance Networking and Computing*, 1998. CD-ROM Proceedings. **Winner, best paper in the systems category.** URL: `http://www.cs.utsa.edu/~whaley/papers/atlas_sc98.ps`.

[109] R. Clint Whaley and Jack Dongarra. Automatically Tuned Linear Algebra Software. Technical Report UT-CS-97-366, University of Tennessee, December 1997. URL : `http://www.netlib.org/lapack/lawns/lawn131.ps`.

[110] See homepage for details. Atlas homepage. http://math-atlas.sourceforge.net/.

[111] Zhang Xianyi, Wang Qian, and Zhang Yunquan. Model-driven level 3 blas performance optimization on loongson 3a processor. In *Parallel and Distributed Systems (ICPADS), 2012 IEEE 18th International Conference on*, pages 684–691, Dec 2012.

[112] Qian Wang, Xianyi Zhang, Yunquan Zhang, and Qing Yi. Augem: Automatically generate high performance dense linear algebra kernels on x86 cpus. In *Proceedings of the International Conference on High Performance Computing, Networking, Storage and Analysis*, SC '13, pages 25:1–25:12, New York, NY, USA, 2013. ACM.

[113] Gaël Guennebaud, Benoît Jacob, et al. Eigen v3. http://eigen.tuxfamily.org, 2010.

[114] Conrad Sanderson. Armadillo: An Open Source C++ Linear Algebra Library for Fast Prototyping and Computationally Intensive Experiments. Technical report, NICTA, September 2010.

[115] Karim Ferhat and Arnaud Ralko. Phase diagram of the $\frac{1}{3}$-filled extended hubbard model on the kagome lattice. *Phys. Rev. B*, 89:155141, Apr 2014.

[116] C. G. Broyden. A class of methods for solving nonlinear simultaneous equations. *Math. Comp.*, 19:577–593, Oct 1965.

[117] J. Merino, A. Greco, N. Drichko, and M. Dressel. Non-fermi liquid behavior in nearly charge ordered layered metals. *Phys. Rev. Lett.*, 96:216402, Jun 2006.

[118] P. Pisarski, R. M. Jones, and R. J. Gooding. Application of a multisite mean-field theory to the disordered bose-hubbard model. *Phys. Rev. A*, 83:053608, May 2011.

[119] M. M. Qazilbash, J. J. Hamlin, R. E. Baumbach, Lijun Zhang, D. J. Singh, M. B. Maple, and D. N. Basov. Electronic correlations in the iron pnictides. *Nat Phys*, 5(9):647–650, Sep 2009.

[120] Ken Kanada, Tsutomu Watanabe, Seiichiro Onari, and Yukio Tanaka. Exact diagonalization study on the extended hubbard model in an anisotropic triangular lattice. *Journal of Physics and Chemistry of Solids*, 69(12):3334 – 3336, 2008. {SNS2007} Spectroscopies in Novel Superconductors '07.

[121] Frank Pollmann, Krishanu Roychowdhury, Chisa Hotta, and Karlo Penc. Interplay of charge and spin fluctuations of strongly interacting electrons on the kagome lattice. *Phys. Rev. B*, 90:035118, Jul 2014.

[122] Alaska Subedi, Oleg E. Peil, and Antoine Georges. Low-energy description of the metal-insulator transition in the rare-earth nickelates. *Phys. Rev. B*, 91:075128, Feb 2015.

[123] Peyman Sahebsara and David Sénéchal. Hubbard model on the triangular lattice: Spiral order and spin liquid. *Phys. Rev. Lett.*, 100:136402, Mar 2008.

[124] Adolfo G. Grushin, Eduardo V. Castro, Alberto Cortijo, Fernando de Juan, María A. H. Vozmediano, and Belén Valenzuela. Charge instabilities and topological phases in the extended hubbard model on the honeycomb lattice with enlarged unit cell. *Phys. Rev. B*, 87:085136, Feb 2013.

[125] A. Demourgues, F. Weill, B. Darriet, A. Wattiaux, J.C. Grenier, P. Gravereau, and M. Pouchard. Additional oxygen ordering in la2nio4.25 (la8ni4o17): Ii. structural features. *Journal of Solid State Chemistry*, 106(2):330 – 338, 1993.

[126] Takashi Mizokawa. Metal-insulator transitions: Orbital control. *Nat Phys*, 9(10):612–613, Oct 2013. News and Views.

[127] Charles L. Cleveland and Rodrigo Medina A. Obtaining a heisenberg hamiltonian from the hubbard model. *American Journal of Physics*, 44(1):44–46, 1976.

[128] Davis E. King. Dlib-ml: A machine learning toolkit. *Journal of Machine Learning Research*, 10:1755–1758, 2009.

[129] X. G. Wen, Frank Wilczek, and A. Zee. Chiral spin states and superconductivity. *Phys. Rev. B*, 39:11413–11423, Jun 1989.

[130] T. Inami, M. Nishiyama, S. Maegawa, and Y. Oka. Magnetic structure of the *kagomé* lattice antiferromagnet potassium jarosite $kfe_3(OH)_6(SO_4)_2$. *Phys. Rev. B*, 61:12181–12186, May 2000.

[131] Seiji Miyashita. Magnetic properties of ising-like heisenberg antiferromagnets on the triangular lattice. *Journal of the Physical Society of Japan*, 55(10):3605–3617, 1986.

[132] Luis Seabra, Tsutomu Momoi, Philippe Sindzingre, and Nic Shannon. Phase diagram of the classical heisenberg antiferromagnet on a triangular lattice in an applied magnetic field. *Phys. Rev. B*, 84:214418, Dec 2011.

[133] Ru Chen, Hyejin Ju, Hong-Chen Jiang, Oleg A. Starykh, and Leon Balents. Ground states of spin-$\frac{1}{2}$ triangular antiferromagnets in a magnetic field. *Phys. Rev. B*, 87:165123, Apr 2013.

[134] Oleg A. Starykh, Wen Jin, and Andrey V. Chubukov. Phases of a triangular-lattice antiferromagnet near saturation. *Phys. Rev. Lett.*, 113:087204, Aug 2014.

[135] Daisuke Yamamoto, Giacomo Marmorini, and Ippei Danshita. Quantum phase diagram of the triangular-lattice xxz model in a magnetic field. *Phys. Rev. Lett.*, 112:127203, Mar 2014.

[136] G. Marmorini, D. Yamamoto, and I. Danshita. On the umbrella-coplanar transition in the triangular XXZ model with arbitrary spin. *ArXiv e-prints*, October 2015.

[137] J. Schulenburg. Spinpack, 2016. [Online; accessed 27-February-2016].

[138] Sylvain Capponi, Oleg Derzhko, Andreas Honecker, Andreas M. Läuchli, and Johannes Richter. Numerical study of magnetization plateaus in the spin-$\frac{1}{2}$ kagome heisenberg antiferromagnet. *Phys. Rev. B*, 88:144416, Oct 2013.

[139] Francois Vernay. *Dégénérescence orbitale et ordre magnétique sur le réseau triangulaire : le cas des composés $LiNiO_2$ et $NaNiO_2$*. PhD thesis, École Polytechnique Fédérale de Lausane, 11 July 2005.

[140] Masahito Mochizuki, Youichi Yanase, and Masao Ogata. Ferromagnetic fluctuation and possible triplet superconductivity in $\mathrm{na}_x\mathrm{coo}_2 \cdot y\mathrm{h}_2\mathrm{O}$: Fluctuation-exchange study of the multiorbital hubbard model. *Phys. Rev. Lett.*, 94:147005, Apr 2005.

[141] N V Smith, S D Kevan, and F J DiSalvo. Band structures of the layer compounds 1t-tas 2 and 2h-tase 2 in the presence of commensurate charge-density waves. *Journal of Physics C: Solid State Physics*, 18(16):3175, 1985.

[142] Walter Kohn. Theory of the insulating state. *Phys. Rev.*, 133:A171–A181, Jan 1964.

[143] B. Sriram Shastry and Bill Sutherland. Twisted boundary conditions and effective mass in heisenberg-ising and hubbard rings. *Phys. Rev. Lett.*, 65:243–246, Jul 1990.

[144] Hirokazu Tsunetsugu and Masatoshi Imada. Dynamic exponent of t-j and t-J-W model. *Journal of the Physical Society of Japan*, 67(6):1864–1867, 1998.

[145] Tomonori Shirakawa and Eric Jeckelmann. Charge and spin drude weight of the one-dimensional extended hubbard model at quarter filling. *Phys. Rev. B*, 79:195121, May 2009.

[146] Toshihiro Sato, Kazumasa Hattori, and Hirokazu Tsunetsugu. Transport criticality at the mott transition in a triangular-lattice hubbard model. *Phys. Rev. B*, 86:235137, Dec 2012.

[147] A. I. Coldea, A. Carrington, R. Coldea, L. Malone, A. F. Bangura, M. D. Johannes, I. I. Mazin, E. A. Yelland, J. G. Analytis, J. A. A. J. Perenboom, C. Jaudet, D. Vignolles, T. Sorgel, and M. Jansen. Interplay between localized and itinerant d electrons in a frustrated metallic antiferromagnet, 2H-AgNiO2. *ArXiv e-prints*, August 2009.

[148] Douglas J. Scalapino, Steven R. White, and Shoucheng Zhang. Insulator, metal, or superconductor: The criteria. *Phys. Rev. B*, 47:7995–8007, Apr 1993.

[149] R. M. Fye, M. J. Martins, D. J. Scalapino, J. Wagner, and W. Hanke. Drude weight, optical conductivity, and flux properties of one-dimensional hubbard rings. *Phys. Rev. B*, 44:6909–6915, Oct 1991.

[150] C. A. Stafford, A. J. Millis, and B. S. Shastry. Finite-size effects on the optical conductivity of a half-filled hubbard ring. *Phys. Rev. B*, 43:13660–13663, Jun 1991.

[151] Elbio Dagotto. Correlated electrons in high-temperature superconductors. *Rev. Mod. Phys.*, 66:763–840, Jul 1994.

[152] Xiaotian Zhang. *Theoretical Study on Spontaneous Symmetry Breaking in Strongly Correlated Electrons*. PhD thesis, University of Tennessee, 5 2012.

Appendix A

Trianglar lattice

A.1 Triangular lattice

A.1.1 Three sublattice

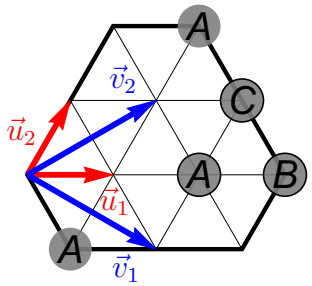

Fig. A.1 Triangular lattice, unit cell vectors $\vec{u}_1$ and $\vec{u}_2$; with the sublattice A, B and C, connected to equivalent sites by linear combination of $\vec{v}_1$ and $\vec{v}_2$ with integer coefficients. Two other A sites are labelled.

The phases we will meet in this dissertation, such as the pinball liquid, often have threefold orders, either on charge or orbitals. It can be seen as defining a new Bravais lattice with three sites per unit cell, represented in Figure A.1. In the triangular lattice, the unit call vectors are $\vec{u}_1 = (1, 0)$ and $\vec{u}_2 = \left(1/2, \sqrt{3}/2\right)$ and all equivalent site of the three sublattice are connected by linear combination of $\vec{v}_1 = 2\vec{u}_1 - \vec{u}_2$ and $\vec{v}_1 = \vec{u}_1 + \vec{u}_2$ with integer coefficients. This sublattice will be use many times in the following to describe threefold orders.

However, this description is not enough because one does not know a priori if other modulations occurs. This is why we need a more general concept, the Brillouin zone that we present below.

A.1.2 Brillouin zone

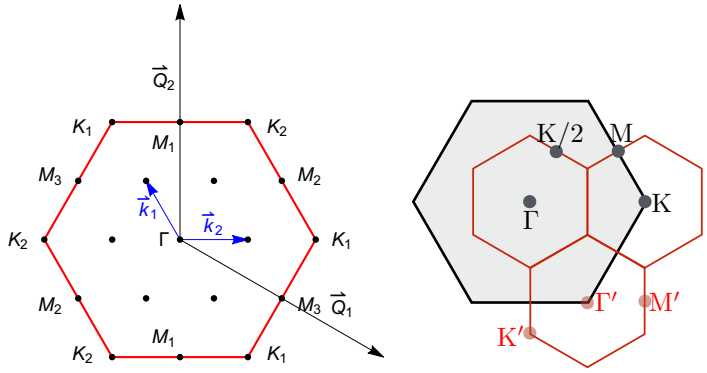

Fig. A.2 (left) First Brillouin zone of the triangular lattice for a cluster of 12 sites with the high symmetry points. The edges of the Brillouin zone are in red. The $\vec{k}$-points are in black. Two Brillouin zones are connected are the vectors $\vec{Q}_1$ and $\vec{Q}_2$ and two $\vec{k}$-points are connected by vectors $\vec{k}_1$ and $\vec{k}_2$. (right) Main symmetry points in the original (black) and reduced (red) Brillouin zone for three-sublattice ordering.

The Brillouin zone and in particular the first Brillouin zone is the ensemble of all the non-equivalent points in the reciprocal space. The shape of the Brillouin zone depends on the lattice geometry. The latter is defined by unit-cell vectors $\vec{u}_l$, $l = [1, D]$ and D the dimension of space. For a finite system with Periodic Boundary Conditions (PBC) $\vec{t}_l$, the vectors which connect two clusters, the number of non-equivalent points in the Brillouin zone is discrete and equal to the number of sites in the system. The discretization depends on the geometry of the finite cluster. Notice that although we will focus only on the triangular geometry, the method below is generic to define any Brillouin zone.

The triangular geometry is defined by the two unit-cell vectors $\vec{u}_1 = (1, 0)$ and $\vec{u}_2 = \left(1/2, \sqrt{3}/2\right)$. We will consider three types of clusters for the triangular lattice, defined by their periodic boundary condition vectors:

- The regular cluster $\vec{t}_1 = L\vec{u}_1$ and $\vec{t}_2 = L\vec{u}_2$.
- The tilted cluster $\vec{t}_1 = L\left(\vec{u}_1 + \vec{u}_1\right)$ and $\vec{t}_2 = L\left(-\vec{u}_1 + 2\vec{u}_1\right)$.
- The rectangular cluster $\vec{t}_1 = 2L\left(\vec{u}_1 + \vec{u}_1\right)$ and $\vec{t}_2 = L\left(-\vec{u}_1 + 2\vec{u}_1\right)$.

L is an integer. The last cluster does not respect the rotation symmetry because the norm of the vectors are different. Nevertheless they all respect the translation symmetry.

Let us first define the shape of the Brillouin zone, then we shall define the discretization. The generic formula to transform a set of three vectors, $\vec{a}_1$, $\vec{a}_2$ and $\vec{a}_3$, from real space to the reciprocal space is

$$\vec{b}_1 = 2\pi \frac{\vec{a}_2 \times \vec{a}_3}{\vec{a}_1.(\vec{a}_2 \times \vec{a}_3)},$$

$$\vec{b}_2 = 2\pi \frac{\vec{a}_3 \times \vec{a}_1}{\vec{a}_1.(\vec{a}_2 \times \vec{a}_3)},$$

$$\vec{b}_3 = 2\pi \frac{\vec{a}_1 \times \vec{a}_2}{\vec{a}_1.(\vec{a}_2 \times \vec{a}_3)},$$

where $\vec{a}_1.(\vec{a}_2 \times \vec{a}_3)$ is the volume occupied by the vectors. The first set of vectors to transform is the unit-cell vectors $\vec{u}_1$ and $\vec{u}_2$. In the third direction, the pattern does not repeat, formally, it is equivalent to a pattern that repeats at infinity. So their expression in three dimension is

$$\vec{e}_1 = (1, 0, 0),\ \vec{e}_2 = (1/2, \sqrt{3}/2, 0),\ \vec{e}_3 = \lim_{\alpha \to \infty} (0, 0, \alpha)$$

and the two vector that will define the shape of the Brillouin zone are

$$\vec{Q}_1 = 2\pi \left(1, -\frac{1}{\sqrt{3}}, 0\right),\ \vec{Q}_2 = 2\pi \left(0, \frac{2}{\sqrt{3}}, 0\right).$$

These two vectors connect two Brillouin zone. The edges of the latter are the lines normal to the vectors at the midpoints.

The discretization of the Brillouin zone comes from the vectors $\vec{t}_1$ and $\vec{t}_2$ that shall be transformed in vectors $\vec{k}_1$ and $\vec{k}_2$ of the reciprocal space:

- The regular cluster $\vec{k}_1 = 2\pi \left(\frac{1}{L}, -\frac{1}{\sqrt{3}L}\right)$ and $\vec{k}_2 = 2\pi \left(0, \frac{2}{\sqrt{3}L}\right)$.
- The tilted cluster $\vec{k}_1 = 2\pi \left(\frac{2}{3L}, 0\right)$ and $\vec{k}_2 = 2\pi \left(-\frac{1}{3L}, \frac{1}{\sqrt{3}L}\right)$.
- The rectangular cluster $\vec{k}_1 = 2\pi \left(\frac{1}{3L}, 0\right)$ and $\vec{k}_2 = 2\pi \left(-\frac{1}{3L}, \frac{1}{\sqrt{3}L}\right)$.

An example of Brillouin zone is given on the left in Figure A.2 for a cluster of 12 sites.

In this thesis, we sometimes consider the three sublattice we presented above. It is interesting to describe briefly its Brillouin zone. The new Bravais lattice contains three sites thus the area of the parallelogram form by them must be equal to three. The new Bravais vectors connect two equivalent sites so we can consider for example the new

unit-cell vectors $\vec{v}_1 = \vec{u}_1 + \vec{u}_2$ and $\vec{v}_1 = -2\vec{u}_1 + \vec{u}_2$. The corresponding Brillouin zone will be labelled reduced. Both the original and the reduced Brillouin zone are plot on the right panel in Figure A.2 with the main high symmetry points. One can notice in particular that the K-points, respectively the K/2 points, of the original Brillouin zone match the Γ-point, respectively the M-points, of the reduced Brillouin zone. So, each modulation that can be represented by the three sublattice above will be characterized in the Brillouin zone by a peak on K-point.

Appendix B

t_{2g} orbitals

The t_{2g}-orbitals are relevant to describe systems such as cobaltites which have rich phase diagrams. In particular, t_{2g}-orbitals are studied to understand the mechanism of exotic superconductivity in triangular-lattice cobalt oxides [140].

The 27 hopping integrals corresponding to the t_{2g}, using Slater and Koster [100], are

$$t^{xy,xy} = 3l^2m^2\,(dd\sigma) + \left(l^2 + m^2 - 4l^2m^2\right)(dd\pi) + \left(n^2 + l^2m^2\right)(dd\delta)$$

$$t^{xy,x^2-y^2} = \frac{3}{2}lm\left(l^2 - m^2\right)(dd\sigma) + 2lm\left(m^2 - l^2\right)(dd\pi) + \frac{1}{2}lm\left(l^2 - m^2\right)(dd\delta)$$

$$t^{xy,z^2} = \sqrt{3}lm\left(n^2 - \frac{1}{2}\left(l^2 + m^2\right)\right)(dd\sigma) - 2\sqrt{3}lmn^2\,(dd\pi) + \frac{\sqrt{3}}{2}lm\left(1 + n^2\right)(dd\delta)$$

$$t^{x^2-y^2,x^2-y^2} = \frac{3}{4}\left(l^2 - m^2\right)^2(dd\sigma) + \left(l^2 + m^2 - \left(l^2 - m^2\right)^2\right)(dd\pi) + \left(n^2 + \frac{1}{4}\left(l^2 - m^2\right)^2\right)(dd\delta)$$

$$t^{x^2-y^2,z^2} = \frac{\sqrt{3}}{2}\left(l^2 - m^2\right)\left(n^2 - \frac{1}{2}\left(l^2 + m^2\right)\right)(dd\sigma) + \sqrt{3}n^2\left(m^2 - l^2\right)(dd\pi) + \frac{\sqrt{3}}{4}\left(1 + n^2\right)\left(l^2 - m^2\right)(dd\delta)$$

$$t^{z^2,z^2} = \left(n^2 - \frac{1}{2}\left(l^2 + m^2\right)\right)^2(dd\sigma) + 3n^2\left(l^2 + m^2\right)(dd\pi) + \frac{3}{4}\left(l^2 + m^2\right)^2(dd\delta)$$

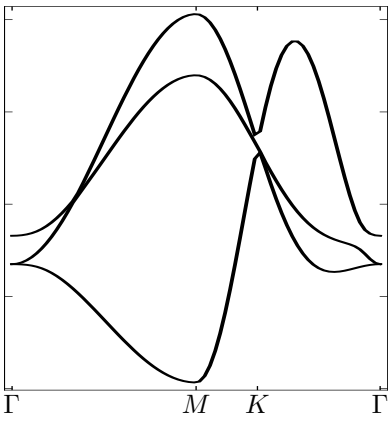

Fig. B.1 Band structure of t_{2g}-orbitals along the path $\Gamma MK\Gamma$ as defined in the Appendix A.1.2 with parameters fitting 1T-TaS_2 [18, 141].

The band structure along the path $\Gamma MK\Gamma$ corresponding to these hopping integrals is plot in Figure B.1 with parameters fitting 1T-TaS_2 [18, 141]. We choose this specific compound due to its peculiar large unit-cell charge-ordered phase of $\sqrt{13} \times \sqrt{13}$ Star of David modulation.

Appendix C

Phase characterization

In this appendix, tools used to characterized phases, order parameters, and to describe them in reciprocal space, with spectral function, will be introduced.

C.1 Order parameters

Let us introduce the order parameters we used to characterize the different phases of the system.

Due to the absence of constraints, the mean-field Hamiltonian does not necessarily commute with τ^2 and τ^z, which are, respectively, the total orbital pseudospin operator and its z component. To look for orbital orders, we use different order parameters. One can notice that the Fock terms of the Hubbard interaction can be recast in terms of the ladder pseudospin operators, allowing for the extraction of the average orbital components $\langle\tau^x\rangle$, $\langle\tau^y\rangle$, and $\langle\tau^z\rangle$

$$\tau_i^\tau = \frac{1}{2} d_{i\tau}^\dagger d_{i\tau},\ \tau_i^+ = \frac{1}{2} d_{i\uparrow}^\dagger d_{i\downarrow},\ \tau_i^- = \frac{1}{2} d_{i\downarrow}^\dagger d_{i\uparrow}. \tag{C.1}$$

We add an 1/2 factor to make the comparison with the spin more convenient. This is particularly useful in order to characterize, in addition to the charge symmetry breaking, solutions having an orbital order such as the 120° phase already observed in the Hubbard model at large U [84, 85]. Let us express these operators into the orbital components

$$\tau_i^x = \tau_i^+ + \tau_i^-,\ \tau_i^y = -i\left(\tau_i^+ - \tau_i^-\right),\ \tau_i^z = \tau_i^\uparrow - \tau_i^\downarrow.$$

and

$$\tau_i = \left(\tau_i^x, \tau_i^y, \tau_i^z\right).$$

This vector will be used to draw the vectorial representation of snapshots in Section 3.4. Notice that it adds informations about in-plane orders that are not present in regular snapshots, which are based on Hartree paramters only.

The total orbital operators are just the sum over all sites of the lattice

$$\tau^{\alpha} = \frac{1}{N_s} \sum_{i=1}^{N_s} \tau_i^{\alpha}. \tag{C.2}$$

This quantity gives information about global orbital polarization but does not capture local arrangement. If one, the following quantity is nonzero

$$\sum_{i=1}^{N_s} \left| \langle n_{i\uparrow} - n_{i\downarrow} \rangle \right|.$$

In case of commensurate order, orbital-orbital correlations gives access to the type of order in reciprocal space

$$T\left(\vec{k}\right) = (1/N_s) \langle \tau^z \left(-\vec{k}\right) \tau^z \left(\vec{k}\right) \rangle. \tag{C.3}$$

In addition, we used charge-charge correlations to identify charge orders

$$C\left(\vec{k}\right) = (1/N_s) \langle \rho \left(-\vec{k}\right) \rho \left(\vec{k}\right) \rangle,$$

with $\rho\left(\vec{k}\right)$ being the Fourier transform of the total on-site density operator $n_{i\uparrow} + n_{i\downarrow}$.

An equivalent approach can be to look at the charge and the orbital ordering in term of pseudo-probabilities as explained in Appendix F.

Insulating states are characterized by a gap at the Fermi energy equivalently the conducting state is possible only if excitations at Fermi energy are possible. Different methods can determine if a phase is metallic or insulating. One can cite for example the Drude weight which is derived from optical conductivity [142–146], however, our mean-field study did not give conclusive results as explained in Appendix G. Another possibility is to compute the electronic compressibility $\frac{1}{\kappa} \propto \frac{d\mu}{dn}$, with μ the chemical potential and n the number of particles. $\kappa = 0$ if the phase is incompressible which is characteristic to insulating states. A proper study of compressibility with a mean-field approach required a great attention to insure each points used for the finite numerical derivative, which itself contain drawbacks, converged to the global minima, otherwise fluctuations in the curve of $\mu(n)$ can appear and lead to spurious results. We will not use this approach but we compute the charge gap Δ_g which is the energy gap if we

add or remove an electron to the system so it corresponds to excitation around Fermi energy

$$\Delta_g = E\left(N_e - 1\right) + E\left(N_e + 1\right) - 2E\left(N_e\right). \tag{C.4}$$

It is expected that the reaction of the system to the variation of one electron to be small for a conducting state ($\Delta_g \simeq 0$) but very sensitive for an insulator (finite Δ_g).

Notice that we will use the same quantities for Exact diagonalization results in section 3.5 and in addition will compute the average double occupation $D = (1/N_s)\left\langle \sum_{i=1}^{N_s} n_{i\uparrow} n_{i\downarrow} \right\rangle$ which is expected to be zero in a Mott state where each site has only one electron but higher than the metallic state in charge ordered states because the charge disproportion will fill some sites more than others raising the double occupancy. It is especially true for some specific order such as the $\sqrt{12} \times \sqrt{12}$ droplet phase will meet later.

Numerically, order parameters does not reach exactly the expected value for a given phase and the stability, i.e. the fluctuation for two close sets of parameters $(t, t', \tilde{U}, V)$, depends on the type of parameter so the cut off used are different. Nevertheless, their behavior change sharply (see right panel of Figure 3.5 and Figure 3.6) so a cut off is usually easy to define and we took typically an approximation at 10^{-3} to the expected order parameters for a given phase.

C.2 Spectral function

To analyze the reconstruction of the band structures and Fermi surfaces, we computed the spectral function

$$A_\tau\left(\vec{k}, \omega\right) = \frac{-1}{\pi} \mathrm{Im} \langle \psi | d_{\vec{k}\tau} \frac{1}{\omega - H + i\eta} d^\dagger_{\vec{k}\tau} | \psi \rangle. \tag{C.5}$$

It is the imaginary part of the Green's function.

On each $\vec{k}$ point of the Brillouin zone, the Green's function has a pole when ω is an eigenvalue of the Hamiltonian.

Spectral function gives three important informations: (i) the band structure, (ii) the density of states through the sum over all the Brillouin zone and (iii) the Fermi surface with a cut at $\omega = E_F$, with E_F the Fermi energy, i.e. the energy of the last occupied state.

One can experimentally have access to the informations given by the spectral function, for example with Angle-Resolved Photoemission Spectroscopy (ARPES) which is a direct measurement of the spectral function. ARPES involves looking at

the reaction of the system (H) to the extraction of an electron ($d_{\vec{k}\tau}$) with a beam ($\omega \propto h\nu$). The sample is beamed with an energy $\omega \propto h\nu$. The beam excites the electrons. The excited electron is analyzed, i.e. one measure the angle, which gives information about the momentum, and the energy of the extracted electron. The momentum perpendicular to the surface is not conserved. However, the momentum parallel to the surface is conserved. In two-dimensional material, only the parallel momentum is of interest which makes ARPES an ideal tool in this case.

One can also have access to the Fermi surface via the method of Fermi-surface reconstruction by quantum oscillations. The latter are obtained through the torque $\vec{\tau} = \vec{m} \times \vec{B}$, with $\vec{m}$ the magnetization and $\vec{B}$ the magnetic field, by doing the Fourier transform. The peaks, associated to a frequency, is related to an area in the Fermi surface.

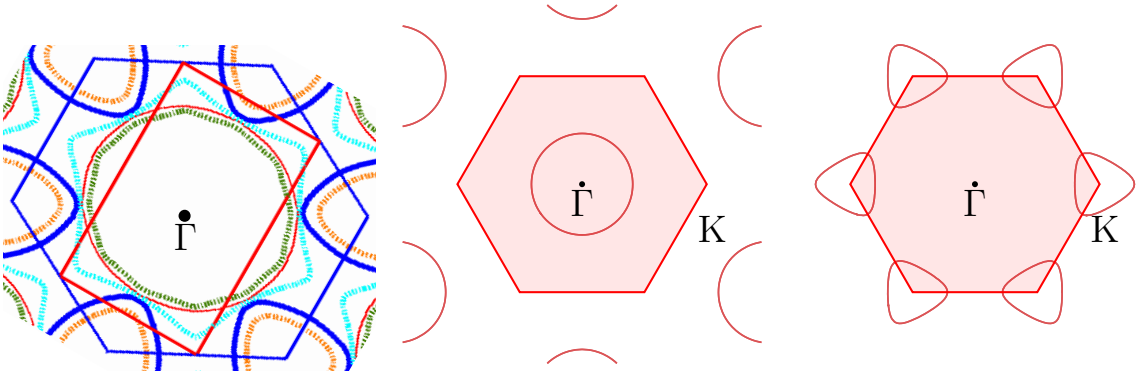

Fig. C.1 (left) Slice of the Fermi surface when the magnetic field is pointing along the c axis. The predicted orbits are shown (solid and dotted lines) inside the and non-magnetic (hexagonal) Brillouin zone. Figure reproduced from [147] and rotated of 30°. Fermi surfaces for the noninteracting triangular lattice a filling of 0.2 for (center) electron and (right) hole.

The Fermi surface of $2H$-$AgNiO_2$ has been measured using this method with the presence of a magnetic field [147], which has an interesting side effect for our purpose. The metallic charge-ordered phase in this compound has a magnetic order which makes the picture more complicated. Above 38T, the magnetic order is completely removed because all spins are parallel. In this configuration, it is energetically favorable for electrons on the same site to be on different orbitals rather than pairing. It correspond to the approximation $U_{mm} \gg U_{m,m'}$ we made above in Section 2.2. In this sense, this can be seen as if the system becomes spinless. We reproduced the Fermi surface measured by Coldea on the left panel in Figure C.1.

At last, we want to add final comment about Fermi surfaces. Let us consider a simple model, e.g. the tight-binding for electrons in triangular lattice

$$\epsilon_{\mathrm{e}}\left(\vec{k}\right) = -2\left(2\cos\left(\frac{k_x}{2}\right)\cos\left(\frac{\sqrt{3}k_y}{2}\right) + \cos\left(k_x\right)\right).$$

For holes, the relation will be the same relation with an opposite sign

$$\epsilon_{\mathrm{h}}\left(\vec{k}\right) = -\epsilon_{\mathrm{e}}\left(\vec{k}\right).$$

The two corresponding Fermi surfaces for a low filling of 0.2 are plotted on the center and the right panels in Figure C.1. One can see that in the case of electrons (left), the Γ point is circled and for holes (right), the K points are circled.

Appendix D

Symmetrizations

In this appendix, we shall introduce the symmetrization. We use this method in the unrestricted Hartree-Fock approach. It adds constrain in the evolution of the convergence in the algorithm which can help to achieve the latter. The drawback is that it makes assumptions about the solution. The unrestricted Hartree-Fock algorithm must always be tested without symmetrization in order to assure the mean-field ground state is compatible with the chosen cluster. Symmetrization can never be used for incommensurate phase.

Symmetrization is the fact to choose a cluster, so a set of two vectors for two-dimensional systems, and constrain parameters to repeat in real space with a modulation which is at most this cluster. It involves the $\vec{k}$-points in the Brillouin zone for these parameters are limited to the $\vec{k}$-points of the chosen cluster. Parameters connected by a linear combination of vectors of the chosen cluster with integer coefficients are average. Then, this average value is affect to all assumed equivalent sites.

This action is repeated at each iteration of the unrestricted Hartree-Fock algorithm. We performed the symmetrization typically on the local electronic density, Hartree mean-field parameters, and also on the Fock mean-field parameters. Basically, we used all possible clusters defined in Appendix A.1.2 up to 48 sites. One can cite for example the symmetrization on a three-sublattice with the vectors $\vec{v}_1 = \vec{u}_1 + \vec{u}_2$ and $\vec{v}_1 = -2\vec{u}_1 + \vec{u}_2$. The symmetrization giving the best results is on 12 sites. It is working everywhere except for the PCO_I phase and, of course, for the incommensurate phases.

Appendix E

Basis of hermitian matrices in the Pauli matrices representation

In this appendix, we shall briefly review how to express 2×2 and 4×4 hermitian matrices as a function of Kronecker Products of the Pauli matrices.

2×2 Matrix

Any 2×2 hermitian matrix can be a representation of an operator acting on a 1/2-spin. These matrices can always be rewritten in the Pauli matrices basis $\{I_2, \sigma^x, \sigma^y, \sigma^z\}$, with I_2 the identity matrix and the Pauli matrices

$$\sigma^x = \begin{pmatrix} 0 & 1 \\ 1 & 0 \end{pmatrix}, \ \sigma^y = \begin{pmatrix} 0 & -i \\ i & 0 \end{pmatrix}, \ \sigma^z = \begin{pmatrix} 1 & 0 \\ 0 & -1 \end{pmatrix}.$$

Proof. A is a general 2×2 hermitian matrix.

$$A = \begin{pmatrix} a & b \\ b^* & d \end{pmatrix} = \alpha I_2 + \beta\sigma^x + \gamma\sigma^y + \delta\sigma^z, \tag{E.1}$$

with $a, b, c, d, \alpha, \beta, \gamma, \delta \in \mathbb{C}$. If Eq. E.1 has a solution, so any 2×2 hermitian matrix can be written as a linear combination of Pauli matrices. This Eq. E.1 has a solution

$$\begin{cases} \alpha &= \frac{a}{2} + \frac{d}{2} \\ \beta &= \mathrm{Re}\{b\} \\ \gamma &= \mathrm{Im}\{b\} \\ \delta &= \frac{a}{2} - \frac{d}{2}. \end{cases}$$

□

Let us write the linear combination

$$A = \frac{1}{2}(a+d)\, I_2 + \mathrm{Re}\{b\}\sigma^x + \mathrm{Im}\{b\}\sigma^y + \frac{1}{2}(a-d)\,\sigma^z.$$

Notice that all coefficients are now real.

4×4 Matrix

At this point, one can ask: *Is a 4×4 hermitian matrix can be expressed in term in term of Kronecker Products of Pauli matrices?* In other words, can we find a linear combination of complex coefficients of the ensemble of the 16 Kronecker Products of Pauli matrices to express a 4×4 hermitian matrix? The answer is yes, and we shall prove it now.

Proof. M is a 4×4 hermitian matrix

$$M = \begin{pmatrix} m_{11} & im_{12i} + m_{12r} & im_{13i} + m_{13r} & im_{14i} + m_{14r} \\ m_{12r} - im_{12i} & m_{22} & im_{23i} + m_{23r} & im_{24i} + m_{24r} \\ m_{13r} - im_{13i} & m_{23r} - im_{23i} & m_{33} & im_{34i} + m_{34r} \\ m_{14r} - im_{14i} & m_{24r} - im_{24i} & m_{34r} - im_{34i} & m_{44} \end{pmatrix}.$$

The coefficient m_{ij} are real numbers. Our basis is

$$B = \{b_i, i \in [1, 16]\}$$

with

$$b_1 = I_2 \otimes I_2,\ b_2 = I_2 \otimes \sigma^x,\ b_3 = I_2 \otimes \sigma^y,\ b_4 = I_2 \otimes \sigma^z,\ b_5 = \sigma^x \otimes I_2,\ b_6 = \sigma^x \otimes \sigma^x,$$

$$b_7 = \sigma^x \otimes \sigma^y,\ b_8 = \sigma^x \otimes \sigma^z,\ b_9 = \sigma^y \otimes I_2,\ b_{10} = \sigma^y \otimes \sigma^x,\ b_{11} = \sigma^y \otimes \sigma^y,\ b_{12} = \sigma^y \otimes \sigma^z,$$

$$b_{13} = \sigma^z \otimes I_2,\ b_{14} = \sigma^z \otimes \sigma^x,\ b_{15} = \sigma^z \otimes \sigma^y,\ b_{16} = \sigma^z \otimes \sigma^z.$$

In the following, the Kronecker product will be implicit, $\sigma_i \otimes \sigma_j = \sigma_i\sigma_j$ and by convention, the Kronecker product with Identity will be implicit, e.g. $\sigma_i \otimes I_2 = \sigma_i$ ans $I_2 \otimes I_2 = 1$.

$$G = \sum_{i=1}^{16} \alpha_i b_i$$

is the most general linear combination with complex coefficient $\alpha_i \in \mathbb{C}$ for this basis. If

$$M = G \tag{E.2}$$

has a solution, any 4×4 hermitian matrix can be written as a linear combination of Kronecker Products of Pauli matrices. Eq. E.2 has a solution, which is:

$$\begin{aligned}
M &= \frac{1}{4}\left(m_{11}+m_{22}+m_{33}+m_{44}\right)b_1 + \frac{1}{2}\left(im_{13i}+m_{13r}+im_{24i}+m_{24r}\right)b_2 \\
&+ \frac{1}{2}\left(-im_{13i}+m_{13r}-im_{24i}+m_{24r}\right)b_3 + \frac{1}{4}\left(m_{11}+m_{22}-m_{33}-m_{44}\right)b_4 \\
&+ \frac{1}{2}\left(im_{12i}+m_{12r}+im_{34i}+m_{34r}\right)b_5 + (m_{14r}+im_{14i})b_6 \\
&+ (m_{23r}-im_{23i})b_7 + \frac{1}{2}\left(im_{12i}+m_{12r}-im_{34i}-m_{34r}\right)b_8 \\
&+ \frac{1}{2}\left(-im_{12i}+m_{12r}-im_{34i}+m_{34r}\right)b_9 + (m_{23r}+im_{23i})b_{10} \\
&+ (m_{14r}-im_{14i})b_{11} + \frac{1}{2}\left(-im_{12i}+m_{12r}+im_{34i}-m_{34r}\right)b_{12} \\
&+ \frac{1}{4}\left(m_{11}-m_{22}+m_{33}-m_{44}\right)b_{13} + \frac{1}{2}\left(im_{13i}+m_{13r}-im_{24i}-m_{24r}\right)b_{14} \\
&+ \frac{1}{2}\left(-im_{13i}+m_{13r}+im_{24i}-m_{24r}\right)b_{15} \\
&+ \frac{1}{4}\left(m_{11}-m_{22}-m_{33}+m_{44}\right)b_{16}.
\end{aligned} \tag{E.3}$$

□

Appendix F

Pseudo-probabilities

The density-density correlation function is a good way to draw snapshots of the phases we found for the multiorbital extended Hubbard model because it reads pseudo-probabilities. It is not real probabilities in the sense that they are not defined positive and can be complex. The following tool is mostly used in quantum optics and know as the degree of coherence. In our case, the best way to look at the snapshots of the unrestricted Hartree-Fock approach is to look at the normalized second order correlation function

$$g^2\left(x,x';x',x\right)=\frac{G^2\left(x,x';x',x\right)}{G^1\left(x,x\right)G^1\left(x',x'\right)},$$

with

$$G^1\left(x,x'\right)=\langle c^\dagger(x)c(x')\rangle,$$

$$G^2\left(x,x';x',x\right)=\langle c^\dagger(x)c^\dagger(x')c(x')c(x)\rangle$$

and x and x' are variables, usually the coordinate with or without the time. The first order correlation function $G^1\left(x,x\right)$ reads the probability of having a particle in x $P\left(x\right)$. The second order correlation function $G^2\left(x,x';x',x\right)$ reads the probability of having a particle in x and x' $P\left(x\cap x'\right)=P\left(x|x'\right)P\left(x'\right)=P\left(x'|x\right)P\left(x\right)$ in term of conditional probabilities and using Bayes' theorem. Using the Wick theorem for fermions,

$$\langle c_i^\dagger c_j c_k^\dagger c_l\rangle=\langle c_i^\dagger c_j\rangle\langle c_k^\dagger c_l\rangle+\langle c_i^\dagger c_l\rangle\langle c_j c_k^\dagger\rangle,$$

one found the general result

$$g^2\left(i,j;j,i\right)=1-\frac{\langle c_i^\dagger c_j\rangle\langle c_j^\dagger c_i\rangle}{\langle n_i\rangle\langle n_j\rangle}.$$

The latter is real for the Multiorbital Extended Hubbard Model and $g^2(i,i;i,i) = 0$ (Pauli principle). Formally, $g^2\left(i,j;j,i\right) = \frac{P(i|j)}{P(i)}$, with $P(i)$ the probability to have an electron on the state i and $P(i|j)$ the probability to have an electron on the state i given that an electron is on the state j. From this statement, one can immediately notice that $g^2 = 1$ means the state i and j are independent. The previous expression of g^2 is convenient for the Hartree-fock approximation because it depends on the mean-field parameters. However, an expression as a function of diagonal operators is more suitable for Lanzos approximation

$$g^2\left(i,j;j,i\right) = \frac{\langle n_i n_j\rangle - \langle n_i\rangle\delta_{i,j}}{\langle n_i\rangle\langle n_j\rangle},$$

with $\delta_{i,j}$ the Kronecker delta. To simplify the picture of a phase, we will focus only on the correlation between two sites regardless the orbitals. Here a formal derivation, $P\left(i\right) = \langle n_i\rangle = \langle n_i^{\uparrow}\rangle + \langle n_i^{\downarrow}\rangle$. For $i \neq j$, $P\left(i \cap j\right) = \langle n_i n_j\rangle$. Using Wick theorem,

$$\frac{P(i\cap j)}{P(i)P(j)} = 1 - \frac{\sum_{\tau,\tau'=\uparrow,\downarrow}\left|\langle c_i^{\tau\dagger}c_j^{\tau'}\rangle\right|^2}{\sum_{\tau,\tau'=\uparrow,\downarrow}\langle n_i^{\tau}\rangle\langle n_j^{\tau'}\rangle} \equiv g^2\left(i,j;j,i\right). \tag{F.1}$$

Appendix G

Drude weight for Hubbard model in mean-field approximation

This section describe an attempts to determine the metallic character of mean-field solutions via a calculation of the Drude weight. Although the calculations were not conclusive because we failed to compute reasonable value of Drude weight they contain some useful informations, for example for the noninteracting case, that we choose to report here.

G.1 One-dimensional chain

We will study Drude weight an one-dimension chain.

G.1.1 Kinetic energy of a finite system

The kinetic operator of an one-dimensional noninteracting chain is

$$\hat{K} = -t \sum_{i=1}^{N_s} \left(\hat{c}_i^\dagger \hat{c}_{i+1} + \hat{c}_{i+1}^\dagger \hat{c}_i \right),$$

where N_s is the number of sites in the system, t the hopping integral which is the amplitude of probability for an electron to go from on site to another and $\hat{c}_i$ ($\hat{c}_i^\dagger$) the annihilation (creation) operator of an electron on the site i. The Fourier transform of the creation and annihilation operators is introduced as follow:

$$\hat{c}_i^\dagger = \frac{1}{\sqrt{N_s}} \sum_{\vec{k} \in \mathrm{BZ}} e^{-i\vec{k}.\vec{r_i}} \hat{c}_{\vec{k}}^\dagger$$

and

$$\hat{c}_i = \frac{1}{\sqrt{N_s}} \sum_{\vec{k}\in \mathrm{BZ}} e^{i\vec{k}.\vec{r_i}} \hat{c}_{\vec{k}},$$

where $\vec{r_i}$ is the position of the site i and BZ is the Brillouin Zone (See Section A.1.2). This transformation directly diagonalize this operator

$$\hat{K} = -2t \sum_{\vec{k}\in \mathrm{BZ}} \cos\left(\vec{k}.\vec{u}\right) \hat{c}^{\dagger}_{\vec{k}} \hat{c}_{\vec{k}}.$$

with $\vec{u}$ the displacement between two sites nearest neighbors (n.n.) in one direction, $\vec{r_n} = n\vec{u}$.

G.1.2 Peierls substitution

To distinguish a metal from a insulator at zero-temperature, we look at the response of the system to an electromagnetic field. We apply a vector potential $\vec{A}$ to the tight binding model which changes the hopping integral with the Peierls substitution [142, 144, 145]

$$t_{\vec{u_i}} \to t_{\vec{u_i}} e^{\vec{A}.\vec{u_i}}.$$

$\vec{u_i}$ is the unit cell vector in the i direction. We define $\vec{A} = \sum_i \frac{\phi_i}{L_i} \vec{e_i}$ with L_i the length of the lattice in the i direction ($L_i = N_i u_i$) and $\vec{e_i}$ the canonical basis vectors in space. With this substitution, the kinetic operator becomes

$$\hat{K}\left(\vec{A}\right) = -2 \sum_{\vec{k}\in \mathrm{BZ}} \hat{c}^{\dagger}_{\vec{k}} \hat{c}_{\vec{k}} \sum_{j=0}^{N_{n.n.}/2} t_{\vec{v_j}} \cos\left(\left(\vec{k} + \vec{A}\right).\vec{v_j}\right), \tag{G.1}$$

with $N_{n.n.}$ the number of nearest neighbors and $\vec{v_j}$ the vector connecting two nearest neighbors in the j direction. It leads to the Drude weight in a $\vec{v_i}$ direction [144]

$$D_i = \lim_{V\to\infty} \frac{1}{V} \frac{\partial^2 E\left(\vec{A}\right)}{\partial A_i^2}\bigg|_{\vec{A}=\vec{0}}, \tag{G.2}$$

with V the volume of the system, $E\left(\vec{A}\right)$ the ground state and $A_i = \vec{A}.\vec{v_i}$.

G.1.3 Spectrum of the noninteracting chain in the presence of a vector potential

We apply the vector potential to an one-dimensional chain. In this case, the latter is $\vec{A} \to A = \frac{\phi}{L}$, with ϕ the flux and $L = uN_s$ the size of the chain.

$$\hat{K}(\phi) = -2t \sum_{k \in \mathrm{BZ}} \cos\left(ku + \frac{\phi}{N_s}\right) \hat{c}^{\dagger}_{\vec{k}} \hat{c}_{\vec{k}}.$$

To find the ground state, we can list the energies given by all possible set of $\vec{k}$ used in the sum

$$E(\phi) = -2t \sum_{\vec{k} \in \mathrm{BZ}} \cos\left(\vec{k}.\vec{u} + \frac{\phi}{N}\right)$$

then take the lowest energy. Here, we are interested by the ground state close to $\vec{A} = \vec{0}$. Using the expression of $\vec{k}$, we can show the energy does not depend on the spacing u between sites:

$$E(\phi) = -2t \sum_{\{n\}} \cos\left((2\pi n + \phi)\frac{1}{N}\right),$$

with $\{n\}$ defined such as to span all k-points.

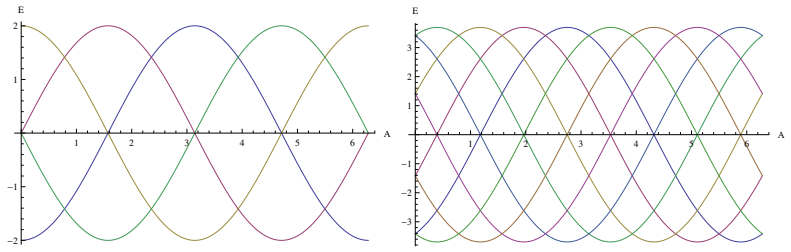

Fig. G.1 Spectrum of a quarter-filled one-dimensional chain with 4 (left) and 8 (right) sites.

Even though our main focus is the half-filled system, we want to show here that there are parity effect that can be clearly seen in the quarter-filled case. Spectrum of a quarter-filled chain of 4 sites (left) and 8 sites (right) as a function the vector potential $\vec{A}$ are report in Figure G.1. Due to a parity effect[1], one can see that the behavior of the energy of ground state close to $\vec{A} = \vec{0}$ is completely different and most notably, the second derivative of the energy is different in both cases. So, one can expect different behaviors of the limit in the convergence of the Drude weight due to the odd or even number of electrons, however the limit should be the same.

[1] One electron in the first case and two in the second case.

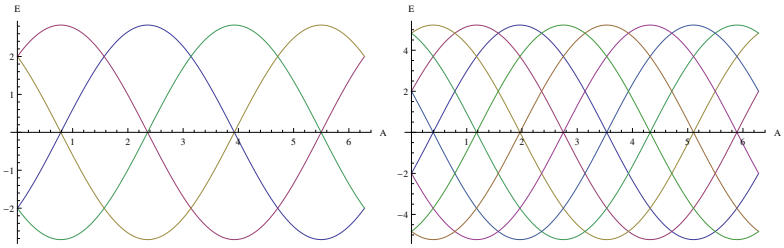

Fig. G.2 Spectrum of a half-filled one-dimensional chain with 4 (left) and 8 (right) sites.

Spectrum of a half-filled chain of 4 sites (left) and 8 sites (right) as a function the vector potential $\vec{A}$ are report in Figure G.2. One can see that crossing levels goes to $\vec{A} = \vec{0}$ when the size of the system increases (also shown in Ref. [148]). It means that we have to be careful to crossing levels in order to have a defined derivative of energy when we compute the thermodynamic limit in Drude weight.

G.1.4 Drude weight of an one-dimension chain

Noninteracting system

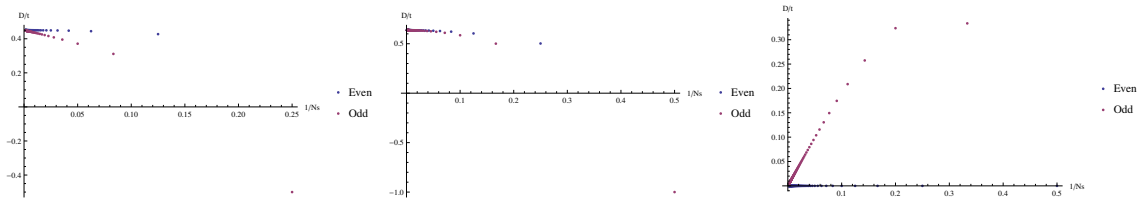

Fig. G.3 Convergence of Drude weight for a quarter-filled (left), half-filled (middle) and filled (right) chain as a function of the size.

Figure G.3 reports the convergence to the thermodynamic limit of the Drude weight for three fillings: quarter, half and completely filled band. As expected from the spectrum seen above, the convergence of the Drude weight has a parity effect and this effect is stronger for a quarter-filled system than the half-filled system, moreover, for small system, one can find negative Drude weight corresponding to permanent currents, nevertheless, the same limit is reached at the thermodynamic limit.

For a completely filled band, one expects an insulator. However the right panel of Figure G.3 represents the Drude weight as previously for a filled band and as for a partially filled band, a parity effect appears. The second derivative of the energy is always zero for even number of sites but has a finite value for a finite size. The system behaves as expected at the thermodynamic limit.

Short-range interaction

As defined in Section 2.2, we want to study the effects of short-range interactions V moreover, in a mean-field approximation, so we will compare here with exact diagonalization.

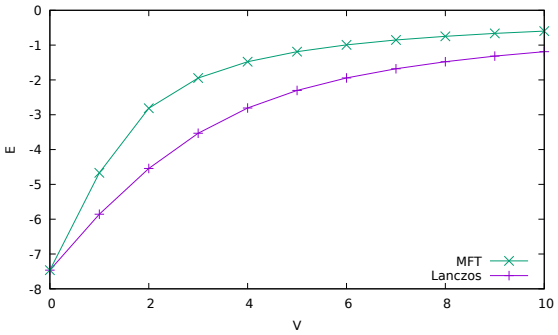

Fig. G.4 Value of the energy of the ground state for a half-filled cluster of 12 sites without vector potential as a function of the short-range interaction V computed with Lanczos and mean-field theory algorithm.

First, we plot the energy of the ground state for both method in Figure G.4 for a 12-site cluster at half-filling. and one can notice a notable energy difference. Let us see if this difference can change the behavior of the system.

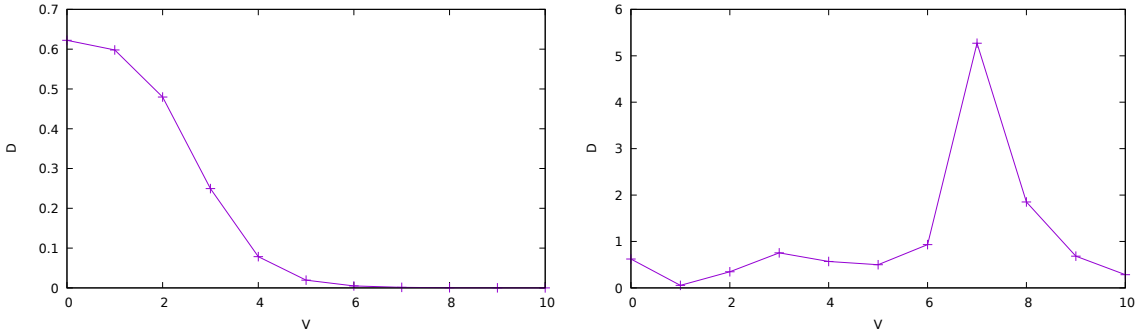

Fig. G.5 Drude weight computed using (left) Lanczos algorithm and (right) mean-field theory as a function of the short-range interaction V for a half-filled chain of 12 sites.

The Drude weight is expected to drop for sufficient interaction because it induces a phase transition to a charge-ordered state. Figure G.5 reports the evolution of Drude weight for 12-site cluster as a function of V for both an exact treatment (left panel) and a mean-field approach (right panel). One can clearly see that the mean-field approach is far from capturing the qualitative behavior of Drude weight.

G.2 Temperature effects on a noninteracting chain with mean-field theory

Because we sometimes use a small temperature in the mean-field approach, we conclude on the one-dimensional chain by looking at its effect on the Drude weight. Even for small temperature, effects on mean-field solution are notable because temperature mixes all quasiparticle associated to the eigenvectors $d_\kappa^\dagger|0\rangle$ (see Section 3.4.1)

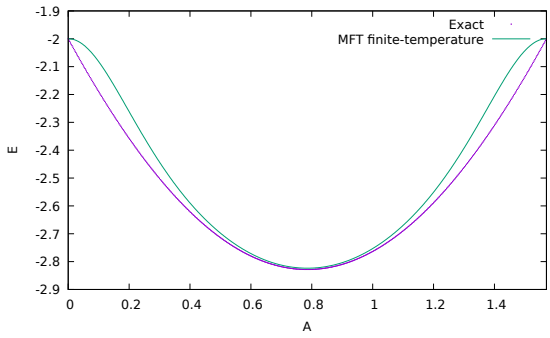

Fig. G.6 Energy of the ground state of a noninteracting half-filled chain of 4 sites as a function of the vector potential found exactly and with Mean Field Theory algorithm at finite-temperature ($\beta = 5$).

Figure G.6 summarizes the result in the non-interacting limit at zero and finite temperature. We took an inverse temperature $\beta = 5$ much larger than the typical temperature we use in unrestricted Hartree-Fock ($\beta = 100$) in order to amply the effect. The effect of the temperature is drastic on the Drude weight as it becomes negative which correspond to a permanent current. The conclusions for the system of 4 sites are the same for the system of 8 sites. To conclude this section, computing the Drude weight in the mean-field approach with temperature should be done carefully.

G.3 Drude weight in noninteracting half-filled triangular lattice

We conclude this appendix with the Drude weight of the noninteracting half-filled triangular lattice.

The kinetic operator for the triangular lattice in the presence of a vector potential using (Eq. G.1) is

$$\hat{K}\left(\vec{A}\right) = -2t \sum_{\{\vec{k}\}} \hat{c}^{\dagger}_{\vec{k}} \hat{c}_{\vec{k}} \cos\left(\left(\vec{k}+\vec{A}\right).\vec{u_1}\right)$$
$$-2t_c \sum_{\{\vec{k}\}} \hat{c}^{\dagger}_{\vec{k}} \hat{c}_{\vec{k}} \cos\left(\left(\vec{k}+\vec{A}\right).(\vec{u_2}+\vec{u_3})\right),$$

with $\vec{u}_1 = (1,0)$, $\vec{u}_2 = \left(1/2, \sqrt{3}/2\right)$, and $\vec{u}_3 = \vec{u}_2 - \vec{u}_1$.

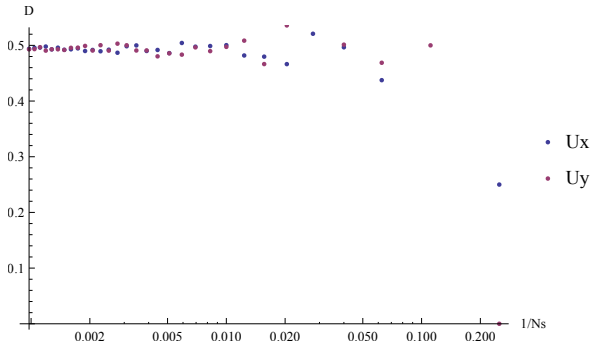

Fig. G.7 Drude weight in the $\vec{u_x}$ and $\vec{u_y}$ directions for the noninteracting half-filled triangular lattice.

The convergence of the Drude weight in the $\vec{u}_x$ and $\vec{u}_y$ directions is plotted in Figure G.7. The convergence is rather smooth and there is no notable different between x and y direction.

Notice that no parity effect is present, however, we can see oscillations in the convergence of the Drude weight.

We conclude this appendix by mentioning that negative Drude weight, computed this the second derivative as we did or using the current operator, for the half-filled Hubbard model is a confirmed effect in one dimension [149, 150] by different methods which has no physical meaning [151] as one can show that it is a size effect and that it goes to zero at the thermodynamic limit. This negative Drude weight has also been reported for d-orbitals with a mean-field approach [152].